Atmospheric Recycling Prevents Premature Collapse of Protoplanetary Atmospheres of Close-in Super-Earths and Mini-Neptunes

Dissertation

der Mathematisch-Naturwissenschaftlichen Fakultät

der Eberhard Karls Universität Tübingen

zur Erlangung des Grades eines

Doktors der Naturwissenschaften

(Dr. rer. nat.)

vorgelegt von

Tobias Walter Moldenhauer

aus Balingen

Tübingen

2022

Gedruckt mit Genehmigung der Mathematisch-Naturwissenschaftlichen Fakultät der Eberhard Karls Universität Tübingen.

Tag der mündlichen Qualifikation:	30.5.2022
Dekan:	Prof. Dr. Thilo Stehle
1. Berichterstatter:	PD Dr. Rolf Kuiper
2. Berichterstatter:	Prof. Dr. Klaus Werner

Abstract

In recent years, space missions such as *Kepler* and the Transiting Exoplanet Survey Satellite (*TESS*) have discovered numerous close-in planets that are more massive than Earth but less massive than gas giants: super-Earths and mini-Neptunes. Their often significant atmospheres consisting of mainly hydrogen and helium indicate that these planets formed early in gas-rich disks while avoiding the runaway gas accretion that would otherwise have turned them into hot Jupiters. This challenges current planet formation models. As a possible mechanism to prevent Kelvin-Helmholtz contraction of the atmosphere, hydrodynamical atmosphere-disk recycling has been suggested. However, because atmospheric recycling can only be captured by three-dimensional simulations which are inherently more computationally expensive, this effect has often been ignored in previous studies.

This thesis investigates the efficacy of the recycling hypothesis in preventing the collapse of the atmosphere. Additionally, the effects of the core mass, optical depth, orbital separation, and the effect of circumstellar gas on sub-Keplerian orbits (headwind) on the recycling process are investigated.

Using three-dimensional radiation-hydrodynamics simulations the formation of the protoplanetary atmosphere is modeled. As part of this thesis, a new particle integrator was implemented to utilize tracer particles in addition to tracer fluids to measure the recycling timescale. This new method allows studying the recycling process in an unprecedented amount of detail.

For the explored parameter space, all simulations except for those with the largest orbital separation of $a_p = 1\,\mathrm{au}$, eventually converge to a thermodynamic equilibrium where gas accretion stops. For the first time, it is shown that atmospheric recycling is capable of fully compensating radiative cooling. In all simulations the atmosphere-to-core mass ratio stays well below 10 %, preventing the atmosphere from becoming self-gravitating and entering runaway gas accretion.

For close-in planets, recycling naturally halts the cooling of planetary proto-atmospheres, preventing them from contracting toward the runaway regime and collapsing into gas giants. Thereby explaining the high frequency of observed super-Earths and mini-Neptunes that avoided atmospheric collapse.

Zusammenfassung

In den letzten Jahren haben Weltraummissionen wie *Kepler* und der Transiting Exoplanet Survey Satellite (*TESS*) viele neue Exoplaneten entdeckt. Ein großer Teil dieser Planeten umkreisen ihren Stern mit einem relativ kleinen Abstand, sind massereicher als die Erde aber besitzen trotzdem noch deutlich weniger Masse als Gasriesen: Die sogenannten Supererden und Mini-Neptune. Da ihre Atmosphären zum großen Teil aus Wasserstoff und Helium bestehen, kann man davon ausgehen, dass sie relativ früh während der noch gasreichen Phase der protoplanetaren Scheibe entstanden sind. Dadurch hatten diese Planeten grundsätzlich genügend Zeit um ausreichend Gas für die Entstehung eines Gasriesens zu akkretieren. Aktuelle Planetenentstehungsmodelle stoßen daher bei diesen Beobachtungen an ihre Grenzen. Als ein möglicher Mechanismus der den Kollaps der Atmosphäre und damit den Übergang zu einem Gasriesen verhindert, wurde atmosphärisches Recycling vorgeschlagen. Da dieser Mechanismus nur mit aufwendigen dreidimensionalen Simulationen modelliert werden kann, wurde er in der Vergangenheit oft ignoriert.

In dieser Arbeit werden dreidimensionale hydrodynamische Simulationen mit Strahlungstransport verwendet um die Effektivität des Recyclingmechanismus zu untersuchen. Dabei wird der Einfluss der Planetenkernmasse, der optischen Tiefe, des Abstands zwischen Planeten und Stern sowie der Einfluss von Gas, das auf Grund des Druckgefälles in der protoplanetaren Scheibe langsamer als der Planet um den Stern kreist, untersucht. Die Recyclingzeitskala der Atmosphäre wird mithilfe von Tracerpartikeln und Tracerfluiden in einem beispiellosen Detailgrad bestimmt. Dazu wurde im Rahmen dieser Arbeit ein neuer Tracerpartikel-Integrator implementiert.

Bis auf die Simulationen mit der größten Umlaufbahn von $a_p = 1\,\mathrm{au}$ erreichen alle durchgeführten Simulationen einen thermodynamischen Gleichgewichtszustand in dem die Atmosphäre nicht weiter kühlt. Diese Arbeit demonstriert damit zum ersten Mal, dass atmosphärisches Recycling in der Lage ist, den Energieverlust durch radiatives Kühlen vollständig auszugleichen. Das Verhältnis der Atmossphärenmasse zur Kernmasse bleibt bei allen Simulationen im Gleichgewichtszustand unter 10 % wodurch der Übergang zu einem Gasriesen verhindert wird.

Die Ergebnisse zeigen, dass für Planeten, die ihren Stern mit einem relativ kleinen Abstand umkreisen, der Übergang zu einem Gasriesen durch atmosphärisches Recycling verhindert wird. Atmosphärisches Recycling ist damit eine sehr gute Erklärung für das häufige Auftreten von Supererden und Mini-Neptunen, die einen geringen Abstand zu ihrem Stern aufweisen.

Contents

Chapter 1

Introduction

1.1 History of astronomy and exoplanets

Humanity has always had a special interest in the sky, its observable objects, and its various wondrous phenomena. Both its beauty and mysteriousness have captivated humans for millennia and have sparked many myths, religions, and scientific theories about the origin and evolution of these observations. Unsurprisingly, astronomy is the oldest of the natural sciences and was already a highly developed science before physics and chemistry were studied systematically (Pannekoek, 1961). At least as early as antiquity, people were able to differentiate between other stars and the planets within the solar system. However, it took humanity until the beginning of the 20th century to understand that, unlike planets, stars undergo nuclear fusion to sustain their high radiative energy output (Eddington, 1920; Bethe and Critchfield, 1938). People observed that planets moved in the night sky relative to the fixed stars. Hence their name in Ancient Greek, πλανήτες αστέρες (planētes asteres, "wandering stars"). Additionally, they noticed that these wandering stars do not move randomly but follow patterns which allowed them to develop theories to predict their movement. Early models suggested that the planets and the sun moved around the earth on circular orbits. However, observed orbits regularly deviated from the trajectories predicted by these models. Therefore, these first models were extended to more complicated

geocentric models. The Ptolemaic model developed by Claudius Ptolemaeus in the 2nd century AD, for example, used a system of two spheres for each planet. Here, the first sphere, the deferent, was centered close to the Earth but not exactly at the location of the Earth. A second sphere, its epicycle, would then orbit on the surface of the first sphere and the celestial body would orbit on its surface. Because this model still mismatched observations at times, even more complicated geocentric models were developed.

While the Ancient Greeks already proposed a heliocentric model for the solar system, Copernicus revived it in Europe during the 16th century. At the beginning of the 17th century, Johannes Kepler published his three laws of planetary motion which improved upon Copernicus' laws to allow for more general elliptical orbits, thereby explaining how planetary velocities vary while the planets orbit the sun. By the end of the 17th century, Isaac Newton had shown that Kepler's laws of planetary motion are a direct consequence of his more general laws of motion and gravity.

While studying the movement of solar planets allows the development of theories on planetary motion, it provides limited information on the formation of the solar system. To effectively develop theories on planet formation, it is necessary to obtain a larger sample size and snapshots at different development stages, i.e. we have to observe many more planetary systems. It has long been suspected by astronomers that the sun is not the only star harboring planets. However, because of the vast distances between stars, the relatively small size and mass of planets, and especially because of their low brightness, they have been notoriously hard to detect. The first confirmed detection of an exoplanet happened in 1992 when several terrestrial-mass planets were discovered orbiting the pulsar PSR B1257+12 (Wolszczan and Frail, 1992). Only a couple of years later the first exoplanet around a solar-type star was discovered (Mayor and Queloz, 1995). Since then nearly 5000 exoplanets have been discovered using mostly indirect methods. Figure 1.1 shows the observed exoplanets as of the writing of the thesis in a mass vs separation diagram. The data is obtained from exoplanets.org (Han et al., 2014).

The displayed exoplanets are color-coded depending on the method used

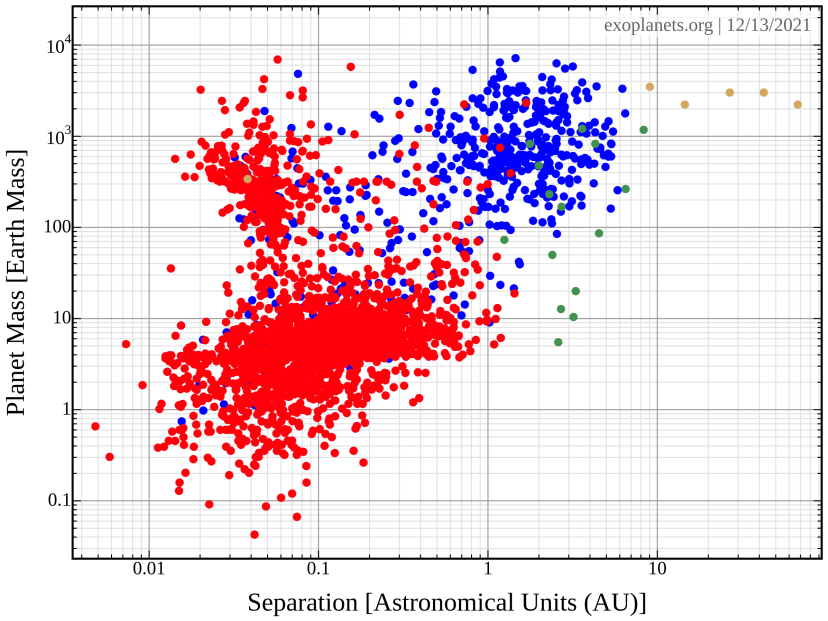

Figure 1.1: Observed exoplanet population as of 12/13/2021, data from exoplanets.org (Han et al., 2014). The x-axis is the separation to the host star and the y-axis is the mass of the planet. Error bars have been omitted for reasons of clarity. However, the errors extend over several orders of magnitude for some measurements. Red data points were observed using the transit method, blue data points using the radial velocity method, green data points using the microlensing method, and golden data points were observed through direct imaging.

to observe them: transit method (red), radial velocity (blue), microlensing (green), and direct imaging (gold). The transit method detects exoplanets by measuring the decrease in observed stellar luminosity when the planet moves between the host star and the observer. Additionally, if the transit period changes between multiple transits, one can infer that there must be an additional planet in the system that perturbs the transiting one. The radial velocity method detects exoplanets by measuring the Doppler shift of the stellar spectrum that occurs when the host star orbits the common center of mass of planet and star. The microlensing method detects exoplanets by measuring the gravitational lensing effect the planetary system has on a distant light source like a star. Direct imaging on the other hand, directly

detects exoplanets by observing the light they reflect from their host star to the observer.

As of today, several thousand exoplanets have been detected and recorded in public databases which allows their population to be analyzed statistically (Schneider, 2011; Wright et al., 2011). There are three distinct groups in the mass-separation diagram shown in figure 1.1. There is a group of terrestrial-mass planets with a relatively small separation from their host star, the so-called *super-Earths* and *mini-Neptunes*, a group of high mass, small separation planets, the so-called *hot Jupiters* and the high mass, larger separation planets, the so-called *cold Jupiters*.

Exoplanets are a valuable tool to study the formation of the planets in our own solar system by providing a larger sample size. Thereby aiding humanity in answering the age-old question of their origin and whether the earth is special in that it is capable of harboring life. However, to understand the complex process of how planets form, it is not enough to observe a large sample and perform statistical analysis, it is also crucial to observe the intermediate steps of their formation process.

1.2 Protoplanetary disks and planet formation

When a star forms from the gravitational collapse of a molecular cloud an inevitable byproduct is the formation of a protoplanetary disk. As the molecular cloud contracts, the conservation of angular momentum causes the cloud to rotate faster and forces it to flatten out. The disk around the newly formed star continues to lose angular momentum through dissipation effects such as viscosity, which causes the material of the disk to be slowly accreted by the host star (Shakura and Sunyaev, 1973). In addition to viscous transport, photoevaporation, grain growth, dust settling and dynamical interaction with objects like companions and protoplanets shape the protoplanetary disk over time. While simulations show that these disks form rapidly within $t \sim 10^4\,\mathrm{yr}$, it takes several million years for the protoplanetary disk to vanish (Yorke et al., 1993; Hueso and Guillot, 2005; Haisch et al., 2001). This formation process has a strong dependency on the angular

momentum of the cloud (Terebey et al., 1984). The wide range of observed core rotation rates, therefore, indicates a large variety of initial disk sizes and masses (Goodman et al., 1993). The long lifetimes of protoplanetary disks allow for planets to form within these disks. The formation of planets in protoplanetary disks explains why planets are usually aligned within a plane in their host star system as can be observed in the solar system. Recent observations from the Disk Substructures at High Angular Resolution Project (DSHARP) using the Atacama Large Millimeter/submillimeter Array (ALMA) have produced small-scale observations of protoplanetary disks (Andrews et al., 2018). These studies have found radial substructure in disks relevant for planet formation to be ubiquitous.

There are two common theories on how planets form within protoplanetary disks: Either by gravitational instability (Kuiper, 1951; Cameron, 1978) or core accretion (Safronov, 1972; Pollack et al., 1996). In the gravitational instability picture, the protoplanetary disk is massive enough to be self-gravitating and starts to form clumps when it cools sufficiently. These clumps then contract by cooling and continue to survive until after the lifetime of the disk. However, this model requires the protoplanetary disk to be relatively massive ($\simeq 0.1 M_\star$) and may only form massive gas giants or even secondary stars.

In the core accretion model, on the other hand, dust within the protoplanetary disk coagulates to form pebbles and planetesimals which over time grow to form protoplanetary cores (Safronov, 1972; Goldreich and Ward, 1973). These cores then gravitationally accrete gas from the protoplanetary disk they were born in. More massive cores ($M_c \sim 10\, M_{\mathrm{Earth}}$) can manage to accrete enough gas for their protoplanetary atmosphere to become self-gravitating. If the atmospheric growth surpasses the growth rate of the core, the atmosphere may then start a process called runaway gas accretion. During runaway gas accretion the atmosphere is no longer in hydrostatic equilibrium but will accrete all available gas on the orbit of the planet and –given there is enough material–, will eventually become a gas giant (Perri and Cameron, 1974; Mizuno et al., 1978; Pollack et al., 1996). If a protoplanet does not undergo runaway gas accretion, it will become a terrestrial

planet. The core accretion model is generally assumed to be responsible for most observed planets while the gravitational instability model explains the formation of companion stars and some gas giants at larger separations of $\simeq 100\,\mathrm{au}$ (Müller et al., 2018).

Theoretical studies aim to predict the characteristics/population of planetary systems from the properties of the protoplanetary disk that they were born in. To accomplish this, simulations of protoplanetary disks are initialized with measured properties, e.g. density and temperature profiles (Andrews et al., 2009, 2010; Isella et al., 2009, 2010; Andrews et al., 2018; Huang et al., 2018). Numerical models are then used to evolve the protoplanetary disk in time until a planetary system forms (Ida and Lin, 2004; Ida et al., 2008; Alibert et al., 2005; Mordasini et al., 2009; Mordasini, 2014; Emsenhuber et al., 2020). The result is then compared to observed exoplanetary systems.

When accounting for observational biases, one finds that only $0.5-1\,\%$ of solar-type stars harbor a hot Jupiter while $10-20\,\%$ of them have gas giants at a separation of $5-10\,\mathrm{au}$ (Cumming et al., 2008; Howard et al., 2010; Mayor et al., 2011). Close-in (separation less than $1\,\mathrm{au}$) super-Earths and mini-Neptunes on the other hand, are very common around solar-type stars with a frequency of $20-50\,\%$ (Mayor et al., 2011; Fressin et al., 2013; Petigura et al., 2013; Weiss et al., 2018; Winn and Fabrycky, 2015). Super-Earths and mini-Neptunes are small (several Earth radii in size) and have an atmosphere that mainly consists of hydrogen and helium. Their atmospheric composition, the short dynamical timescale, and high surface density at such small separations (Lee et al., 2014) point to an early formation (Wu and Lithwick, 2013). Therefore, these cores should have had sufficient time to accrete enough gas for their atmosphere to become self-gravitating within the lifetime of the disk. The atmosphere of the protoplanet would then eventually stop being in hydrostatic equilibrium with the circumstellar disk and enter runaway gas accretion to become a hot Jupiter (Batygin et al., 2016). Consequently, to explain the high abundance of observed super-Earths and mini-Neptunes, an efficient mechanism to prevent the onset of runaway gas accretion is needed. As possible solutions multiple mechanisms have been suggested including a

high opacity atmosphere (Lee et al., 2014), late formation (Lee and Chiang, 2015), atmosphere-disk recycling (Ormel et al., 2015b; Cimerman et al., 2017; Béthune and Rafikov, 2019; Ali-Dib et al., 2020; Moldenhauer et al., 2021) and gap opening (Fung and Lee, 2018; Ginzburg and Chiang, 2019).

For the modeling of protoplanetary atmospheres, typically one dimensional (1D) models of the radial direction are calculated for their simplicity and their relatively low requirement of computational resources. Here, a quasi-steady state is reached when the radiative cooling of the atmosphere is fully compensated by a luminosity source within the atmosphere. Typically, a fixed luminosity source is introduced at the inner boundary, i.e. at the boundary between the protoplanetary core and the atmosphere. The luminosity is justified by the accretion of solids like planetesimals and pebbles. This model results in an atmosphere that is independent of time but a function of luminosity and therefore the accretion rate of solids (Rafikov, 2006), hence the name quasi-steady state.

However, the situation changes when solid accretion terminates and the core mass is fixed. The atmosphere then stops being in a quasi-steady state and starts to contract. Instead of the fixed luminosity from the accretion of solids, the atmosphere then provides its own luminosity through Kelvin-Helmholtz contraction. Because of the early formation of super-Earths and mini-Neptunes, one can expect this situation to occur as solids will be accreted on timescales shorter than the disk lifetime. Even before the amount of solids within the disk drops to levels below the amount required to sustain this quasi-steady state, solid accretion may be halted once the pebble isolation mass is reached (Lambrechts et al., 2014; Ataiee et al., 2018; Bitsch et al., 2018). When this situation occurs, the evolution of the atmosphere is determined by the Kelvin-Helmholtz timescale. Several detailed 1D studies have shown that the Kelvin-Helmholtz timescale is a strong function of the opacity in the outer radiative zone (Ikoma et al., 2000; Lee et al., 2014; Hori and Ikoma, 2010; Chachan et al., 2021). Typically, models assume ISM-like dust-to-gas ratios and grain properties, where the opacity is predominantly determined by the dust. However, studies have argued that because grains are expected to aggregate and settle, protoplanetary atmospheres should be

modeled as grain-free and therefore with a lower opacity (Mordasini, 2014; Ormel, 2014). For a low opacity atmosphere that is not heated through the accretion of solids, analytical models have shown that the timescale to achieve runaway gas accretion drops below 1 Myr for core masses above 2 $M_\oplus$ (Hori and Ikoma, 2010). A solution to these issues might lie in hydrodynamics itself: Unlike 1D simulations, three-dimensional (3D) simulations allow energy to be resupplied by exchanging low entropy atmospheric gas with high entropy circumstellar gas without the need for a net accretion of gas.

1.3 Atmospheric recycling

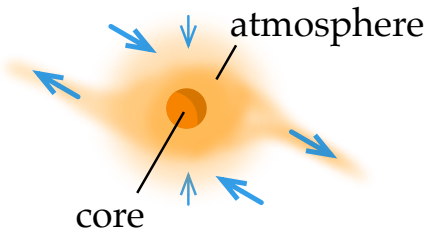

Figure 1.2: Recycling flow pattern of a protoplanetary atmosphere. Low entropy (cooled) atmospheric gas is shown in orange which is surrounded by high entropy circumstellar gas (not colored). The atmosphere exchanges gas with the protoplanetary disk at the boundary between the horseshoe orbits and the atmosphere along the orbital direction and through vertical inflow. Sketch by André Oliva.

Most 1D models of protoplanetary atmospheres explain the abundance of super-Earths and mini-Neptunes by preventing runaway gas accretion by invoking the accretion of solids or by assuming a high opacity atmosphere. While these effects certainly exist, they have to be fine-tuned such that these models reproduce the observed planet population (Emsenhuber et al., 2020). In 3D an additional effect exists that counters the cooling of the atmosphere and can thereby potentially prevent the atmosphere from entering runaway gas accretion: Atmospheric recycling. In the recycling picture, the protoplanetary atmosphere is not viewed as independent from the protoplanetary disk.

Instead, as shown in figure 1.2, high entropy circumstellar gas constantly replaces low entropy atmospheric gas and thereby reheats the atmosphere that is cooling radiatively. For geometric reasons, a recycling flow pattern is only possible in 3D. In 3D circumstellar gas enters the atmosphere through the vertical direction and can be removed through the midplane (Machida et al., 2008; Tanigawa et al., 2012; Szulágyi et al., 2016), there is no clear boundary between the protoplanetary atmosphere and the protoplanetary disk (Ormel et al., 2015b). Therefore, 1D and 2D models of protoplanetary atmospheres completely ignore atmospheric recycling. Previous studies have shown that at close-in orbits atmospheric recycling is a strong enough effect to efficiently counteract radiative cooling (Cimerman et al., 2017).

This thesis investigates atmospheric recycling for atmospheres of close-in protoplanets in great detail. Using 3D radiation hydrodynamics simulations protoplanetary atmospheres are simulated for a range of core masses, opacities, and orbital separations. For the first time, it is shown that atmospheric recycling on its own is capable of fully compensating radiative cooling at close-in separations. Additionally, the effects of the so-called headwind on the recycling of atmospheric gas are investigated. Furthermore, the recycling pattern of the atmosphere is analyzed and the atmospheric recycling is quantified by introducing and measuring the recycling timescale. To accomplish this, new post-processing techniques are introduced and refined. After the simulations have reached a thermodynamic equilibrium where radiative cooling is fully compensated by atmospheric recycling, tracer particles and tracer fluids are used to study the process.

The results presented in this thesis show that atmospheric recycling is an efficient enough mechanism to effectively prevent Kelvin-Helmholtz contraction. Close-in protoplanetary cores fail to accrete a massive enough envelope needed for the onset of runaway gas accretion when 3D effects are considered. This proves that modeling close-in protoplanetary atmospheres as isolated systems using 1D simulations is insufficient. The 3D simulations presented in this thesis show that in-situ formation of close-in gas giants is significantly more unlikely than 1D models would suggest, thereby explaining the abundance of observed close-in super-Earths and mini-Neptunes.

Chapter 2

Setup and numerics

2.1 Setup

The setup for the simulations conducted in the scope of this thesis is based on the setup used by Cimerman et al. (2017). The simulations utilize radiation-hydrodynamics (RHD) on a 3D spherical grid centered at the protoplanetary core with a core mass of M_c. Figure 2.1 shows the structure of the setup. Instead of simulating the whole circumstellar disk, only the region of the disk that surrounds the protoplanet is part of the computational domain. This allows for a high enough resolution to resolve the protoplanetary core, i.e. the inner boundary is the actual surface of the core. The outer boundary extends up to $5H$, where H is the scale height of the disk at the orbit of the planet. To properly resolve the flow of the atmosphere, the simulation utilizes a spherical grid centered around the planet. The local frame of reference orbits the star with the Keplerian frequency, $\Omega_K = \sqrt{GM_*/a^3}$, where G is the gravitational constant, M_* the stellar mass, and a the orbital separation of the planet. However, despite the spherical simulation grid, throughout this thesis, Cartesian coordinates are often used to describe the results. The x-direction points away from the star, the y-direction points in the orbital direction of the planet, and the z-direction points parallel to the rotation axis of the circumstellar disk. The origin of the Cartesian grid is the protoplanetary core.

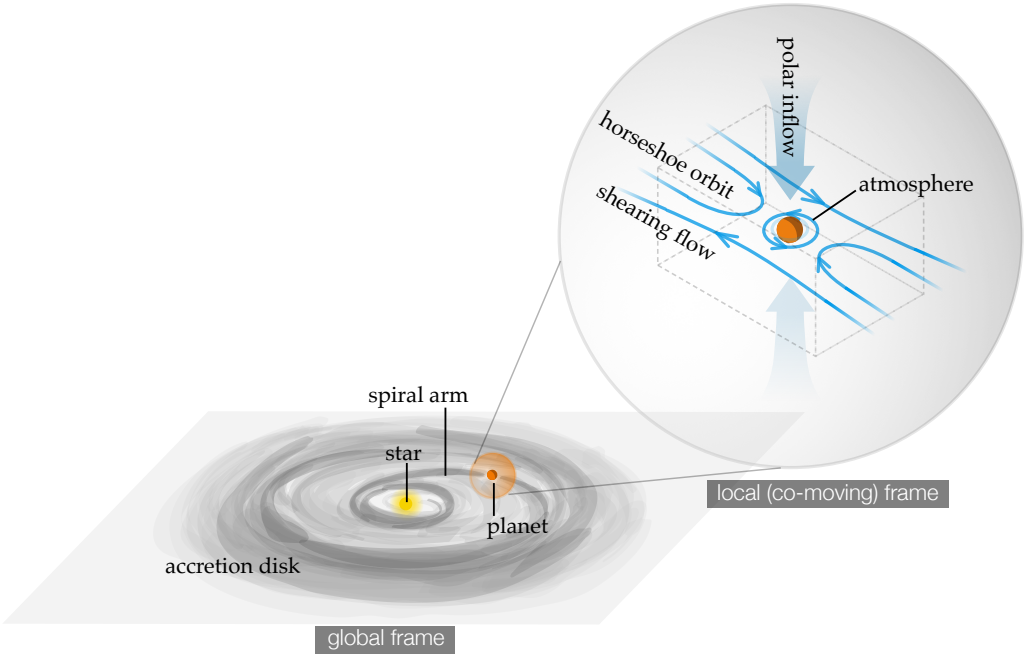

Figure 2.1: Sketch of the simulation setup. The simulation domain is a local sphere centered at the protoplanetary core. Note that the structure in the "global frame" is exaggerated. The core masses used in this thesis have little effect on the disk, thereby justifying this local approach. Sketch by André Oliva.

The computational domain is initialized with a vertically stratified density, $\rho = \rho_0 \exp(-0.5z^2/H^2)$, and a uniform temperature, T_0. The velocity field is set to the linearized shearing flow of the circumstellar disk, $\boldsymbol{v}_\infty = -\frac{3}{2}x\Omega_K \boldsymbol{e}_y$. Closer to the star, i.e. negative values for x, the gas orbits the star faster than the planet, and further away the gas orbits the star more slowly than the planet. The values the computational domain is initialized with are also used for the outer boundary condition as this is the boundary with the circumstellar disk. The inner boundary uses a reflective boundary condition because of the solid protoplanetary core, i.e all fluxes vanish at the surface of the core. The size of the protoplanetary core is calculated from the core mass, assuming a mean core density of $\rho_c = 5\,\mathrm{g/cm^3}$.

After the simulation is started, several external forces perturb the initial

conditions. The protoplanetary core exerts a gravitational force on the gas,

$$\boldsymbol{a}_p = -GM_c/r^2. \tag{2.1}$$

Here, M_c is the mass of the core and r is the distance of the respective cell from the core. Because the computational domain moves with the planetary core and is therefore not an inertial frame of reference, fictitious forces have to be included: Firstly, the Coriolis force,

$$\boldsymbol{a}_{\mathrm{cor}} = -2\boldsymbol{\Omega}_K \times \boldsymbol{v}, \tag{2.2}$$

is included, where $\boldsymbol{\Omega}_K = \Omega_K \boldsymbol{e}_z$. Secondly, the stellar acceleration and the centrifugal accelerations can be combined into the linearized tidal force,

$$\boldsymbol{a}_{\mathrm{tid}} = 3\Omega_K^2 x \cdot \boldsymbol{e}_x. \tag{2.3}$$

Because of the radial pressure gradient in the circumstellar disk, the gas orbits the star at sub-Keplerian speeds. However, as the force from the pressure gradient is negligible for solid bodies like planets, they orbit the star faster than the gas. From the point of view of the planet, a so-called headwind occurs. Because of the local nature of the simulations in this thesis, the pressure gradient in the disk is not captured. It is therefore necessary to explicitly add the headwind parameter. For simulations that include a headwind an additional velocity is added at the boundary,

$$\boldsymbol{v}_{\mathrm{hw}} = \mathcal{M}_{\mathrm{hw}} \cdot c_{\mathrm{iso}}, \tag{2.4}$$

where $\mathcal{M}_{\mathrm{hw}}$ is the Mach number of the headwind and c_{iso} the isothermal sound speed of the gas.

To prevent initial shocks, the gravity of the core as well as the headwind is switched on using an injection factor,

$$\alpha_{\mathrm{inj}}(t) = 1 - \exp\left(-\frac{1}{2}\frac{t^2}{t_{\mathrm{inj}}^2}\right). \tag{2.5}$$

For all simulations the injection time, t_{inj}, is set to $4\,\Omega_K^{-1}$. However, one additional simulation with an injection time of $400\,\Omega_K^{-1}$ was conducted to confirm that the injection time does not affect the long-term evolution of the simulation.

The simulations in this thesis follow Lee et al. (2014) and Cimerman et al. (2017) and use the density and temperature profile from the Minimum Mass Extrasolar Nebula (MMEN, Chiang and Laughlin, 2013):

$$\rho_{\mathrm{MMEN}} = 6 \cdot 10^{-6} \cdot \left(\frac{a}{0.1\,\mathrm{au}}\right)^{-2.9} \mathrm{g/cm^3} \tag{2.6}$$

$$T_{\mathrm{MMEN}} = 1000 \cdot \left(\frac{a}{0.1\,\mathrm{au}}\right)^{-3/7} \mathrm{K} \tag{2.7}$$

From these profiles the disk height, H, and aspect ratio, h, are given by

$$H = 0.002\,\mathrm{au}\left(\frac{a}{0.1\,\mathrm{au}}\right)^{9/7}, \tag{2.8}$$

$$h = 0.02\left(\frac{a}{0.1\,\mathrm{au}}\right)^{2/7}. \tag{2.9}$$

From the temperature and density gradient the Mach number of the headwind can be calculated to

$$\mathcal{M}_{hw} = 0.033\left(\frac{a}{0.1\,\mathrm{au}}\right)^{2/7}. \tag{2.10}$$

The Mach number of the headwind increases with the distance to the star. However, in order to exaggerate the effects of the headwind, in this thesis $\mathcal{M}_{\mathrm{hw}} = 0.1$ is used for all simulations that include a headwind.

The standard opacity used for the simulations is $\kappa = 10^{-4}\,\mathrm{cm^2 g^{-1}}$. This opacity is several orders of magnitude lower than a realistic opacity Ferguson et al. (2005). An artificially low opacity ensures that the cooling timescale is sufficiently short to rule out that the limited simulation time prevents the atmosphere from cooling. However, because only the optical depth, $\tau = \int \kappa\rho\,\mathrm{d}s$, is relevant for the radiation solver (section 2.3) and the density is only a scaling parameter in the hydrodynamics (section 2.2), changing the opacity has the same effect as changing the density to the resulting

flow structure. All things considered, the free simulation parameters are the initial specific optical depth, $\kappa\rho_0$, the rotation frequency of the planet around the star, Ω_K, the background temperature, T_0, the headwind Mach number, $\mathcal{M}_{\mathrm{hw}}$, and the core mass M_c. All simulations assume a solar mass host star, $M_* = M_\odot$, and use the separation a instead of $\Omega_K = \sqrt{GM_*/a^3}$ as the parameter determining the stellar interaction.

The naming of the simulations works as follows: Setups are named MX where X is the core mass in M_{Earth}. If the setup features a non-standard initial $\kappa\rho_0$ ($6 \cdot 10^{-10}\,\mathrm{cm}^{-1}$), $\pm$Y is appended which states the deviation in orders of magnitude, Y. For setups that include a headwind, -HW is appended. The suffix L stands for a lower resolution (half in each direction) compared to the standard resolution of 128x32x128 ($N_r \times N_\theta \times N_\varphi$). Additionally, the suffix T indicates that the standard temperature of 1000 K was used despite the change in orbital separation, i.e. the temperature at 0.1 au was used instead of the disk temperature at that location. The prefixes 03AU and 1AU stand for a separation of 0.3 au and 1 au respectively. All other simulations use the standard separation of 0.1 au.

Name	resolution	$\kappa\rho_0$ in cm^{-1}	a in au	T_0 in K	$\mathcal{M}_{\mathrm{hw}}$	M_c in M_{Earth}
M1	normal	$6 \cdot 10^{-10}$	0.1	1000	0	1
M2	normal	$6 \cdot 10^{-10}$	0.1	1000	0	2
M5	normal	$6 \cdot 10^{-10}$	0.1	1000	0	5
M10	normal	$6 \cdot 10^{-10}$	0.1	1000	0	10
M1-HW	normal	$6 \cdot 10^{-10}$	0.1	1000	0.1	1
M2-HW	normal	$6 \cdot 10^{-10}$	0.1	1000	0.1	2
M5-HW	normal	$6 \cdot 10^{-10}$	0.1	1000	0.1	5
M10-HW	normal	$6 \cdot 10^{-10}$	0.1	1000	0.1	10
M1-1D	normal	$6 \cdot 10^{-10}$	0.1	1000	0	1
M1+1	normal	$6 \cdot 10^{-9}$	0.1	1000	0	1
M1-1	normal	$6 \cdot 10^{-11}$	0.1	1000	0	1
M1-L	low	$6 \cdot 10^{-10}$	0.1	1000	0	1
03AU-M2	normal	$6 \cdot 10^{-10}$	0.3	624	0	2
03AU-M2-L	low	$6 \cdot 10^{-10}$	0.3	624	0	2
03AU-M2-L-T	low	$6 \cdot 10^{-10}$	0.3	1000	0	2
03AU-M2-1-L	low	$6 \cdot 10^{-11}$	0.3	624	0	2
03AU-M2-2-L	low	$6 \cdot 10^{-12}$	0.3	624	0	2
03AU-M2-3-L	low	$6 \cdot 10^{-13}$	0.3	624	0	2
03AU-M10-L	low	$6 \cdot 10^{-10}$	0.3	624	0	10
03AU-M10-L-T	low	$6 \cdot 10^{-10}$	0.3	1000	0	10
03AU-M10-1-L	low	$6 \cdot 10^{-11}$	0.3	624	0	10
03AU-M10-2-L	low	$6 \cdot 10^{-12}$	0.3	624	0	10
03AU-M10-3-L	low	$6 \cdot 10^{-13}$	0.3	624	0	10
1AU-M2	normal	$6 \cdot 10^{-10}$	1	373	0	2
1AU-M2-1-L	low	$6 \cdot 10^{-11}$	1	373	0	2
1AU-M2-2-L	low	$6 \cdot 10^{-12}$	1	373	0	2
1AU-M2-3-L	low	$6 \cdot 10^{-13}$	1	373	0	2
1AU-M10-L	low	$6 \cdot 10^{-10}$	1	373	0	10
1AU-M10-3-L	low	$6 \cdot 10^{-13}$	1	373	0	10

Table 2.1: Overview of the simulation setups. The M1-1D simulation uses the same parameters as M1 but includes only the radial dimension.

2.2 Hydrodynamics

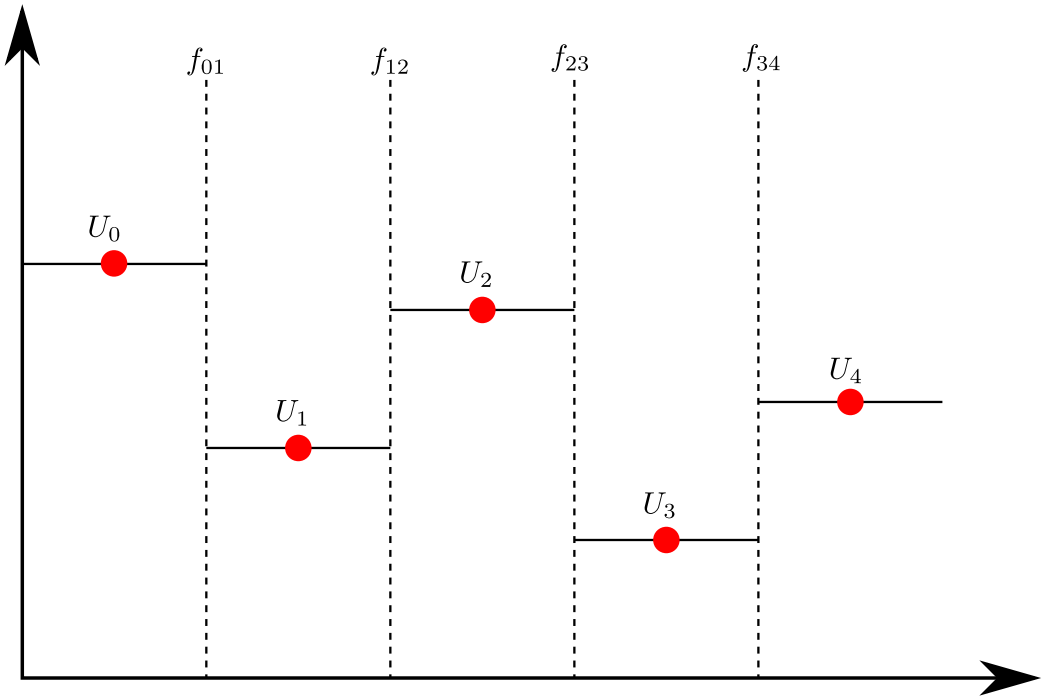

Figure 2.2: The Riemann problem. U is a conserved quantity defined on a grid. At the boundaries between two cells, a discontinuity occurs. Solving the Riemann problem results in the fluxes at the boundaries that are then used in the advection equation of that quantity to evolve it in time.

For the simulations in this thesis the hydrodynamics module of the open-source code PLUTO (Mignone et al., 2007, 2012), version 4.1, is used. PLUTO solves the following conservation equations: Conservation of mass, momentum and total energy,

$$\frac{\partial \rho}{\partial t} + \nabla \cdot (\rho \boldsymbol{v}) = 0, \tag{2.11}$$

$$\frac{\partial \rho \boldsymbol{v}}{\partial t} + \nabla(\rho \boldsymbol{v} \cdot \boldsymbol{v} + p) = \rho \boldsymbol{a}, \tag{2.12}$$

$$\frac{\partial E}{\partial t} + \nabla \cdot [(E + p) \cdot \boldsymbol{v}] + \nabla \cdot \boldsymbol{F} = \rho \boldsymbol{v} \cdot \boldsymbol{a}. \tag{2.13}$$

Here, ρ is the gas density, p the gas pressure, $\boldsymbol{v}$ the gas velocity and $E = E_{\mathrm{th}} + E_{\mathrm{kin}}$ the total energy of the gas. $\boldsymbol{a}$ represents external accelerations

and $\boldsymbol{F}$ is the radiation flux from the flux-limited diffusion solver (see section 2.3). The set of equations is completed by an equation of state $p = p(\rho, E)$.

Equations 2.11 to 2.13 are of the form

$$\frac{\partial U}{\partial t} + \nabla \cdot T(U) = S(U), \tag{2.14}$$

where U is the conserved quantity, $\nabla \cdot T(U)$ its transport term and $S(U)$ its source term. In PLUTO the computational domain is divided into cells, for each cell a single value of U is stored. A cell represents a finite volume V_i with the volume average of the tracked quantity U_i, hence the name of the scheme: "finite volumes". As each cell is represented by a single value, discontinuities arise at the boundaries between the cells (see figure 2.2). An initial value problem of a conservation equation with piecewise constant initial values and a single discontinuity is called a Riemann problem after Bernhard Riemann. To evolve the solution in time using the transport term, the flux, f_{ij}, at the boundary between U_i and U_j has to be calculated. This is achieved by solving the Riemann problem (see Toro (1999) for details). However, because finding an exact solution to the Riemann problem is computationally expensive and accuracy is limited by the finite grid resolution, multiple faster approximate solvers have been developed. For the hydrodynamics simulations throughout this thesis, the Roe approximate Riemann solver was used (Roe, 1986). Ormel et al. (2015a) found that the Roe solver introduces a relatively low numerical viscosity compared to other solvers. Such a numerical viscosity is usually undesired because of its artificial nature. Using the calculated fluxes the solution is then updated in time,

$$U_i^{n+1} = U_i^n - \frac{\Delta t}{\Delta x}(f_{i-1,i} - f_{i,i+1}). \tag{2.15}$$

The source term from equation 2.14 can either be included during the advection step in equation 2.15 or be added separately (operator splitting).

2.3 Radiation transport

The radiative cooling of the protoplanetary atmosphere is modeled using the flux-limited diffusion (FLD) approximation (Levermore and Pomraning, 1981). The FLD solver used throughout this thesis with the PLUTO hydrodynamics code was implemented by Kuiper et al. (2010) and Kuiper et al. (2020).

In the FLD approximation the radiation flux, $\boldsymbol{F}$, is calculated using a diffusion equation. In the following, its calculation is outlined. The time evolution of the internal energy of the gas, $E_{\rm int}$, and the radiative energy, $E_{\rm rad}$ is given by the following differential equations:

$$\frac{\partial E_{\rm int}}{\partial t} + \nabla \cdot (E_{\rm int}\boldsymbol{v}) = Q^{+} + \Lambda, \tag{2.16}$$

$$\frac{\partial E_{\rm rad}}{\partial t} + \nabla \cdot (E_{\rm rad}\boldsymbol{v}) = -\nabla \cdot \boldsymbol{F} - \Lambda. \tag{2.17}$$

Here, $\boldsymbol{v}$ is the velocity of the gas, Q^{+} is the heating source term of the gas, $\boldsymbol{F}$ is the radiation flux and Λ is the energy coupling between both fields, i.e. the radiative heating or cooling of the gas. The heating source term, Q^{+}, includes adiabatic compression, $-P\nabla\cdot\boldsymbol{u}$, and other heating mechanisms that depend on the physics included, e.g. viscous heating. Λ is given by

$$\Lambda = \rho c \kappa \left(a T^{4} - E_{\rm rad} \right), \tag{2.18}$$

where ρ is the density of the gas, c the speed of light, κ the opacity, T the temperature of the gas and a the radiation constant.

Adding up the differential equations 2.16 and 2.17 yields

$$\frac{\partial (E_{\rm int} + E_{\rm rad})}{\partial t} + \nabla \cdot (E_{\rm int}\boldsymbol{v}) + \nabla \cdot (E_{\rm rad}\boldsymbol{v}) = -\nabla \cdot \boldsymbol{F} + Q^{+}. \tag{2.19}$$

The first transport term, $\nabla \cdot (E_{\rm int}\boldsymbol{v})$, is already advected by PLUTO when equation 2.13 is solved. The second transport term, $\nabla \cdot (E_{\rm rad}\boldsymbol{v})$ can either be ignored because of $E_{\rm rad} \ll E_{\rm int}$, or be advected separately (operator split-

ting). When omitting these two terms one obtains

$$\frac{\partial(E_{\text{int}} + E_{\text{rad}})}{\partial t} = -\nabla \cdot \boldsymbol{F} + Q^{+}. \tag{2.20}$$

Furthermore, assuming that the gas and radiation are in a local thermal equilibrium, i.e. $\Lambda = 0$ and $T_{\text{gas}} = T_{\text{rad}} = T$, the radiation energy is given by

$$E_{\text{rad}} = aT^4. \tag{2.21}$$

This assumption is justified in the optically thick regime ($\tau = \int \kappa\rho \, \mathrm{d}s > 1$). Because the internal energy of the gas is a function of the temperature,

$$E_{\text{int}} = c_V \rho T, \tag{2.22}$$

its time derivative can be expressed using the time derivative of the radiation energy:

$$\frac{\partial E_{\text{int}}}{\partial t} = c_V \rho \partial \frac{\partial E_{\text{int}}}{\partial t} = \frac{c_V \rho}{4aT^3} \frac{\partial E_{\text{rad}}}{\partial t}. \tag{2.23}$$

Here, c_V is the specific heat capacity of the gas at constant volume. This treatment is possible because the same temperature is assumed for the internal energy of the gas and for the radiation energy which is why this approximation is often referred to as *one-temperature FLD*.

Equation 2.20 can then be written as a diffusion equation,

$$\frac{\partial E_{\text{rad}}}{\partial t} = f_c \left(-\nabla \cdot \boldsymbol{F} + Q^{+}\right), \tag{2.24}$$

where $f_c = (c_V \rho/(4aT^3) + 1)^{-1}$. In the FLD approximation the radiation flux is given by

$$\boldsymbol{F} = -\frac{\lambda c}{\kappa \rho}, \tag{2.25}$$

where λ is a so-called flux limiter. It ensures that in the free-streaming limit ($R := |\nabla E_{\text{rad}}|/(\kappa\rho|E_{\text{rad}}|) \to \infty$) and in the diffusion limit ($R \to 0$) the

radiation flux approaches the correct values,

$$\boldsymbol{F} = -cE_{\mathrm{rad}}\frac{\nabla E_{\mathrm{rad}}}{|E_{\mathrm{rad}}|} \qquad R \to \infty, \tag{2.26}$$

$$\boldsymbol{F} = -\frac{c}{3\kappa\rho}\nabla E_{\mathrm{rad}} \qquad R \to 0. \tag{2.27}$$

Levermore and Pomraning (1981) found $\lambda(R) = 1/R\,(\coth(R) - 1/R)$ to be a suitable limiter. However, for faster computation, its rational approximation $\lambda(R) = (2 + R)/(6 + 3R + R^2)$ is used. The radiation flux calculated from solving equation 2.24 is then used in equation 2.13 to update the energy of the gas.

2.4 Post-processing

The simulations are run until they reach a thermodynamic equilibrium where atmospheric recycling fully compensates for radiative cooling. To investigate the recycling process, the flow pattern is analyzed in post-processing using two techniques: Tracer particles and tracer fluids. Tracer particles are a computationally inexpensive method when the velocity field has stopped evolving in time. When the velocity field continues to evolve in time, it is better to use a tracer fluid where the calculated advection flux for the density can be reused to advect the tracer fluid. However, this requires significantly more computational resources as the hydrodynamics has to be evolved as well.

2.4.1 Tracer particles

After a thermodynamic equilibrium is reached, tracer particles can be introduced to measure the recycling timescale. Tracer particles are massless particles that directly follow the gas. Here, we define the recycling timescale as the time it takes the gas to leave the Hill sphere. The Hill radius, $R_{\mathrm{Hill}} = a\sqrt[3]{\frac{M_c}{3M_*}}$, is a spherical approximation for the region where the gravity of the core dominates over the stellar gravity. It therefore serves as a good upper bound for the size of the atmosphere. Tracer particles are introduced everywhere inside the Hill sphere and are then integrated along streamlines. The time they

take to leave the Hill sphere is then the recycling timescale at their starting position.

Initial testing showed that the measured recycling time is very sensitive to the starting position, i.e. a small change in the starting position may cause a large change in the recycling time. To smooth out the result, adjacent tracer particles are grouped and the median of their recycling time is calculated. This approach is justified because they track the flow pattern of a gas that naturally mixes.

To calculate the recycling time using tracer particles a new particle integrator was developed as part of this thesis. The particle integrator is described in detail in chapter 3.

2.4.2 Tracer fluid

Another method to track the recycling of the gas is the usage of a tracer fluid. A tracer fluid is a scalar quantity Ψ that is evolved using the advection equation,

$$\frac{\partial \Psi}{\partial t} + \nabla \cdot (\Psi \boldsymbol{v}) = 0. \tag{2.28}$$

Here, $\boldsymbol{v}$ is the velocity of the gas. Note that equation 2.28 is the same as the advection equation of the gas density 2.15 using the same velocity. The tracer fluid therefore mimics the flow of the gas without altering it.

In order to track the recycling of the gas, after the simulation has reached a thermomdynamic equilibrium the Hill sphere is filled with a tracer fluid density of unity,

$$\Psi_0(r) = \begin{cases} 1, & r < R_{\text{Hill}}, \\ 0, & r \geq R_{\text{Hill}}. \end{cases} \tag{2.29}$$

The choice of the Hill sphere is arbitrary, any radius larger than the (unknown) atmospheric radius works equally well. However, the Hill radius is easy to calculate and is a good upper bound for the size of the atmosphere as it is the region where the gravity of the core dominates over the stellar

gravity. Tracer fluids add little overhead because they are advected using the same fluxes as the density field. Therefore, no new fluxes have to be calculated when a tracer fluid is added.

The simulation is then continued with the added tracer fluid. The regions inside R_{Hill} that are replenished with circumstellar gas will decrease their tracer fluid concentration as the gas is replaced with gas from outside R_{Hill} that has a tracer concentration of zero. The tracer concentration at a fixed time after the tracer fluid was added then serves as a measurement for the recycling efficiency. A lower tracer concentration indicates a shorter recycling time.

Chapter 3

Particle integrator

To calculate the recycling timescale, it is necessary to closely track the motion of the gas. One possibility to achieve this is to use tracer particles. Laboratory experiments also utilize tracer particles to visualize and measure the flow of fluids. The tracer particle integrator described in this chapter was implemented from scratch as part of this thesis.

3.1 Tracer particles

Tracer particles are massless particles that follow the gas along streamlines. The corresponding differential equation for the location of the tracer particles that has to be solved reads as

$$\frac{\mathrm{d}\boldsymbol{x}_{\mathrm{par}}}{\mathrm{d}t} = \boldsymbol{v}_{\mathrm{gas}}(\boldsymbol{x}_{\mathrm{par}}, t). \tag{3.1}$$

Here, $\boldsymbol{x}_{\mathrm{par}}$ is the position of the tracer particle, and $\boldsymbol{v}_{\mathrm{gas}}$ is the velocity field of the gas.

For simulations that result in a true steady state, i.e. the velocity field becomes constant in time, this can be done in post-processing. Here, the the differential equation that describes the motion of the tracer particles

simplifies to

$$\frac{\mathrm{d}\boldsymbol{x}_{\mathrm{par}}}{\mathrm{d}t} = \boldsymbol{v}_{\mathrm{gas}}(\boldsymbol{x}_{\mathrm{gas}}), \tag{3.2}$$

as there is no time dependency for $\boldsymbol{v}_{\mathrm{gas}}$. This makes solving the hydrodynamics equations during the integration of the particles unnecessary and thus significantly reduces the computational resources needed. There are two quantities the implemented particle integrator can track: the time it takes for a particle to reach a specified distance from the origin of the coordinate system and the trajectory of the particle.

3.2 Implementation

The implementation of the tracer particle integrator consists of three main components: Integration, interpolation, and parallelization. The integrator advances the solution using the differential equation from equation 3.2. For the integration step, the integrator has to be able to access the gas velocity at arbitrary locations. However, because the hydrodynamics solution is calculated on a grid, it is necessary to interpolate the velocity field to arbitrary locations between the grid points. Finally, parallelization of the particle integrator is necessary to utilize multiple CPU cores to be able to integrate many tracer particles in a reasonable amount of time. A higher number of tracer particles results in a more detailed analysis of the flow pattern.

3.2.1 Runge-Kutta-Fehlberg method

The particle integrator uses the Runge-Kutta-Fehlberg (RKF45) integration method which was developed by Fehlberg in 1969 (Fehlberg, 1969). The RKF45 method is an explicit 5th-order scheme with an adaptive step size where the truncation error is estimated using a 4th-order scheme. First, the

0						
1/4	1/4					
3/8	3/32	9/32				
12/13	1932/2197	-7200/2197	7296/2197			
1	439/216	-8	3680/513	-845/4104		
1/2	-8/27	2	-3544/2565	1859/4104	-11/40	
RK4	25/216	0	1408/2565	2197/4104	-1/5	0
RK5	16/135	0	6656/12825	28561/56430	-9/50	2/55

Table 3.1: Butcher tableau for the Runge-Kutta-Fehlberg (RKF45) method formula 2 (Fehlberg, 1969). The RK4 and the RK5 solutions use the same slopes which considerably reduces the computation time.

4th- and 5th-order solutions for the next time step, t', are calculated:

$$t' = t + \Delta t \tag{3.3}$$

$$\boldsymbol{x}(t') = \boldsymbol{x}_4(t + \Delta t) + \mathcal{O}((\Delta t)^5) \tag{3.4}$$

$$\boldsymbol{x}(t') = \boldsymbol{x}_5(t + \Delta t) + \mathcal{O}((\Delta t)^6) \tag{3.5}$$

The difference between both approximations is an estimate for the leading (fifth-order) truncation error,

$$\mathrm{TE} \approx |\boldsymbol{x}_5(t + \Delta t) - \boldsymbol{x}_4(t + \Delta t)|. \tag{3.6}$$

The truncation error can then be used to calculate the required step size for a given tolerance ε:

$$s = \left(\frac{\varepsilon}{2|\boldsymbol{x}_4 - \boldsymbol{x}_5|} \right)^{1/5} \tag{3.7}$$

$$\Delta t_{\mathrm{new}} = s \cdot \Delta t \tag{3.8}$$

If $s < 1$, the step size, Δt, was not small enough for the truncation error to be less than ε and the time step is therefore repeated using the new step size, Δt_{new}. However, if $s \geq 1$, the current step size was sufficient and the calculated new step size, Δt_{new}, is used for the next time step and the current solution is updated using the 5th-order result, $\boldsymbol{x}(t') = \boldsymbol{x}_5(t + \Delta t)$.

For this implementation of the tracer particle integrator, the RKF45 method formula 2 is used (Fehlberg, 1969). The coefficients of this method are shown as an extended Butcher tableau in table 3.1. Using these coefficients the slopes calculate to:

$$\boldsymbol{k}_1 = \boldsymbol{f}\left(t, \boldsymbol{x}(t)\right), \tag{3.9}$$

$$\boldsymbol{k}_2 = \boldsymbol{f}\left(t + \frac{1}{4}\Delta t, \boldsymbol{x}(t) + \Delta t \cdot \frac{1}{4}\boldsymbol{k}_1\right), \tag{3.10}$$

$$\boldsymbol{k}_3 = \boldsymbol{f}\left(t + \frac{3}{8}\Delta t, \boldsymbol{x}(t) + \Delta t \left[\frac{3}{32}\boldsymbol{k}_1 + \frac{9}{32}\boldsymbol{k}_2\right]\right), \tag{3.11}$$

$$\boldsymbol{k}_4 = \boldsymbol{f}\left(t + \frac{12}{13}\Delta t, \boldsymbol{x}(t) + \Delta t \left[\frac{1932}{2197}\boldsymbol{k}_1 - \frac{7200}{2197}\boldsymbol{k}_2 + \frac{7296}{2197}\boldsymbol{k}_3\right]\right), \tag{3.12}$$

$$\boldsymbol{k}_5 = \boldsymbol{f}\left(t + \Delta t, \boldsymbol{x}(t) + \Delta t \left[\frac{439}{216}\boldsymbol{k}_1 - 8\boldsymbol{k}_2 + \frac{3680}{513}\boldsymbol{k}_3 - \frac{845}{4104}\boldsymbol{k}_4\right]\right), \tag{3.13}$$

$$\boldsymbol{k}_6 = \boldsymbol{f}\left(t + \frac{1}{2}\Delta t, \boldsymbol{x}(t) + \Delta t \left[-\frac{8}{27}\boldsymbol{k}_1 + 2\boldsymbol{k}_2 - \frac{3544}{2565}\boldsymbol{k}_3 + \frac{1859}{4104}\boldsymbol{k}_4 - \frac{11}{40}\boldsymbol{k}_5\right]\right). \tag{3.14}$$

The calculated slopes are then used to obtain the 4th- and 5th-order solutions,

$$\boldsymbol{x}_4(t + \Delta t) = \Delta t \left[\frac{25}{216}\boldsymbol{k}_1 + \frac{1408}{2565}\boldsymbol{k}_3 + \frac{2197}{4104}\boldsymbol{k}_4 - \frac{1}{5}\boldsymbol{k}_5\right], \tag{3.15}$$

$$\boldsymbol{x}_5(t + \Delta t) = \Delta t \left[\frac{16}{135}\boldsymbol{k}_1 + \frac{6656}{12825}\boldsymbol{k}_3 + \frac{28561}{56430}\boldsymbol{k}_4 - \frac{9}{50}\boldsymbol{k}_5 + \frac{2}{55}\boldsymbol{k}_6\right]. \tag{3.16}$$

The advantage of the RKF45 method is that the 4th- and 5th-order schemes share their slopes, $\boldsymbol{k}_i$. Therefore, the additional 4th-order solution which is used to estimate the truncation error is computationally inexpensive.

3.2.2 Interpolation

The velocity field of the gas from PLUTO is arranged on a grid, $\boldsymbol{x}_i$. It is therefore necessary to interpolate the data to the current location of the tracer particle, $\boldsymbol{x}$. Because of the regular grid that PLUTO uses, every point

except if it is located at the edge of the domain has two adjacent grid points in each direction. For a three-dimensional grid, there are therefore up to eight points to interpolate from. For writing down the interpolation scheme the coordinates of the grid points are labeled as $\boldsymbol{x}_{ijk}$ and the respective velocity as $\boldsymbol{v}_{ijk}$, where $i, j, k \in [0, 1]$. Here, 0 denotes that the grid point is to the left and 1 denotes that the grid point is to the right of the tracer particle in the respective direction. The letter i represents the radial direction, the letter j the polar direction, and the letter k the azimuthal direction. The particle integrator supports inverse distance weighted interpolation as well as linear interpolation. Testing showed that the trajectories of the tracer particles only differ within the error margin given by the resolution of the grid when switching between both interpolation schemes. However, inverse distance weighted interpolation is significantly slower as it requires the calculation of a square root. Therefore, for the results in this work, only linear interpolation was used for performance reasons.

Inverse Distance Weighted Interpolation

The inverse distance weighted interpolation is the weighted average of all adjacent points where the weight is the inverse of the distance to the tracer particle (Shepard, 1968). If the tracer particle is currently at an edge of the domain and thus only has one neighbor in the respective direction, the weighted average is simply calculated using less than eight points. If the distance to one of the grid points is zero, the value of this respective point is used. This can happen, for example, when initializing the location of the tracer particle using the coordinates of a grid point. The interpolated velocity is given by

$$\boldsymbol{v}(\boldsymbol{x}) = \frac{\sum_{i,j,k\in[0,1]} w_{ijk}\boldsymbol{v}_{ijk}}{\sum_{i,j,k\in[0,1]} w_i}, \tag{3.17}$$

$$w_{ijk} = \frac{1}{|\boldsymbol{x} - \boldsymbol{x}_{ijk}|}, \tag{3.18}$$

where w_{ijk} is the weight of the respective grid point.

Linear Interpolation

For linear interpolation, linear polynomials are used to interpolate the quantity to points between the grid points, i.e. the interpolated values lie on a line between the original points. In three dimensions this needs to be done for each direction, halving the number of values in each step. If the tracer particle is currently at an edge of the domain, interpolation in this respective direction can simply be omitted, i.e. in this case nearest-neighbor interpolation is used in this direction.

First, the distance ratios are calculated for each direction,

$$r_d = \frac{r - r_0}{r_1 - r_0}, \tag{3.19}$$

$$\theta_d = \frac{\theta - \theta_0}{\theta_1 - \theta_0}, \tag{3.20}$$

$$\varphi_d = \frac{\varphi - \varphi_0}{\varphi_1 - \varphi_0}, \tag{3.21}$$

where r, θ, φ are the coordinates of tracer particle and r_0, θ_0, φ_0 and r_1, θ_1, φ_1 are the coordinates of the grid points to the left and to the right of the tracer particle respectively. Then, the values from the eight grid points are interpolated in the radial direction which results in four new, interpolated values:

$$\boldsymbol{v}_{00} = \boldsymbol{v}_{000} + r_d(\boldsymbol{v}_{100} - \boldsymbol{v}_{000}), \tag{3.22}$$

$$\boldsymbol{v}_{01} = \boldsymbol{v}_{001} + r_d(\boldsymbol{v}_{101} - \boldsymbol{v}_{001}), \tag{3.23}$$

$$\boldsymbol{v}_{10} = \boldsymbol{v}_{010} + r_d(\boldsymbol{v}_{110} - \boldsymbol{v}_{010}), \tag{3.24}$$

$$\boldsymbol{v}_{11} = \boldsymbol{v}_{011} + r_d(\boldsymbol{v}_{111} - \boldsymbol{v}_{011}). \tag{3.25}$$

The resulting values are then interpolated linearly in the polar direction:

$$\boldsymbol{v}_0 = \boldsymbol{v}_{00} + \theta_d(\boldsymbol{v}_{10} - \boldsymbol{v}_{00}), \tag{3.26}$$

$$\boldsymbol{v}_1 = \boldsymbol{v}_{01} + \theta_d(\boldsymbol{v}_{11} - \boldsymbol{v}_{01}). \tag{3.27}$$

Finally, linear interpolation along the azimuthal direction results in the in-

terpolated value at the wanted location, $\boldsymbol{x}$,

$$\boldsymbol{v}(\boldsymbol{x}) = \boldsymbol{v}_0 + \varphi_d(\boldsymbol{v}_1 - \boldsymbol{v}_0). \tag{3.28}$$

3.2.3 Parallelization

For a detailed analysis of the recycling timescale in three dimensions, it is necessary to use a large number of tracer particles. For the run time to be still acceptable, it is therefore crucial to integrate these tracer particles in parallel. As the tracer particles are independent of each other, during the integration process there is no communication needed. However, the tracer particles that need to be integrated have to be distributed efficiently across the available computational resources. The naive approach of simply distributing the particles evenly across all available cores does not work. Some tracer particles take significantly longer to integrate until they reach the specified escape distance. Therefore, if all particles were distributed evenly across the cores, some cores would finish much earlier than others. These cores would then be idle until the other cores have finished which would waste computational resources. Instead, the particle integrator implemented uses queues to efficiently distribute packages of tracer particles to be integrated across the available cores. The overhead caused by the coordination to distribute these packages correctly is negligible compared to the total execution time while the speed up from the efficient distribution is enormous.

The implemented particle integrator uses a hybrid parallelization approach using multithreading and multiple processes as sketched in figure 3.2. The integration of the tracer particles takes place in *worker threads*. Multiple worker threads and a single *local manager thread* form a process. Instead of a local manager thread, the first process has a *global manager thread* which also coordinates the other local manager threads. The threads within a process communicate and avoid race conditions using atomic variables, condition variables and share their memory spaces. The different processes communicate using the Message Passing Interface (MPI) which also enables processes to communicate across machines over the network. This parallelization lay-

out allows for efficient use of the available computational resources as it closely fits the underlying compute architecture. Modern compute architectures consist of non-uniform memory access (NUMA) nodes. Each NUMA node, in turn, consists of multiple Central Processing Unit (CPU) cores and their closest memory bank. It is common for a single CPU socket to house multiple NUMA nodes. To efficiently utilize the underlying architecture, each NUMA node runs its own process. Thereby ensuring that the worker threads have direct access to their memory. At the same time, the use of multiple processes communicating using MPI allows running the particle integrator on multiple CPU sockets and even multiple machines, i.e. on cluster computers commonly used in high-performance computing (HPC).

Global Manager Thread

The responsibility of the global manager is to supply the local managers with packages of particles to integrate, its flowchart is displayed in figure 3.3. The tracer particles to be integrated are divided into packages. The global manager thread maintains a queue of packages that is initially filled with all packages, i.e. contains all particles. However, to save on memory and communication bandwidth, only the IDs of the packages are saved in the queue. After initialization, the global manager thread continuously listens for requests from local manager threads through MPI. Because MPI implements waiting for requests using a loop, it is necessary that the global manager thread is assigned to its own CPU core. When the global manager thread receives a request for more packages from one of the local manager threads, it first checks whether there are more packages left. If there are packages available it removes them from its queue and sends their IDs to the requesting local manager. If there are no packages left, the global manager signals the requesting thread that there are no more packages to work on. After all local manager threads have signaled the global manager that they have finished, the global manager terminates all processes.

Local Manager Thread

Every other process than the first has a local manager thread that also maintains a package queue. The local manager thread is responsible for supplying the worker threads with packages of particles to integrate, its flowchart is displayed in figure 3.4. However, unlike the queue of the global manager thread, the queue for the local manager thread is initialized empty. Each local manager waits for one of the worker threads in its process to signal that the queue is running low on packages to work on. This signal-based communication is managed by the scheduler of the operating system (Linux in this case). Therefore, waiting for such a signal causes no significant CPU usage. Consequently, the local manager threads do not need a dedicated CPU core. When a "low on packages"-signal is received, the local manager thread sends an MPI request to the global manager requesting new packages to work on. It then waits until it receives them and adds them to the local queue of the process or, if there are no packages left, it sets a flag implemented using an atomic variable indicating that the worker threads should terminate. The local manager then signals all waiting worker threads to continue. If there are no more packages available it waits for all worker threads to terminate and then messages the global manager that it has finished.

Worker Thread

As the name suggests, the worker threads perform the actual integration of the tracer particles. Because in a process the memory is shared between the threads, the worker threads can also directly access the package queue populated by their respective local manager thread. Additionally, all worker threads share the same gas velocity field in memory which significantly reduces RAM usage. If the number of packages left in the integration queue drops below a specified threshold, the worker thread signals the local manager thread that the queue is running low. If there are no packages left in the queue it waits for a signal from the local manager. The worker thread takes a package from the queue, calculates the initial coordinates of the tracer particles which are part of that package, and starts integrating them one by

one. Integrating them one by one and not simultaneously proved to be significantly faster because of cache locality. Switching between tracer particles during the integration requires loading the current coordinates from memory and different locations in the velocity field have to be accessed. After all tracer particles of a package have been integrated, the calculated recycling time and optionally the trajectory is saved to disk. The worker thread then moves on to the next package.

3.2.4 Results

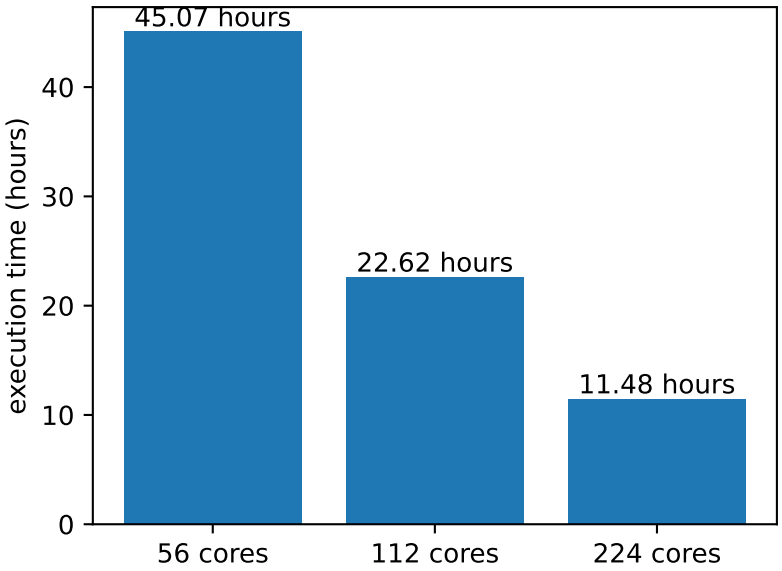

Figure 3.1: Execution time versus the number of used cores for a test set of tracer particles. Doubling the number of cores almost perfectly halves the execution time indicating a low parallelization overhead.

The particle integrator was tested on the "bwForCluster Bioinformatik und Astrophysik Cluster" (BinAC) located in Tübingen. On the standard nodes, BinAC uses two Intel Xeon E5-2630v4 (Broadwell) per node. Each E5-2630v4 consists of two NUMA nodes, i.e each node has a total of four NUMA nodes with 7 cores each. Therefore, for best utilization of the underlying hardware, four processes with 7 threads each were used per node. The

efficient parallelization of the particle integrator allows for a high number of tracer particles and therefore a detailed analysis of the recycling in protoplanetary atmospheres. In the results chapter, figure 5.9 shows the result of a recycling timescale analysis that utilizes 5 nodes on BinAC to integrate more than 500 million tracer particles inside the Hill sphere. Figure 3.1 shows the results of a scaling analysis on 2, 4, and 8 nodes for approximately four million integrated tracer particles on BinAC. The scaling is almost perfectly linear because of the low overhead generated by the distribution of the workload.

3.2.5 Outlook

In addition to using the particle integrator to track the motion of the gas in the protoplanetary atmosphere and measure the recycling time, one could also use it to model the trajectory of massive objects like pebbles. Unlike tracer particles, massive particles would not follow the path of the gas directly but experience a drag force that depends on the properties of the particle. It is therefore necessary to treat the velocity of the particle, $\boldsymbol{v}_{\mathrm{par}}$, as an independent variable. The difference between the velocity of the particle and the gas velocity is the relative velocity, $\boldsymbol{v}_{\mathrm{rel}} = \boldsymbol{v}_{\mathrm{gas}} - \boldsymbol{v}_{\mathrm{par}}$. The single differential equation 3.2 has to be updated to the system of differential equations that includes an evolving particle velocity,

$$\frac{\mathrm{d}\boldsymbol{x}_{\mathrm{par}}}{\mathrm{d}t} = \boldsymbol{v}_{\mathrm{par}} \tag{3.29}$$

$$\frac{\mathrm{d}\boldsymbol{v}_{\mathrm{par}}}{\mathrm{d}t} = \boldsymbol{a}_{\mathrm{drag}} + \boldsymbol{a}_{\mathrm{grav}} + \boldsymbol{a}_{\mathrm{frame}} + \boldsymbol{a}_{\mathrm{tidal}}. \tag{3.30}$$

Here, $\boldsymbol{a}_{\mathrm{drag}}$ is the drag force from the gas, $\boldsymbol{a}_{\mathrm{grav}}$ is the gravitational acceleration because of the protoplanetary core, $\boldsymbol{a}_{\mathrm{frame}}$ is the acceleration because of the rotating frame of reference and $\boldsymbol{a}_{\mathrm{tidal}}$ is the tidal force exerted by the gravity of the host star.

The drag force is calculated differently depending on the properties of the particle, the gas, and their relative velocity. For a relative velocity which is much smaller than the mean thermal velocity of the gas, $\boldsymbol{v}_{\mathrm{th}} =$

$\sqrt{8k_BT/(\pi m_0)}$, and a mean free path λ which is much shorter than the particle radius $r_{\rm par}$, the Epstein drag law applies (Baines et al., 1965). Here, the drag force reads

$$\boldsymbol{F}_{\rm drag,E} = \frac{4\pi}{3} r_{\rm par}^2 \rho_{\rm gas} v_{\rm th} \boldsymbol{v}_{\rm rel}, \tag{3.31}$$

where $\rho_{\rm gas}$ is the density of the gas. However, if the particle radius is much larger than the free mean path $r_{\rm par} \gg \lambda$, the Stokes drag law applies instead (Weidenschilling, 1977). Here, the drag force reads

$$\boldsymbol{F}_{\rm drag,S} = \frac{C_D}{2} \pi r_{\rm par}^2 \rho_{\rm gas} \boldsymbol{v}_{\rm rel}^2 \frac{\boldsymbol{v}_{\rm rel}}{|\boldsymbol{v}_{\rm rel}|}, \tag{3.32}$$

where C_D is a dimensionless drag coefficient which depends on the Reynolds number of the gas and the shape of the particle. For spherical shaped particles its numerical values are given by (Weidenschilling, 1977),

$$C_D \simeq \begin{cases} 24\,{\rm Re}^{-1} & {\rm Re} < 1, \\ 24\,{\rm Re}^{-0.6} & 1 < {\rm Re} < 800, \\ 0.44 & {\rm Re} > 800. \end{cases} \tag{3.33}$$

To obtain a more general drag force one can interpolate between both regimes depending on the given conditions using the coefficient $f = \frac{r_{\rm par}}{r_{\rm par}+\lambda}$ (Supulver and Lin, 2000; Haghighipour and Boss, 2003). After dividing the interpolated drag force with the mass of the particle, $m_{\rm par} = \frac{4}{3}\pi r_{\rm par}^3 \rho_{\rm par}$, one then obtains the drag acceleration,

$$\boldsymbol{a}_{\rm drag} = \frac{(1-f)}{m_{\rm par}} \boldsymbol{F}_{\rm drag,E} + \frac{f}{m_{\rm par}} \boldsymbol{F}_{\rm drag,S} \tag{3.34}$$

$$= \frac{\rho_{\rm gas}}{\rho_{\rm par} \cdot (r_{\rm par} + \lambda)} \left[\frac{\lambda}{r_{\rm par}} v_{\rm th} + \frac{3}{8} C_D |\boldsymbol{v}_{\rm rel}| \right] \boldsymbol{v}_{\rm rel}. \tag{3.35}$$

This drag acceleration can be used to investigate the accretion of solids onto the protoplanetary atmosphere. The results could then be used to construct an even more sophisticated model where the protoplanetary core

continues to grow and the atmosphere is reheated through the influx of solids in addition to the effects of atmospheric recycling.

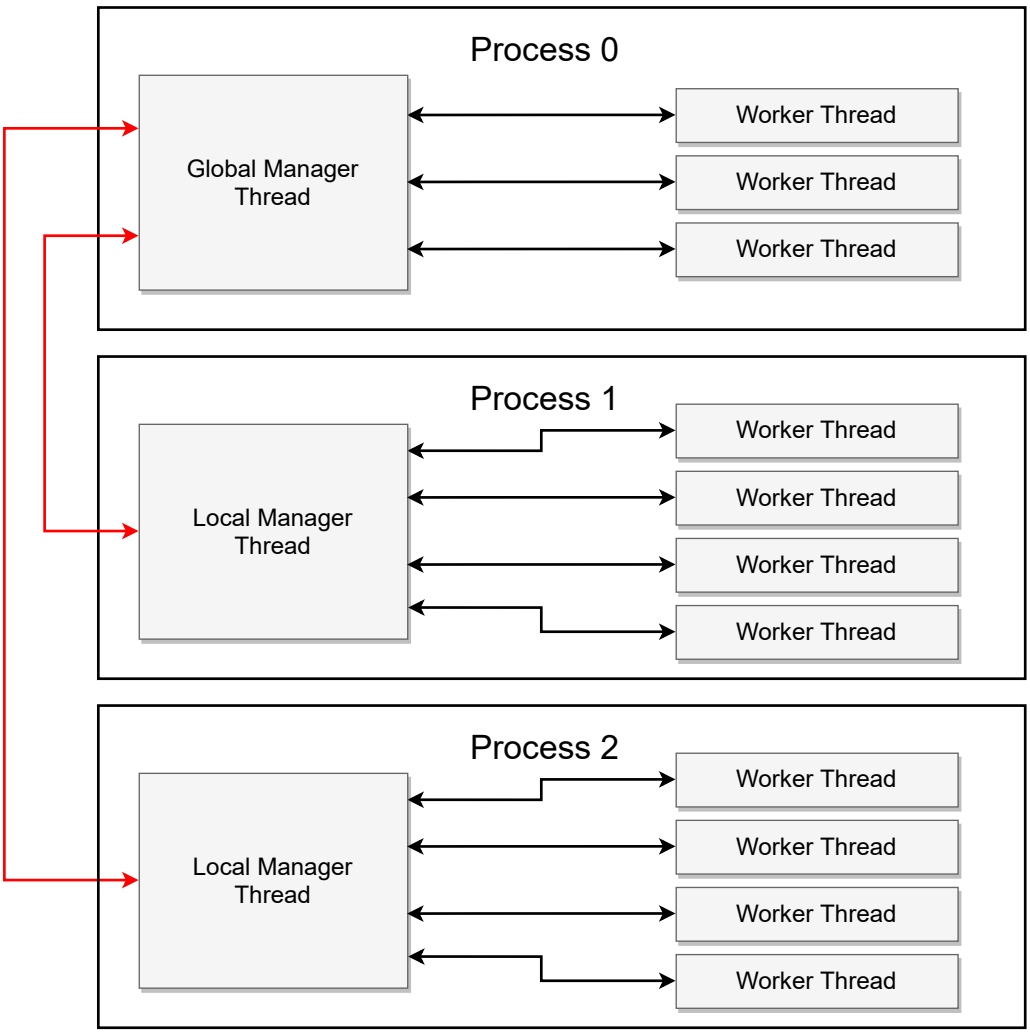

Figure 3.2: Parallelization layout for an example architecture consisting of three non-uniform memory access (NUMA) nodes and 4 cores per NUMA node. The black arrows indicate inter-thread communication and the red arrows indicate inter-process communication using the Message Processing Interface (MPI). The processes can be on the same or different machines. Note that the first process has only three worker threads as the global manager requires a dedicated core to listen for MPI requests from the local manager threads.

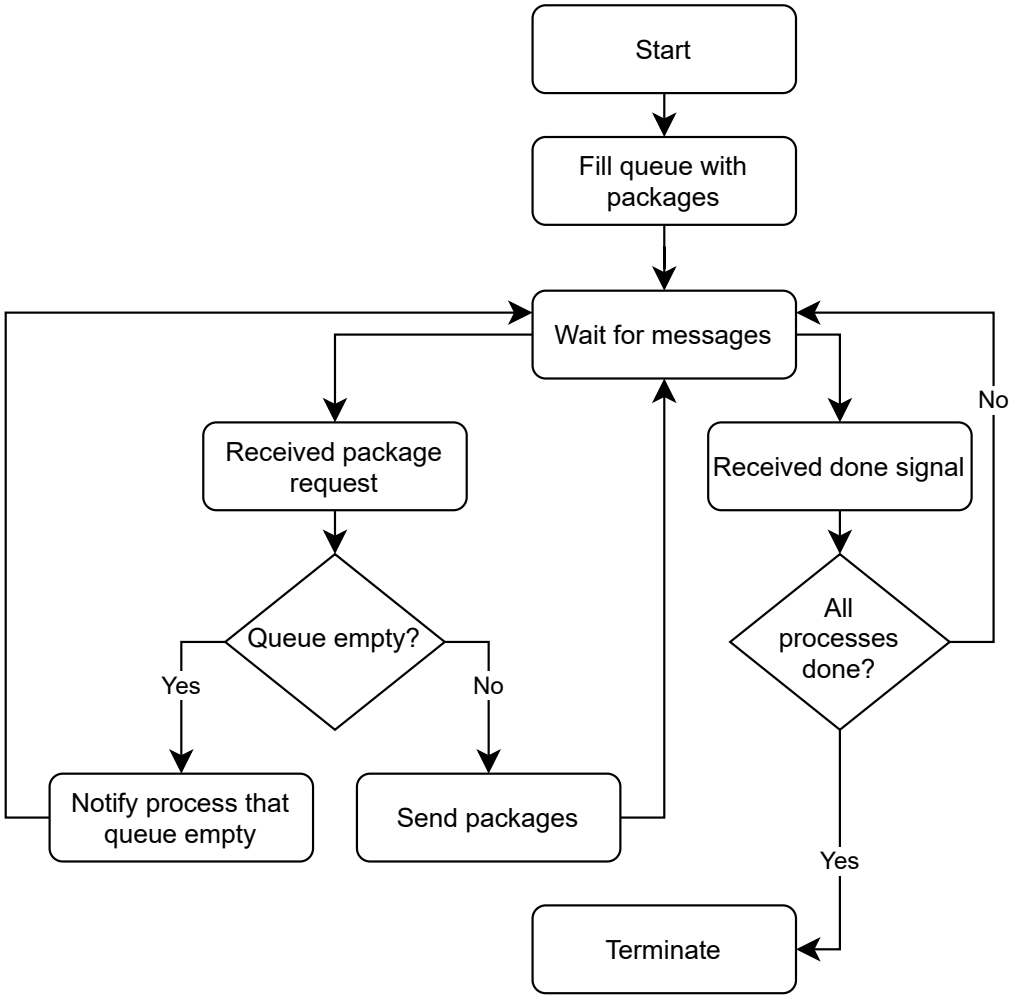

Figure 3.3: Flowchart of the global manager thread. The global manager thread supplies the local manager threads with packages of particles to integrate from its queue. Most of the time is spent waiting for messages using the Message Processing Interface (MPI). This requires a dedicated CPU core.

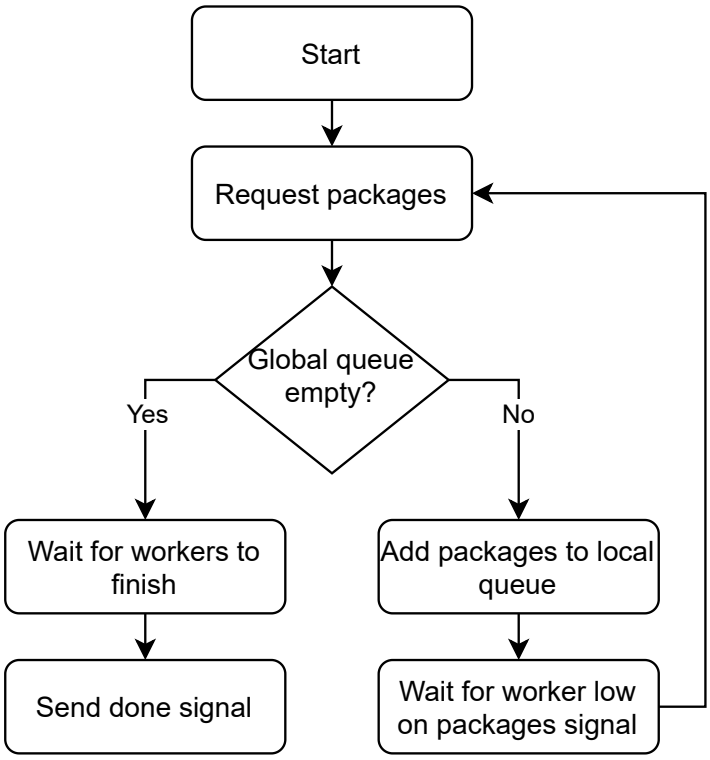

Figure 3.4: Flowchart of the local manager thread. The local manager thread maintains a queue with packages of particles to integrate for the worker threads that are part of its process. It requests new packages from the global manager thread when the queue runs low on packages. Most of the time is spent waiting for the "low on packages signal" from a worker thread. However, because this is implemented using inter-thread communication and handled by the scheduler of the operating systems, this requires almost no CPU time. Therefore, the local manager threads do not need their dedicated CPU core but can share it with a worker thread.

Chapter 4

Publications

The scientific discoveries in the context of this thesis have been published in two articles:

1. Steady state by recycling prevents premature collapse of protoplanetary atmospheres (Moldenhauer et al., 2021)

2. Recycling of the first atmospheres of embedded planets: Dependence on core mass and optical depth (Moldenhauer et al., 2022)

In Moldenhauer et al. (2021) the efficacy of the recycling hypothesis is investigated by comparing the results of 1D and 3D radiation hydrodynamics simulations. I am the lead author of the manuscript. The paper was written in collaboration with PD Dr. Rolf Kuiper, Prof. Dr. Wilhelm Kley and Prof. Dr. Christiaan Ormel. All simulations, their corresponding post-processing, analysis, and creation of figures were conducted by myself. However, regular discussions with PD Dr. Kuiper and Prof. Dr. Kley of preliminary results and their implications have greatly helped me to further improve the results. The introduction was written by Prof. Dr. Ormel, the rest of the manuscript was written by me, taking the co-authors' suggestions into account.

Moldenhauer et al. (2022) continues from the first article and investigates the influence of the headwind, core mass, and optical depth on the recycling process of protoplanetary atmospheres. I am the lead author of the manuscript. The paper was written in collaboration with PD Dr. Rolf

Kuiper, Prof. Dr. Wilhelm Kley and Prof. Dr. Christiaan Ormel. All simulations, their corresponding post-processing, analysis, and creation of figures were conducted by myself. However, regular discussions with PD Dr. Kuiper and Prof. Dr. Kley of preliminary results and their implications have greatly helped me to further improve the results. The manuscript was written by me, taking the co-authors' suggestions into account.

A&A 646, L11 (2021)
https://doi.org/10.1051/0004-6361/202040220

Astronomy & Astrophysics

LETTER TO THE EDITOR

Steady state by recycling prevents premature collapse of protoplanetary atmospheres

T. W. Moldenhauer[1], R. Kuiper[1], W. Kley[1], and C. W. Ormel[2]

[1] Institut für Astronomie und Astrophysik, Universität Tübingen, Auf der Morgenstelle 10, 72076 Tübingen, Germany
e-mail: tobias.moldenhauer@uni-tuebingen.de
[2] Department of Astronomy, Tsinghua University, 30 Shuangqing Rd, Haidian District, Beijing, PR China

Received 23 December 2020 / Accepted 24 January 2021

ABSTRACT

Context. In recent years, space missions such as *Kepler* and TESS have discovered many close-in planets with significant atmospheres consisting of hydrogen and helium: mini-Neptunes. This indicates that these planets formed early in gas-rich disks while avoiding the runaway gas accretion that would otherwise have turned them into hot-Jupiters. A solution is to invoke a long Kelvin-Helmholtz contraction (or cooling) timescale, but it has also been suggested that thermodynamical cooling can be prevented by hydrodynamical planet atmosphere-disk recycling.
Aims. We investigate the efficacy of the recycling hypothesis in preventing the collapse of the atmosphere, check for the existence of a steady state configuration, and determine the final atmospheric mass to core mass ratio.
Methods. We use three-dimensional radiation-hydrodynamic simulations to model the formation of planetary proto-atmospheres. Equations are solved in a local frame centered on the planet.
Results. Ignoring small oscillations that average to zero over time, the simulations converge to a steady state where the velocity field of the gas becomes constant in time. In a steady state, the energy loss by radiative cooling is fully compensated by the recycling of the low entropy gas in the planetary atmosphere with high entropy gas from the circumstellar disk.
Conclusions. For close-in planets, recycling naturally halts the cooling of planetary proto-atmospheres, preventing them from contracting toward the runaway regime and collapsing into gas giants.

Key words. hydrodynamics – protoplanetary disks – planets and satellites: atmospheres – planets and satellites: formation

1. Introduction

Close-in planets are a new exoplanet population that were discovered in abundance by the *Kepler* mission and now also by the Transiting Exoplanet Survey Satellite (TESS). They tend to be small, up to several Earth radii in size, and are located close to their host stars in systems with a fair degree of uniformity (Weiss et al. 2018). Above all, they are very common: one out of three solar-type stars may host these types of planets (Winn & Fabrycky 2015; Zhu et al. 2018). Important to this work, their atmospheres are inferred to harbor significant amounts of hydrogen and helium (Wu & Lithwick 2013), strongly suggesting that they formed early within the primordial disk, hence the name "mini-Neptune". The observed valley in the planet size histogram (Fulton et al. 2017) further suggests that even those planets without an atmosphere were born in the disks, with the smallest and most irradiated of them having their atmospheres stripped over time (Jin & Mordasini 2018).

From a theoretical perspective, there is no consensus on how exactly the atmosphere was accreted. Because these planets orbit so close to their host star, they likely assembled in a very short time (Lee et al. 2014). Even if they did not form in situ but migrated to their present orbital radii, it means that their proto-atmospheres had copious time to contract on the Kelvin-Helmholtz timescale, increasing their atmosphere mass to eventually become self-gravitating and form hot-Jupiters (Batygin et al. 2016). The rapid thermal evolution follows from our expectation that these atmospheres are characterized by a low opacity due to the fact that grains settle quickly (Ormel 2014; Mordasini 2014) and are not replenished by planetesimal infall (Movshovitz et al. 2010). But for mini-Neptunes (and super-Earths), which by far outnumber hot-Jupiters, this runaway gas accretion must have been avoided. Proposed solutions include a high opacity atmosphere (Lee et al. 2014), late formation (Lee & Chiang 2015), atmospheric recycling (Ormel et al. 2015; Ali-Dib et al. 2020), and gap opening (Fung & Lee 2018; Ginzburg & Chiang 2019).

In this Letter, we report that planet atmosphere-disk interaction yields a steady state and results in the complete recycling of the atmosphere. The recycling hypothesis states that atmospheres are not isolated from their disks, which may be inferred (erroneously) from one-dimensional or two-dimensional modeling. Isothermal three-dimensional simulations by Ormel et al. (2015), Fung et al. (2015), and Béthune & Rafikov (2019) instead have shown that disk gas flows deep into the atmosphere and vice versa. However, the flow structure was seen to strongly depend on the thermodynamical properties of the gas, that is, its cooling rate (Kurokawa & Tanigawa 2018; Popovas et al. 2018). Therefore, this problem is best addressed with radiation hydrodynamical (RHD) simulations (Ayliffe & Bate 2009; Cimerman et al. 2017). Here, we present the results of new three-dimensional high resolution RHD simulations of an Earth-mass core embedded

in a disk and demonstrate that the atmosphere reaches an equilibrium. A true steady state is retrieved, in which the atmosphere mass reaches an asymptotic value, because gas elements are transported back to the disk before they have the chance to cool.

2. Model setup

To study the physics of protoplanetary atmospheres, we followed Cimerman et al. (2017) and ran RHD simulations on a three-dimensional grid in spherical coordinates in a local shearing frame centered on the planet. We inserted a planetary core with a mass $M_c = 1\,M_{\rm Earth}$ at a distance $a = 0.1$ au from the star in the protoplanetary disk and followed the formation of an atmosphere around the core. Following Lee et al. (2014), assuming a minimum-mass extrasolar nebula (MMEN, Chiang & Laughlin 2013), we adopted an ambient midplane density of $\rho_0 = 6 \times 10^{-6}\,{\rm g\,cm^{-3}}$ and an ambient temperature of $T_0 = 1000\,{\rm K}$. The initial temperature is constant, and the density is vertically Gaussian. For the rocky core, we took a mean density of $\rho_c = 5\,{\rm g\,cm^{-3}}$. In units of the thermal mass $M_{\rm th} = c_s^3/(G\Omega_{\rm K})$ (Rafikov 2006), the planetary core mass corresponds to a dimensionless mass of $m = M_c/M_{\rm th} = 0.18$. For the time unit, we used the inverse Keplerian orbital frequency of the planet with respect to the star, $\Omega_{\rm K}^{-1} = \sqrt{a^3/(GM_\star)}$.

In our numerical setup, we followed Cimerman et al. (2017) and used the open source PLUTO code (Mignone et al. 2007) and the flux-limited diffusion solver from Kuiper et al. (2010, 2020). Similar to Ormel et al. (2015) and Cimerman et al. (2017), we adopted a spherical grid centered on the planet, but contrary to Cimerman et al. (2017), we simulated the full upper hemisphere around the core, assuming symmetry with respect to the equatorial plane. Previously, we had used the additional symmetry of the local shear and restricted the computational domain to half of the upper hemisphere. However, in this case, gravitational smoothing was necessary to avoid numerical instabilities caused by the boundaries together with the radiative transfer. By simulating the full upper hemisphere in our new setup, the uncorrected Newtonian potential for the gravity of the planetary core can be used throughout, which stabilizes the flow structure of the inner atmosphere. Our new simulations therefore no longer feature these unphysical flow artifacts.

For a steady state to emerge, the simulations have to exceed the Kelvin-Helmholtz timescale. Hence, in order to keep the cooling timescale short and thus save on computation time, we used a low constant opacity of $\kappa = 10^{-4}\,{\rm cm^2\,g^{-1}}$. At that opacity, the protoplanetary atmosphere is still optically thick. For the spherical grid, we used 128 logarithmically spaced grid cells in the radial direction, 32 equidistant cells in the polar direction, and 128 cells in the azimuthal direction. We tested for convergence by comparing the density profile against a simulation with half resolution. In the lower resolution simulation, the density profile differs only slightly in its evolution and settles into the same steady state. As a comparison, and to demonstrate the impact of recycling, we also ran a one-dimensional simulation with otherwise identical parameters and physics.

For the inner boundary at the planetary core, we used a closed boundary condition where all fluxes, including the radiative, vanish (i.e., no energy is exchanged with the planetary core). At the outer boundary, the hydrodynamical quantities were kept constant at their initial values to account for a circumstellar disk that evolves on much longer timescales. The coordinate system is oriented in such a way that the vertical, $\theta = 0$, axis points in the direction of the disk's angular momentum vector. In a local Cartesian system, this corresponds to the z-axis, where the x-axis points to the radial direction (away from the star) and the y-axis in the direction of the disk's motion.

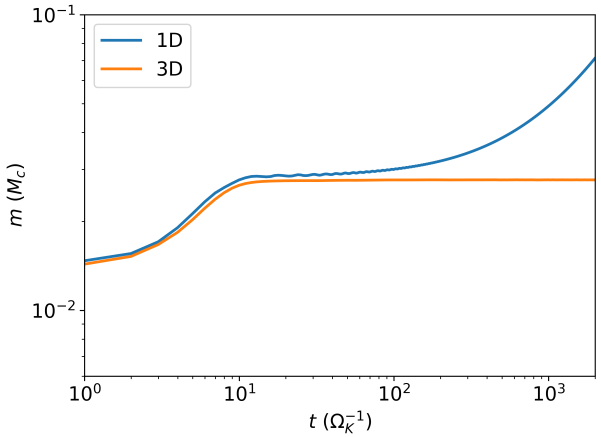

Fig. 1. Mass evolution comparison inside the Hill sphere for the one-dimensional (blue) simulation and the three-dimensional (orange) simulation. The one-dimensional simulation starts with a slightly higher mass than the three-dimensional simulation because it does not account for the vertical stratification of the circumstellar disk. While the one-dimensional simulation continues to accrete, the three-dimensional simulation reaches a steady state, where the final mass, $\chi = M_{\rm final}/M_c = 2.76\%$, is typical for a mini-Neptune planet.

In order to prevent initial shocks at the planetary core surface and allow for a smooth simulation start, we multiplied the planet's gravity by a switch-on factor, $\alpha_{\rm inj}(t) = 1 - \exp(-0.5t^2/t_{\rm inj}^2)$, where $t_{\rm inj} = 4\,\Omega_{\rm K}^{-1}$ is the injection time. For later usage, we defined the Hill radius as $R_{\rm Hill} = a(M_c/(3M_\star))^{1/3}$.

3. Results

We first present the comparison of the three-dimensional simulation to a one-dimensional simulation with identical physical parameters to highlight that a three-dimensional simulation behaves fundamentally differently. In Sect. 3.2, we then demonstrate the steady state found in the three-dimensional simulation by analyzing the entropy evolution and show that the atmosphere eventually stops cooling. In Sect. 3.3, we then show, using tracer particles, that the steady state is indeed maintained by the recycling of the atmospheric gas with gas from the circumstellar disk, in agreement with the recycling hypothesis.

3.1. One-dimensional versus three-dimensional comparison

Figure 1 displays the mass inside the Hill sphere as a function of time since the start of the simulation for the three-dimensional simulation and a one-dimensional simulation with identical parameters. The one-dimensional simulation starts with a slightly higher mass because, unlike the three-dimensional simulation, it does not include the vertical stratification of the circumstellar disk. Initially, during the switch-on time $t_{\rm inj}$, both simulations behave similarly. However, afterward the one-dimensional simulation continues to accrete mass, while the three-dimensional simulation stops accreting. In the three-dimensional simulation, the final ratio of the mass inside the Hill sphere and the core mass, $\chi = M_{\rm final}/M_c$, converges to $\chi = 2.76\%$, a value that is typical for a mini-Neptune planet. In the one-dimensional simulation, gas accretes on a timescale shorter than 1000 years. A mass ratio of $\chi = 100\%$ is reached at

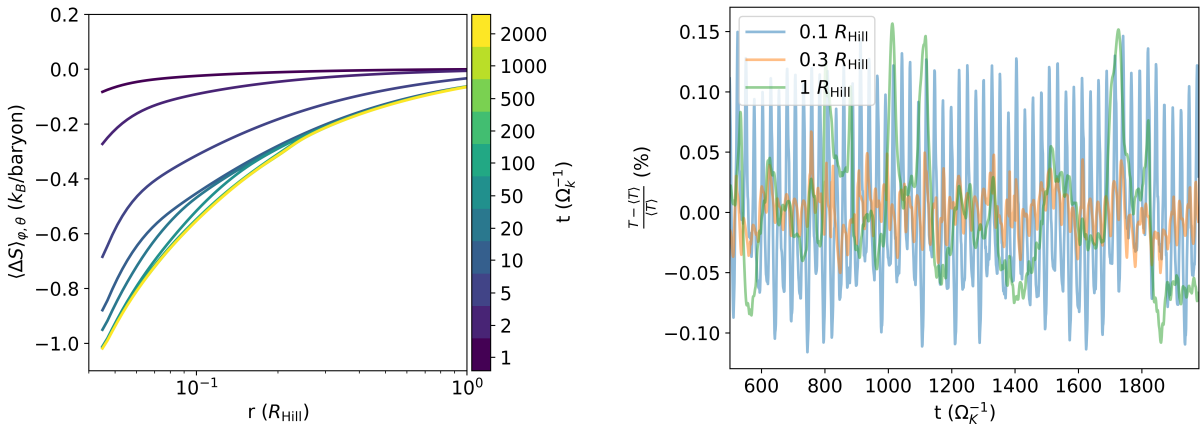

Fig. 2. Thermal evolution of the three-dimensional simulation. *Left*: time evolution of the spherically averaged entropy. The lines are spaced logarithmically in time and the last four lines overlap, indicating the emergence of a radial entropy profile that is constant in time. *Right*: relative temperature deviation to the mean temperature in the steady state at three distances to the protoplanetary core. The trend line slopes of $(-0.84 \pm 4.21) \times 10^{-6}\,\%\,\Omega_{\rm K}$ at $0.1\,R_{\rm Hill}$, $(-4.21 \pm 1.12) \times 10^{-6}\,\%\,\Omega_{\rm K}$ at $0.3\,R_{\rm Hill}$, and $(-2.28 \pm 0.31) \times 10^{-5}\,\%\,\Omega_{\rm K}$ at $1\,R_{\rm Hill}$ are consistent with a true steady state.

$t = 35\,000\,\Omega_{\rm K}^{-1}$, and $\chi = 200\%$ is reached at $t = 65\,000\,\Omega_{\rm K}^{-1}$. This behavior suggests that a pure three-dimensional mechanism is responsible for counteracting the radiative cooling and prevents the atmosphere from contracting.

3.2. Steady state

In Fig. 2, we display the thermal evolution of the three-dimensional simulation. The left panel shows the evolution of the radial entropy profile from the start of the simulation up until the maximum simulation time of $2000\,\Omega_{\rm K}^{-1}$. We show the entropy profile because adiabatic compression and expansion do not change the entropy of the gas, and therefore the entropy is a direct indicator for the cooling of the gas. The entropy profile lines are spaced logarithmically in time. Initially, the entropy drops rapidly because of the radiative cooling. As explained in Sect. 2, the adopted opacity is very low in order to facilitate a cooling timescale shorter than the simulation time. After approximately $200\,\Omega_{\rm K}^{-1}$, the entropy profile stops decreasing and becomes constant in time, ignoring small oscillations. These oscillations are displayed in the right panel of Fig. 2. There we see three distinctive radii, $r \in [0.1, 0.3, 1]\,R_{\rm Hill}$, and compare the temperature to the mean temperature averaged over the steady state ($t > 500\,\Omega_{\rm K}^{-1}$). With a maximum amplitude of 0.15% in temperature and a maximum amplitude of 0.3% in density, these oscillations are very weak and therefore not important for the evolution of the atmosphere. Toward the inner boundary, the oscillations are strongly periodic, in contrast to the outer regions where the oscillations are more irregular. The low frequency of the oscillations, $\sim 0.038\,\Omega_{\rm K}$, is not consistent with the high local Brunt–Väisälä frequency ($\sim 100\,\Omega_{\rm K}$), while the period is comparable to the sound crossing time through the computational domain. Hence, we conclude that they are caused by small global residual perturbations in our inviscid simulation. The statistical trend of these oscillations is consistent with zero. Hence, we can conclude that the three-dimensional simulation is in a true steady state in which the radiative cooling is fully compensated.

3.3. Recycling hypothesis

Energy may only be transported by radiation and advection. Radiation transports energy outward from the hotter inner regions of the atmosphere toward the cooler circumstellar disk. Therefore, advection must counter the radiation energy flux and transport energy back inward to the planetary core. In a steady state, where the net mass flux is zero, adiabatic compression and expansion cancel each other out. Even though the net mass flux over a shell vanishes, this does not imply that the advection energy flux vanishes as well. The energy of the gas that enters the atmosphere is higher than the energy of the gas that leaves the atmosphere, resulting in a net advection energy flux inward. In one dimension, there is only one possible direction for the gas to flow, which makes recycling physically impossible.

To further investigate the recycling of the atmospheric gas, we used tracer particles to measure the time the gas has spent inside the Hill sphere, which we will refer to as the "recycling time". The recycling time was calculated by inserting tracer particles throughout the Hill sphere. In order to remove the small oscillations shown in Fig. 2, we time-averaged the velocity field in the steady state before introducing the tracer particles. We then integrated them backward in time along streamlines and measured the time it takes for them to leave the Hill sphere. This recycling time measures how much time the tracer particle has spent inside the Hill sphere; it quantifies how rapidly atmospheric gas and disk gas are exchanged. Because the trajectory, and thus the measured recycling time, is highly sensitive to the starting location of the particles, we used many more particles than grid cells and took the median of adjacent particles. This approach is justified because the particles represent a continuous fluid. Figure 3 displays two-dimensional cuts of this recycling time. As expected, the recycling time is significantly higher in the inner part of the Hill sphere, where the gas rotates around the protoplanetary core, than in the outer regions where it flows past the planet. Most importantly, however, almost the whole atmosphere recycles in a finite time frame. Even the region directly at the surface of the planetary core is recycled. Only a small region at the boundary of the vertical influx and the outflow in the midplane, the yellow ring in Fig. 3, did not recycle even after $10^4\,\Omega_{\rm K}^{-1}$. However, this small remaining part is negligible for the thermodynamic structure of the atmosphere. Therefore, the gas that forms the planetary atmosphere is eventually replenished with fresh, high entropy gas from the circumstellar disk.

In addition to the recycling time, the figure also displays the density distribution using iso-density lines. The density at the inner boundary reaches a maximum value of $\rho_{\rm max} = 117\,\rho_0$. We can see that both the long recycling time region and the high

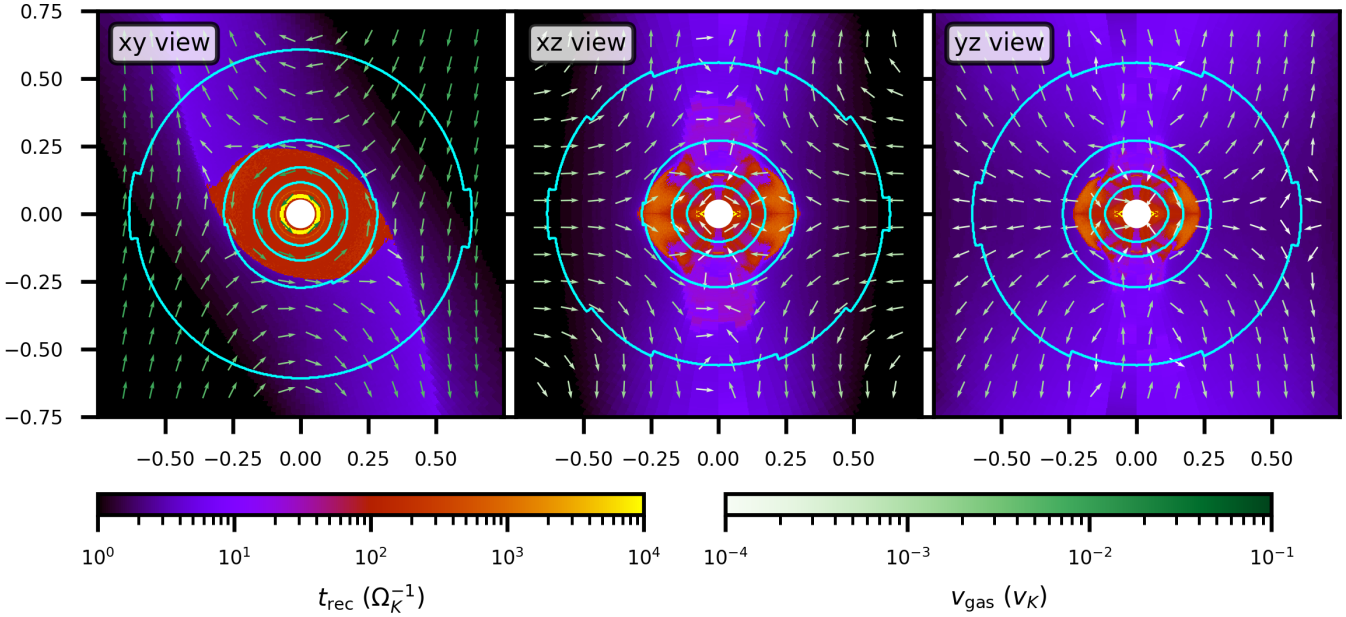

Fig. 3. Recycling time and density of the gas inside the Hill sphere. The length unit is $R_{\rm Hill}$. The velocity of the gas is measured in units of the Keplerian orbital velocity of the planet around the star. The recycling time is defined as the time the gas has already spent inside the Hill sphere. The arrows indicate the velocity of the gas. The density contour lines (cyan) are drawn at [2, 4, 8, 16] ρ_0. These lines are jagged because of the resolution of the grid. *Left*: *xy* plane or midplane. *Middle*: *xz* plane. *Right*: *yz* plane. The atmosphere is recycled up to the surface of the protoplanetary core. Gas around the *z*-axis has a lower recycling time than the gas in the midplane. This indicates that gas enters from the poles and leaves the atmosphere through the midplane.

density region are squished vertically and along the orbital direction. However, the long recycling time region is also elongated along the *x*-direction because of the stellar tidal forces. Close to the vertical axis, the recycling time is also significantly shorter than in the midplane. This shows that fresh gas enters the atmosphere through the poles and leaves the atmosphere by spiraling outward in the midplane before it gets picked up by the shearing flow.

Figure 4 shows the mass-weighted recycling time (i.e., the recycled mass) and compares it to the total mass inside the Hill sphere. Eventually, over 99.85% of the mass inside the Hill sphere is recycled with fresh gas from the circumstellar disk. The remaining part is heated radiatively by the surrounding gas and therefore does not continue to cool either. This illustrates that the radiative cooling is fully compensated by the recycling of the atmospheric gas with fresh gas from the circumstellar disk.

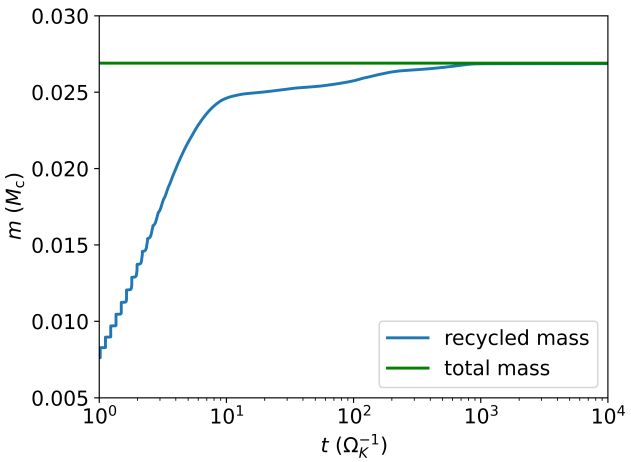

Fig. 4. Recycled mass in the Hill sphere as a function of time after a steady state has emerged. Most mass in the Hill sphere is part of the shearing flow and is therefore recycled very quickly ($\approx 10\,\Omega_{\rm K}^{-1}$). For the inner parts of the atmosphere to be recycled, it takes approximately $10^3\,\Omega_{\rm K}^{-1}$. A small part of the atmosphere is not recycled even after our maximum integration time of $10^4\,\Omega_{\rm K}^{-1}$.

4. Discussion and summary

It has been customary to model planets' thermal evolution like stars, using the one-dimensional stellar structure equations. But young planets, embedded in their natal disks, cannot be regarded as isolated from their environment. Facing the disk gas flow, planets need to "process" material at a rate of $R_{\rm Hill}^3\,\Omega_{\rm K}\rho_0$ – equivalent to ∼1 Earth mass per year (!) – for the parameters used in this study. This number, although crude and not accounting for the spatial variations in the recycling efficiency, in itself underscores the fact that embedded planets cannot be treated as one-dimensional isolated objects. In this Letter, with improved three-dimensional RHD simulations, we have shown that the entire envelope is affected by the vigorous recycling, preventing the adiabatically heated gas from cooling radiatively. We found this despite our choice of very low opacity, for which the one-dimensional setup would enter runaway gas accretion in a mere 10^3 yr. In a future work, we will investigate the dependence of our result on parameters such as the planet mass, location, and disk headwind. In particular, for typical disk parameters with increasing orbital radii, the impact rate of disk gas ($\sim R_{\rm Hill}^3\,\Omega_{\rm K}\rho_0$) decreases, while the gravitational potential at the planet surfaces steepens ($\sim R_{\rm Hill}/R$). Therefore, we can expect recycling to become less vigorous in the outer disk. Nonetheless, the ubiquity of super-Earths and mini-Neptunes close to their host star is most naturally explained by the recycling mechanism. Gas hydrodynamics trumps radiative cooling.

Acknowledgements. TWM and RK acknowledge funding through the German Research Foundation (DFG) under grant no. KU 2849/6-1 as well as support through travel grants under the SPP 1992: Exoplanet Diversity program. RK acknowledges financial support via the Emmy Noether Research Group on Accretion Flows and Feedback in Realistic Models of Massive Star Formation funded by the DFG under grant no. KU 2849/3-1 and KU 2849/3-2. We acknowledge support by the High Performance and Cloud Computing Group at the Zentrum für Datenverarbeitung of the University of Tübingen, the state of Baden-Württemberg through bwHPC and the DFG through grant no. INST 37/935-1 FUGG.

References

Ali-Dib, M., Cumming, A., & Lin, D. N. C. 2020, MNRAS, 494, 2440
Ayliffe, B. A., & Bate, M. R. 2009, MNRAS, 393, 49
Batygin, K., Bodenheimer, P. H., & Laughlin, G. P. 2016, ApJ, 829, 114
Béthune, W., & Rafikov, R. R. 2019, MNRAS, 488, 2365
Chiang, E., & Laughlin, G. 2013, MNRAS, 431, 3444
Cimerman, N. P., Kuiper, R., & Ormel, C. W. 2017, MNRAS, 471, 4662
Fulton, B. J., Petigura, E. A., Howard, A. W., et al. 2017, AJ, 154, 109
Fung, J., & Lee, E. J. 2018, ApJ, 859, 126
Fung, J., Artymowicz, P., & Wu, Y. 2015, ApJ, 811, 101
Ginzburg, S., & Chiang, E. 2019, MNRAS, 487, 681
Jin, S., & Mordasini, C. 2018, ApJ, 853, 163
Kuiper, R., Klahr, H., Dullemond, C., Kley, W., & Henning, T. 2010, A&A, 511, A81
Kuiper, R., Yorke, H. W., & Mignone, A. 2020, ApJS, 250, 13
Kurokawa, H., & Tanigawa, T. 2018, MNRAS, 479, 635
Lee, E. J., & Chiang, E. 2015, ApJ, 811, 41
Lee, E. J., Chiang, E., & Ormel, C. W. 2014, ApJ, 797, 95
Mignone, A., Bodo, G., Massaglia, S., et al. 2007, ApJS, 170, 228
Mordasini, C. 2014, A&A, 572, A118
Movshovitz, N., Bodenheimer, P., Podolak, M., & Lissauer, J. J. 2010, Icarus, 209, 616
Ormel, C. W. 2014, ApJ, 789, L18
Ormel, C. W., Shi, J.-M., & Kuiper, R. 2015, MNRAS, 447, 3512
Popovas, A., Nordlund, Å., Ramsey, J. P., & Ormel, C. W. 2018, MNRAS, 479, 5136
Rafikov, R. R. 2006, ApJ, 648, 666
Weiss, L. M., Marcy, G. W., Petigura, E. A., et al. 2018, AJ, 155, 48
Winn, J. N., & Fabrycky, D. C. 2015, ARA&A, 53, 409
Wu, Y., & Lithwick, Y. 2013, ApJ, 772, 74
Zhu, W., Petrovich, C., Wu, Y., Dong, S., & Xie, J. 2018, ApJ, 860, 101

Astronomy & Astrophysics manuscript no. output
February 26, 2022

Recycling of the first atmospheres of embedded planets: Dependence on core mass and optical depth

T. W. Moldenhauer[1], R. Kuiper[2,1], W. Kley[1,⋆], and C. W. Ormel[3]

[1] Institut für Astronomie und Astrophysik, Universität Tübingen, Auf der Morgenstelle 10, 72076 Tübingen, Germany
[2] Zentrum für Astronomie der Universität Heidelberg, Institut für Theoretische Astrophysik, Albert-Ueberle-Straße 2, 69120 Heidelberg, Germany
[3] Department of Astronomy, Tsinghua University, 30 Shuangqing Rd, 100080 Haidian District, Beijing, China

e-mail: tobias.moldenhauer@uni-tuebingen.de

Received August 1, 2021; accepted February 7, 2022

ABSTRACT

Context. Recent observations found close-in planets with significant atmospheres of hydrogen and helium in great abundance. These are the so-called super-Earths and mini-Neptunes. Their atmospheric composition suggests that they formed early during the gas-rich phase of the circumstellar disk and were able to avoid becoming hot Jupiters. As a possible explanation, recent studies explored the recycling hypothesis and showed that atmosphere-disk recycling is able to fully compensate for radiative cooling and thereby halt Kelvin-Helmholtz contraction to prevent runaway gas accretion.
Aims. To understand the parameters that determine the efficiency of atmospheric recycling, we extend our earlier studies by exploring the effects of the core mass, the effect of circumstellar gas on sub-Keplerian orbits (headwind), and the optical depth of the surrounding gas on the recycling timescale. Additionally, we analyze their effects on the size and mass of the forming atmosphere.
Methods. We used three-dimensional (3D) radiation-hydrodynamic simulations to model a local shearing box centered on the planet. Our planet is located at a separation of $a_p = 0.1$ au from its solar-type host star, and we scanned the core mass range from 1 to $10\,M_{\rm Earth}$. In order to measure and track the recycling of the atmosphere, we employed tracer particles as well as tracer fluids after thermodynamic equilibrium was reached.
Results. For the explored parameter space, all simulations eventually reach an equilibrium where heating due to hydrodynamic recycling fully compensates radiative cooling. In this equilibrium, the atmosphere-to-core mass ratio stays well below 10 %, preventing the atmosphere from becoming self-gravitating and entering runaway gas accretion. Higher core masses cause the atmosphere to become turbulent, which further enhances recycling. Compared to the core mass, the effect of the headwind on the recycling timescale is negligible. The opacity has no significant effect on the recycling timescale, which demonstrates that the Kelvin-Helmholtz contraction timescale and the atmosphere-disk recycling timescale are independent of each other.
Conclusions. Even for our highest core mass of $10\,M_{\rm Earth}$, atmosphere-disk recycling is efficient enough to fully compensate for radiative cooling and prevent the atmosphere from becoming self-gravitating. Hence, in-situ formation of hot Jupiters is very unlikely, and migration of gas giants is a key process required to explain their existence. Our findings imply that atmosphere-disk recycling is the most natural explanation for the prevalence of close-in super-Earths and mini-Neptunes.

Key words. hydrodynamics, protoplanetary disks, planets and satellites: atmospheres, planets and satellites: formation, radiative transfer

1. Introduction

Recent observations by the *Kepler* mission and the Transiting Exoplanet Survey Satellite (*TESS*) found close-in super-Earths and mini-Neptunes in great abundance (Weiss et al. 2018). One out of three solar-type stars may host such a planet (Winn & Fabrycky 2015). These planets are small, several Earth radii in size, orbit close to their host stars, with a typical or mean distance of 0.1 au, and have an atmosphere that mainly consists of hydrogen and helium, which points to an early formation (Wu & Lithwick 2013). Because of the short dynamical timescale and higher surface density at such close orbits (Lee et al. 2014), the cores should have formed early enough for these protoplanets to have had enough time to accrete massive enough atmospheres for them to become self-gravitating and enter runaway accretion to become hot Jupiters (Batygin et al. 2016). In order to explain the high abundance of super-Earths and mini-Neptunes, an efficient mechanism to prevent runaway gas accretion is necessary. Multiple solutions have been suggested, including a high-opacity atmosphere (Lee et al. 2014), late formation (Lee & Chiang 2015), atmosphere-disk recycling (Ormel et al. 2015b; Cimerman et al. 2017; Béthune & Rafikov 2019; Ali-Dib et al. 2020; Moldenhauer et al. 2021), and gap opening (Fung & Lee 2018; Ginzburg & Chiang 2019).

In the core-accretion model, giant planets form by accreting gas from the circumstellar disk onto their planetary cores (Perri & Cameron 1974; Mizuno et al. 1978; Pollack et al. 1996). Computationally, the thermal evolution of the atmosphere of these protoplanets is most conveniently calculated in one radial dimension (1D). A quasi-steady state is reached when a luminosity source is present at the inner boundary (the interface between core and envelope), which is traditionally attributed to the accretion of solids. In this approximation, the protoplanetary at-

⋆ deceased

mosphere[1] becomes a function of mass and solid accretion rate, but is independent of time (Rafikov 2006). Nevertheless, more massive protoplanetary cores accrete more nebular gas. Loosely speaking, the point at which gas accretion overtakes solid accretion, the so-called crossover point, marks the onset of runaway gas accretion (Bodenheimer & Pollack 1986; Pollack et al. 1996; Papaloizou & Terquem 1999). Previous 1D models calculated a critical core mass of $M_{\rm crit} \sim 5{-}20\,M_{\rm Earth}$ as a requirement for the occurrence of runaway gas accretion (Mizuno 1980; Ikoma et al. 2000).

The situation changes when solid accretion terminates and the core mass is fixed. The atmosphere then provides its own luminosity by Kelvin-Helmholtz contraction. For close-in super-Earths and mini-Neptunes, this situation can be expected because any local source of solids (planetesimals) will be accreted on timescales much shorter than the disk lifetime. In addition, for higher-mass protoplanetary cores ($M_c \sim 20\,M_{\rm Earth}$), pebble accretion may also be halted once the pebble isolation mass is reached (Lambrechts et al. 2014; Ataiee et al. 2018; Bitsch et al. 2018). Detailed 1D studies have consistently found that the Kelvin-Helmholtz timescale is a strong function of the opacity in the outer radiative zone (Ikoma et al. 2000; Lee et al. 2014; Hori & Ikoma 2010; Chachan et al. 2021). It has been typical to assume interstellar medium (ISM)-like dust-to-gas ratios and grain properties, in which case the opacity is overwhelmingly determined by the dust, particularly in the outer disk. However, grains are expected to aggregate and settle, giving rise to the conclusion that envelopes should be modeled as grain-free (Mordasini (2014); Ormel (2014)). In this situation, the timescale on wich runaway gas accretion is to be achieved drops below 1 Myr for core masses that exceed $2\,M_\oplus$ (Hori & Ikoma 2010).

Despite these concerns, 1D models are still widely employed to explain the preponderance of super-Earths and mini-Neptunes (Ida & Lin 2004; Mordasini et al. 2009; Schlecker et al. 2021), simply assuming a sufficiently high opacity and a long period in which solids are accreted, or by invoking planetary migration. These 1D models have already demonstrated that the opacity and heating through accretion of solids are important parameters for the evolution of protoplanetary atmospheres. However, a comparison of ALMA observations to current gas accretion models suggested that gas accretion needs to be suppressed by at least one order of magnitude to match the observed planet population (Nayakshin et al. 2019). Some studies have argued that a supersolar metallicity of the gas (Lee et al. 2014) or convective overshooting (Ali-Dib et al. 2020; Johansen & Nordlund 2020) might slow down or halt the Kelvin-Helmholtz contraction. A more straightforward answer may come from hydrodynamics, however. In the past decade, a series of hydrodynamical simulations have indicated that the 1D assumption of an atmosphere isolated from its surroundings is no longer applicable in 3D (Ormel et al. 2015b; Fung et al. 2015; Cimerman et al. 2017; Kurokawa & Tanigawa 2018; Kuwahara & Kurokawa 2020).

However, for geometric reasons, 1D (and 2D) models fail to capture the 3D flow structure, which enables recycling of low-entropy atmospheric gas with high-entropy circumstellar gas. This makes capturing recycling effects computationally expensive, which generally means that these effects are ignored. In the 3D picture, circumstellar gas is accreted through the vertical direction and can be removed in the midplane (Machida et al. 2008; Tanigawa et al. 2012; Szulágyi et al. 2016), and 3D studies found that there is no clear boundary between the atmospheric and circumstellar gas flow and gas is constantly exchanged between both regions, it is recycled. High-entropy circumstellar gas replaces low-entropy atmospheric gas and thereby heats the cooling atmosphere, providing an effective heat source that counteracts radiative cooling (Ormel et al. 2015b; Cimerman et al. 2017). In recent work, we have shown that this hydrodynamic heating effect allows reaching a true steady state (Moldenhauer et al. 2021). Consequently, for close-in planetary cores, there is no atmosphere in the traditional sense of gravitationally bound gas. Therefore, we introduce another definition for the planetary atmosphere that is based on the recycling time, which is the time it takes gas to flow back from the vicinity of the core to the circumstellar disk. Gas that has a significantly longer recycling time than its surroundings, that is, the gas that orbits the core instead of the star for several orbital periods until it is replenished, is defined as the atmosphere (see section 2.2 for details).

To test the efficacy of the recycling hypothesis, we employ a gas opacity in our simulations that is several orders of magnitude lower than a realistic opacity (Ferguson et al. 2005). By choosing an artificially low opacity, we focus our analysis on the recycling mechanism. A 1D simulation with the same parameters would reach $M_{\rm atm} \sim M_c$ in fewer than 10,000 orbits (Moldenhauer et al. 2021). Additionally, a convenient side effect of the shorter cooling timescale is that it saves computational resources by enabling the simulations to reach equilibrium faster. By deliberately using a very low opacity (and no accretion luminosity), Moldenhauer et al. (2021) showed that recycling on its own is capable of fully compensating for radiative cooling and keeping the atmosphere of an Earth-mass planet at $a_p = 0.1$ au in thermodynamic equilibrium. In this paper, we continue this work by investigation the effects of the protoplanetary core mass on the recycling timescale.

In addition to the core mass, another important parameter is the so-called headwind. The disk headwind is defined as the amount by which the gas rotational velocity deviates from Keplerian. Because of the radial pressure gradient in the circumstellar disk, the gas is partially pressure supported. This pressure support acts against the stellar gravity, causing the gas to rotate around the star at sub-Keplerian speeds. As the gas rotates at a lower velocity than the planet, the planet effectively experiences a headwind. The headwind strongly affects the boundary region between the planetary atmosphere and the circumstellar disk, potentially altering the recycling process. A stronger headwind leads to a more asymmetric flow pattern and an overall smaller atmosphere (Ormel 2013).

We continue from Moldenhauer et al. (2021) and use local radiation-hydrodynamic (RHD) simulations to perform a parameter study and investigate the influence of the core mass, the opacity, and the headwind on the recycling process. Our study focuses on close-in super-Earths and mini-Neptunes. Simulations at larger separations require significantly more computational resources because the dynamical timescale is longer than the computational time step, which is limited by the inner boundary. All our simulations use the surface of the solid protoplanetary core as its inner boundary, which is independent of the separation. We reserve this parameter for a future study. Here, we show that for the explored parameter range, all simulations eventually reach thermodynamic equilibrium where radiative cooling is fully compensated for by hydrodynamic recycling. In this thermodynamic equilibrium, atmospheric growth halts completely. Additionally, we study the effects that the analyzed parameters have on the recycling timescale, and we study how the structure and mass of the resulting atmosphere is changed.

[1] We use the words envelope and atmosphere interchangeably.

Name	M_c / $M_\oplus$	$\mathcal{M}_{hw}$	κ / cm^2 g^{-1}	t_{inj}/Ω_K^{-1}	M_H/M_c	M_B/M_c	M_{atm}/M_c	$R_H/R_\oplus$	$R_B/R_\oplus$	$R_{atm}/R_\oplus$
M1	1	0	10^{-4}	4	2.70 %	1.37 %	0.20 %	23.5	17.3	6.0
M2	2	0	10^{-4}	4	3.52 %	5.10 %	0.42 %	29.6	35.4	8.2
M5	5	0	10^{-4}	4	5.05 %	21.38 %	1.32 %	40.1	98.9	14.7
M10	10	0	10^{-4}	4	4.43 %	40.85 %	1.91 %	50.6	212.7	24.6
M1-HW	1	0.1	10^{-4}	4	2.71 %	1.37 %	0.14 %	23.5	17.3	4.8
M2-HW	2	0.1	10^{-4}	4	3.52 %	5.10 %	0.37 %	29.6	35.4	7.6
M5-HW	5	0.1	10^{-4}	4	5.02 %	21.21 %	1.04 %	40.1	98.9	11.7
M10-HW	10	0.1	10^{-4}	4	4.37 %	40.71 %	1.87 %	50.6	212.7	24.6
M1-HO	1	0	10^{-3}	4	2.68 %	1.35 %	0.15 %	23.5	17.3	5.3
M1-LO	1	0	10^{-5}	4	2.90 %	1.40 %	0.44 %	23.5	16.5	8.1
M1-SLOW	1	0	10^{-4}	400	2.70 %	1.37 %	0.20 %	23.5	17.3	6.0

Table 1. Simulations and their respective atmospheric mass inside different radii. Bondi and Hill are abbreviated with B and H, respectively. R_{atm} is the radius at which the azimuthal velocity is the strongest component in the midplane, i.e., at which the flow of the circumstellar disk starts and the atmospheric flow ends (see section 2.2). The simulations are labeled MX, where X is the mass of the core in units of M_{earth}. The suffixes describe alterations compared to the standard setup: HW means that a headwind is included, HO and LO stand for a higher and lower opacity, respectively. Finally, M1-SLOW is a simulation with an injection time that is 100 times longer.

2. Model

For our simulations, we built upon the code and parameters used by Cimerman et al. (2017) and Moldenhauer et al. (2021). We used RHD on a 3D spherical grid in a local shearing box approach, centered on the planet. Figure 1 outlines the structure of the setup. The separation of the planet from its host star is $a_p = 0.1$ au, and we adopt a corresponding ambient midplane density of $\rho_0 = 6 \cdot 10^{-6}$ g cm^{-3} and temperature of $T_0 = 1000$ K following Lee et al. (2014), in accordance with the minimum-mass extrasolar nebula (MMEN; Chiang & Laughlin 2013). In the optically thick regime, Cimerman et al. (2017) showed that the final mass of the atmosphere is rather independent of opacity or total optical depth. For the parameter scan, we therefore used a single value of opacity, $\kappa = 10^{-4}$ cm^2 g^{-1}, in order to keep the cooling timescale short and thus save on computation time; however, in section 5.3 we compare different opacities to explore the effect of optical depth. The simulation domain covers the upper hemisphere, and we did not use any smoothing for the gravitational potential of the planet as we resolve the rocky planetary surface. To explore the effect of the core mass on the flow structure as well as the atmospheric mass, we performed simulations with core masses $M_c \in [1, 2, 5, 10]\, M_{Earth}$. For the rocky cores, we assumed a mean density of $\rho_c = 5$ g cm^{-3}. Models are labeled MX, where X is the core mass in units of Earth masses. The M1 simulation is identical to the setup described in Moldenhauer et al. (2021). All simulations are listed in Table 1.

2.1. Headwind

Because of the radial thermal pressure gradient through the circumstellar disk, the gas experiences an outward force, $\boldsymbol{F}_p = -\nabla p$, that acts against the stellar gravity. This results in a sub-Keplerian rotation of the gas. For solid bodies such as planets, on the other hand, this force is negligible. The planet therefore moves faster than the surrounding gas and thus experiences a headwind along its orbital direction. As we did not model the full circumstellar disk, we artificially added this headwind to our shearing box setup. In a global simulation, this effect would be naturally included. We parameterized the headwind in our simulations in terms of the Mach number, $\mathcal{M}_{hw}$, where

$$v_{hw} = \mathcal{M}_{hw} \cdot c_{iso} \tag{1}$$

is the gas velocity of the headwind and c_{iso} is the isothermal sound speed for the initial and boundary temperature, T_0. From the temperature profile we used for our simulations, we can calculate the headwind Mach number as

$$\mathcal{M}_{hw} = 0.033 \left(\frac{a}{0.1\text{au}}\right)^{2/7}. \tag{2}$$

For the minimum-mass solar nebula (MMSN), we obtain a slightly lower headwind Mach number (Kuwahara & Kurokawa 2020),

$$\mathcal{M}_{hw} = 0.028 \left(\frac{a}{0.1\text{au}}\right)^{1/4}. \tag{3}$$

However, to clearly assess the effects of the headwind and show its impact clearly, we followed Ormel et al. (2015b) and chose a headwind Mach number of $\mathcal{M}_{hw} = 0.1$. Models that include a headwind are marked by the abbreviation HW in their names.

2.2. Length scales

There are two important length scales in protoplanetary atmospheres. The first is the Hill radius,

$$R_{Hill} := a \sqrt[3]{\frac{M_c}{3M_\star}}, \tag{4}$$

which is the radius of the region in which the planetary gravity dominates the stellar gravity. The second is the Bondi radius,

$$R_{Bondi} := \frac{2GM_c}{c_s^2}, \tag{5}$$

which is the radius at which the escape velocity equals the speed of sound. To calculate the Bondi radius, we used the spherically averaged local sound speed. The Bondi radius is therefore time dependent and a local length scale. The Hill radius, on the other hand, is constant in time and a global length scale. We emphasize that in the 3D setup, physical relevant physical quantities as well as the flow field are continuous across R_{Hill} and R_{Bondi}, but we nevertheless included them for comparison purposes.

For an atmosphere that fully recycles, the traditional definition of an atmosphere as the region in which the gas is gravitationally bound is no longer meaningful. Therefore, in addition to

the Hill and Bondi radii, we defined a third radius $R_{\rm atm}$ to analyze the size and mass of the protoplanetary atmosphere,

$$R_{\rm atm} := \max\left\{ r \,\middle|\, v_\varphi|_{\theta=\pi/2} > \max(v_r, v_\theta) \right\}. \tag{6}$$

$R_{\rm atm}$ is the maximum radius at which the azimuthal velocity component is the largest component of the velocity field in the midplane, that is, where the gas rotates around the core instead of the star. This radius is a good measurement for the size of the atmosphere as it indicates where the circular atmospheric flow transitions into the circumstellar shearing flow. In the following analyses, the 2D cut figures include this radius as a magenta circle. The resulting sphere matches the size of the atmosphere well that is obtained from the regions that are recycled on longer timescales, $t_{\rm rec} > 100\,\Omega_K^{-1}$. Throughout this work, "atmosphere" refers to the region inside $R_{\rm atm}$. At the time of disk dispersal, this region might form a proper bound atmosphere. However, because our simulations do not cover the dispersal of the disk, this remains work for a further investigation.

3. Numerics

3.1. Radiation hydrodynamics

We used the hydrodynamics module of the open-source code PLUTO (Mignone et al. 2007), version 4.1, and the flux-limited diffusion solver described in Kuiper et al. (2010) and Kuiper et al. (2020). PLUTO solves conservation equations: conservation of mass, momentum, and total energy,

$$\frac{\partial \rho}{\partial t} + \nabla \cdot (\rho \boldsymbol{v}) = 0, \tag{7}$$

$$\frac{\partial \rho \boldsymbol{v}}{\partial t} + \nabla(\rho \boldsymbol{v} \cdot \boldsymbol{v} + p) - \rho \boldsymbol{a} = 0, \tag{8}$$

$$\frac{\partial E}{\partial t} + \nabla \cdot \left[(E + p) \cdot \boldsymbol{v}\right] + \nabla \cdot \boldsymbol{F} - \rho \boldsymbol{v} \cdot \boldsymbol{a} = 0. \tag{9}$$

Here, ρ is the gas density, p is the gas pressure, $\boldsymbol{v}$ is the gas velocity, and $E = E_{\rm th} + E_{\rm kin}$ is the total energy of the gas. $\boldsymbol{a}$ represents external accelerations, and $\boldsymbol{F}$ is the radiation flux from the flux-limited diffusion solver.

Because our simulations use the advantages of a shearing box around the planet, which is not an inertial frame of reference, we have to include forces of inertia that act on the gas. First, we include the Coriolis acceleration,

$$\boldsymbol{a}_{\rm cor} = -2\boldsymbol{\Omega}_K \times \boldsymbol{v}, \tag{10}$$

where $\boldsymbol{\Omega}_K = \Omega_K \cdot \boldsymbol{e}_z$ is the Keplerian frequency at the location of the planet pointing in the z-direction. The tidal acceleration is the sum of the stellar gravity, $-GM_\star/a^2$, and the centrifugal acceleration, $\Omega_K^2 a$. Here a is the distance of the gas to the star. Using the Keplerian frequency, $\Omega_K = GM_\star/a_p^3$, at the orbital position of the planet, a_p, the linearized approximation of the tidal acceleration calculates as

$$\boldsymbol{a}_{\rm tid} \approx 3\Omega_K^2 \Delta x \cdot \hat{\boldsymbol{e}}_x, \tag{11}$$

where $\Delta x = a - a_p$ is the relative orbital position of the gas with respect to the planet. Finally, for the simulations that include a headwind, we add an additional acceleration,

$$\boldsymbol{a}_{\rm hw} = 2\mathcal{M}_{\rm hw} c_{\rm iso} \Omega_K \cdot \hat{\boldsymbol{e}}_x, \tag{12}$$

to account for the net effect of the radial thermal pressure gradient. Together with the gravitational acceleration by the planetary core, these accelerations add up to the total external acceleration, $\boldsymbol{a}$, in equation 8 and 9.

In the radial direction, the computational domain extends from the planetary core r_c to $r_{\rm max} = 5H = 5h \cdot a_p$, where $h = c_{\rm iso}/v_K = 0.02$ denotes the aspect ratio and H is the pressure scale height of the circumstellar disk at the location of the planet. In the polar and azimuthal directions, the domain covers the hemisphere above the midplane, and symmetry at the midplane is implied by the boundary conditions. For all simulations, we used a resolution of 128 logarithmically spaced cells in the radial, 32 cells in the polar, and 128 in the azimuthal direction.

Simulations were initialized with the circumstellar disk shear flow and a planar uniform but vertically stratified density,

$$\rho_{t=0}(\boldsymbol{r}) = \rho_0 \cdot \exp\left(-\frac{1}{2}\frac{z^2}{H^2}\right). \tag{13}$$

The radially inner boundary at the planetary core is reflective, and the values at the outer boundary were kept constant at their initial values. For the boundary at the vertical axis, $\theta = 0$, we used the so-called π-boundary (Ormel et al. 2015b). Here, the ghost cells, which have an effective negative θ value, are filled with quantities from $\varphi + \pi$,

$$A(-\theta, \varphi) = A(+\theta, \varphi + \pi). \tag{14}$$

Even though the interface of this boundary actually has an areal extent of zero, the values of the ghost cells have to be specified in the PLUTO code and are used in the reconstruction step of the hydrodynamics solver to compute the slope of grid-cell-centered variables.

To prevent the occurrence of initial shocks at the planetary core surface, we multiplied the planetary gravity and the headwind magnitude with a switch-on factor,

$$\alpha_{\rm inj}(t) = 1 - \exp\left(-\frac{1}{2}\frac{t^2}{t_{\rm inj}^2}\right), \tag{15}$$

where $t_{\rm inj} = 4\,\Omega_K^{-1}$ is the injection time. To confirm that the chosen injection time $t_{\rm inj} = 4\,\Omega_K^{-1}$ does not affect the equilibrium solution of our simulation, we ran an additional simulation M1-SLOW, whose parameters are identical to those of the M1 simulation, but the injection time is much longer, $t_{\rm inj} = 400\,\Omega_K^{-1}$. With this long injection time, the density and thus the temperature of the atmosphere build up more slowly. This might give the atmosphere more time to cool before recycling starts, and it might result in a different equilibrium of cooling and recycling. However, this is not the case, as Table 1 shows. The mass and thermodynamics of the final atmosphere are independent of the chosen injection time. Finally, for simulations including a headwind, we added the headwind velocity, $v_{\rm hw}$, to the shearing velocity at the radially outer boundary.

3.2. Tracer particles

For our simulations with low planetary mass, $M_c = 1\,M_{\rm Earth}$, which eventually enter a steady state, we used tracer particles in postprocessing to determine the time the gas has spent inside the Hill sphere to calculate the recycling timescale. The choice of the Hill sphere to define the recycling timescale is arbitrary. A change in this radius has little effect on the measured recycling time as long as it exceeds the atmosphere. The recycling timescale is an additive quantity and orders of magnitude lower

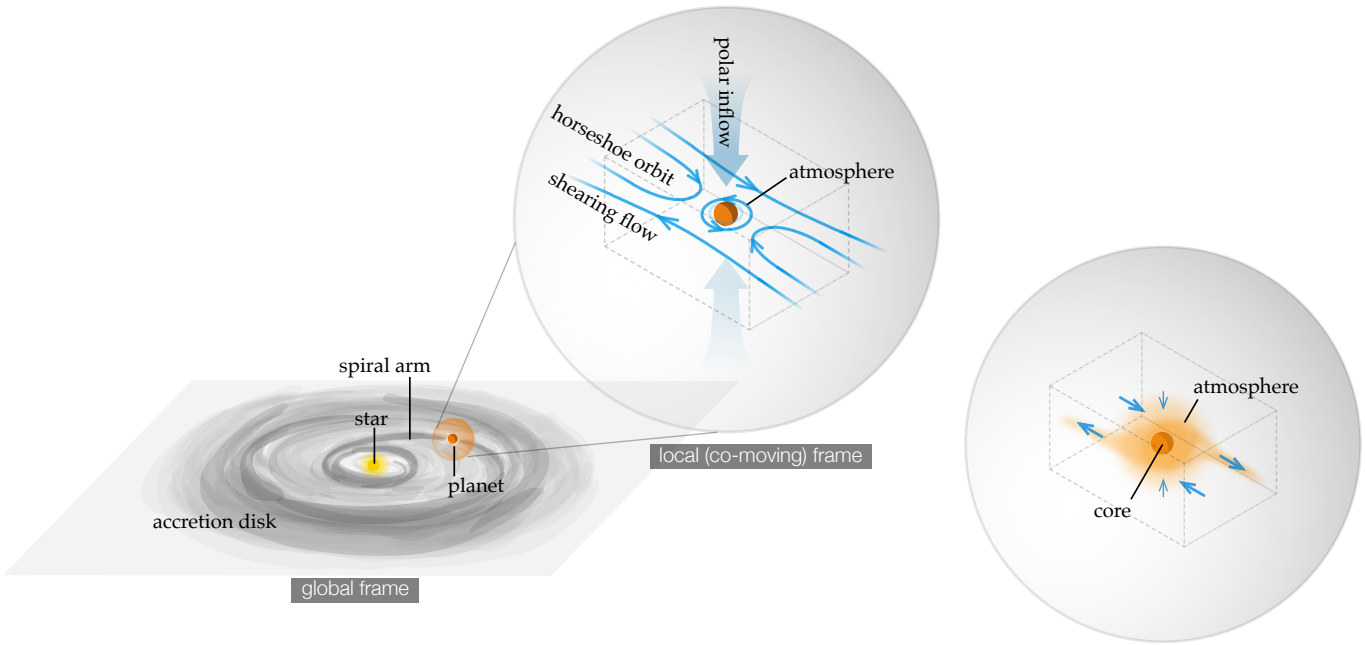

Fig. 1. Outline of the setup. We introduce a rocky core and simulate the protoplanetary atmosphere in a local frame, while we keep the conditions of the circumstellar disk constant in time. The planetary core accumulates gas to form an atmosphere. In addition to polar inflow, the two horseshoe orbits that form along the orbital direction of the planet constantly exchange high-entropy circumstellar with low-entropy atmospheric gas. This process results in thermodynamic equilibrium in which radiative cooling is fully compensated for by atmosphere-disk recycling. We thank André Oliva for drawing this sketch.

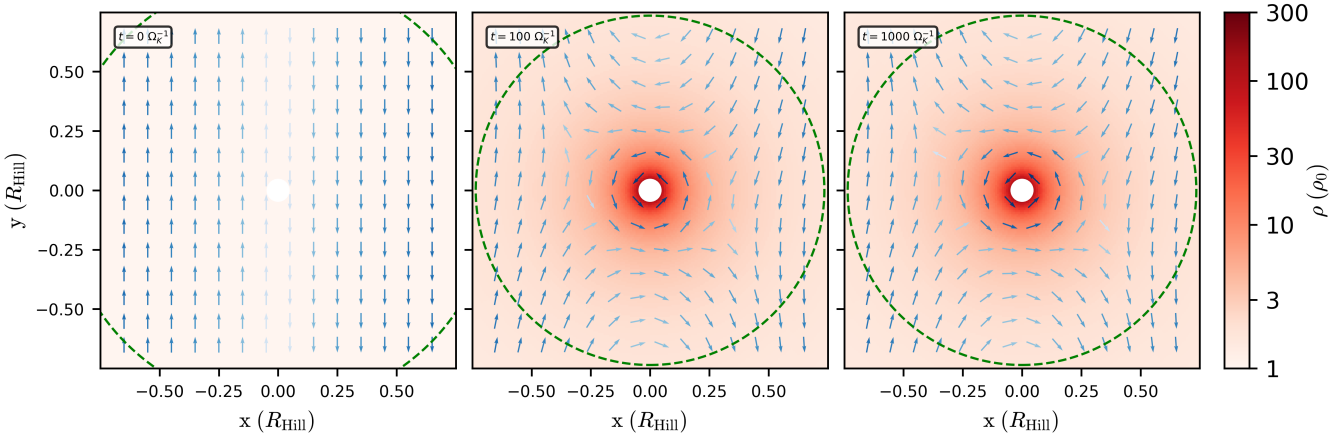

Fig. 2. Development of the flow structure in the midplane for the M1 simulation. The computation domain is initialized with a uniform density and the shear flow of the circumstellar disk. The planetary core accretes gas, and a protoplanetary atmosphere forms around the core. In the orbital direction of the planet, horseshoe orbits form, centered on the sign change of the shear flow. Eventually, the simulation reaches thermodynamic equilibrium, where radiative cooling is fully compensated for by atmosphere-disk recycling. In this equilibrium the gas temperature and the gas density become constant in time. The dashed green circle is the Bondi radius calculated from the local temperature. The Bondi radius shrinks with time because the atmospheric gas heats up when it is compressed. After $\sim 100\,\Omega_K^{-1}$ the simulation reaches thermodynamic equilibrium.

outside of the atmosphere than inside. The Hill sphere was chosen because it is the upper limit at which the planetary core could significantly alter the gas flow. As tracer particles can easily be integrated along streamlines, they are a computationally inexpensive method for calculating the recycling timescale as a function of space.

After the simulations reached a steady state, we took the velocity field of the simulation averaged over the last 500 outputs at an output frequency of $1\,\Omega_K^{-1}$ and integrated tracer particles along streamlines backward in time. This removed any residual random oscillations that might disturb the integration of the tracer particles. We call the time it takes for the tracer particles to escape the Hill sphere the recycling time $t_{\rm rec}$. The recycling time measures the time for which the gas has been in the Hill sphere. Because of the increased pressure caused by the gravity of the planetary core, atmospheric gas is hotter than circumstellar gas. This temperature gradient causes the atmosphere to cool through radiative emission. Therefore, atmospheric gas has a lower entropy than the circumstellar gas. As atmospheric gas is replenished with fresh circumstellar gas through atmospheric recycling, this entropy loss is compensated for. Consequently, a longer recycling timescale, that is, it takes longer for the gas to

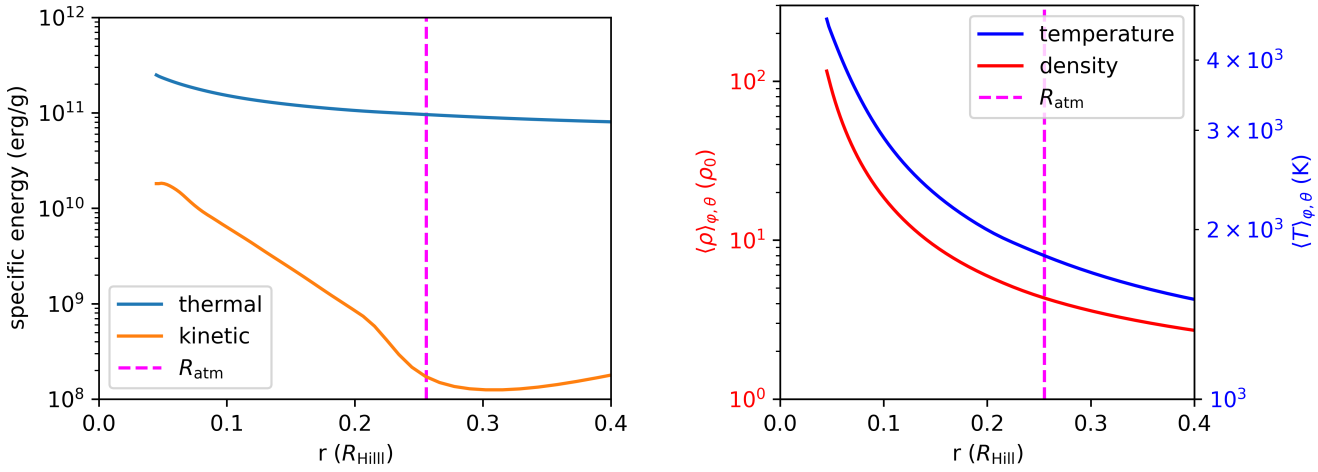

Fig. 3. Radial 1D-averaged profiles for M1 simulation. Left: Thermal and kinetic specific energy profiles. Right: Density and temperature profiles. The dashed magenta vertical line is $R_{\rm atm}$ as defined in Sect. 2.2. The thermal energy is more than one order of magnitude higher than the kinetic energy, i.e., the atmosphere is pressure supported. Inside $R_{\rm atm}$, the kinetic energy is significantly higher than outside. This is because of the azimuthal velocity component: Inside $R_{\rm atm}$, the gas rotates around the core.

be replenished, means that gas in this region has had more time to cool radiatively.

We realized that the recycling time strongly depends on the starting position of the tracer particles. Small spatial variations can cause very different trajectories, such as the number of orbits around the planetary core and thus recycling times. This is illustrated in more detail in section 4.3. In order to determine the physically meaningful mean value, we arranged the tracer particles on a grid and calculated the median of all tracer particles in a grid cell. This is justified because the tracer particles trace a gaseous medium that mixes naturally.

For the integration, we used an adaptive fifth-order Runge-Kutta integrator. The velocity of the tracer particle was calculated from the hydrodynamic velocity field using linear interpolation on a spherical grid.

3.3. Tracer fluid

For our higher core mass simulations, the gas flow structure continued to change even after thermodynamic equilibrium is reached. Therefore, it is no longer possible to measure the recycling timescale in post processing. Instead, the recycling timescale has to be measured while the simulation is still running. While tracer particles could still be used, it is faster and easier to use a tracer fluid instead as the tracer fluid can be advected using the same flux that is calculated for the field of gas mass density. A tracer fluid is a scalar quantity ψ that is evolved using the advection equation

$$\frac{\partial \psi}{\partial t} + \nabla \cdot (\psi \boldsymbol{v}) = 0, \tag{16}$$

where $\boldsymbol{v}$ is the velocity field of the gas. The density distribution of the tracer fluid ψ is independent of the gas density and can be chosen freely. However, the tracer fluid density evolves in exactly the same way as the density of the gas, allowing us to trace the motion of the gas without altering it. For our tracer fluid postprocessing, we evolved the simulation until it reached thermodynamic equilibrium where the temperature of the atmosphere no longer decreases and the density no longer increases. We then inserted a uniform density tracer fluid in the Hill sphere and continued to evolve the simulation. The choice of the region that is initially filled with tracer fluid is arbitrary. We chose the Hill sphere as it serves as an upper estimate of the size of the protoplanetary atmosphere. The tracer fluid density outside of the Hill sphere, that is, in the circumstellar disk, is zero and no additional tracer fluid enters the simulation domain through the outer boundary. The tracer fluid may only leave the simulation domain. After a fixed evolution time, regions that exchange gas with the circumstellar disk on shorter timescales will have a lower concentration of tracer fluid. The local density of the tracer fluid is therefore a measure for the recycling timescale at that location.

4. Atmosphere-disk recycling

First, we revisit the M1 simulation described in Moldenhauer et al. (2021) and analyze it in even greater detail using additional postprocessing techniques to fully understand the recycling process. The same postprocessing is used for the other models to perform the parameter study in the next section. We start by giving an overview of the hydrodynamic quantities in section 4.1. In section 4.2 we explain the thermodynamic equilibrium that all simulations eventually reach and explain the key differences between low and high core mass cases. In section 4.3 we analyze the gas flow in more detail using the trajectories of two sample tracer particles. In section 4.4 we then show the recycling process using a tracer fluid and confirm that the entire atmosphere recycles.

4.1. Overview

Figure 1 outlines the model and the resulting flow structure in a sketch. Even though the simulations were performed in spherical coordinates, we used a Cartesian coordinate system to describe the results in the local frame around the planet. The x- or radial direction points away from the star through the planet, the y- or orbital direction points in the orbital direction of the planet, and the z- or vertical direction is aligned with the angular momentum vector of the circumstellar disk. All three coordinates are centered on the planet. The left panel of figure 3

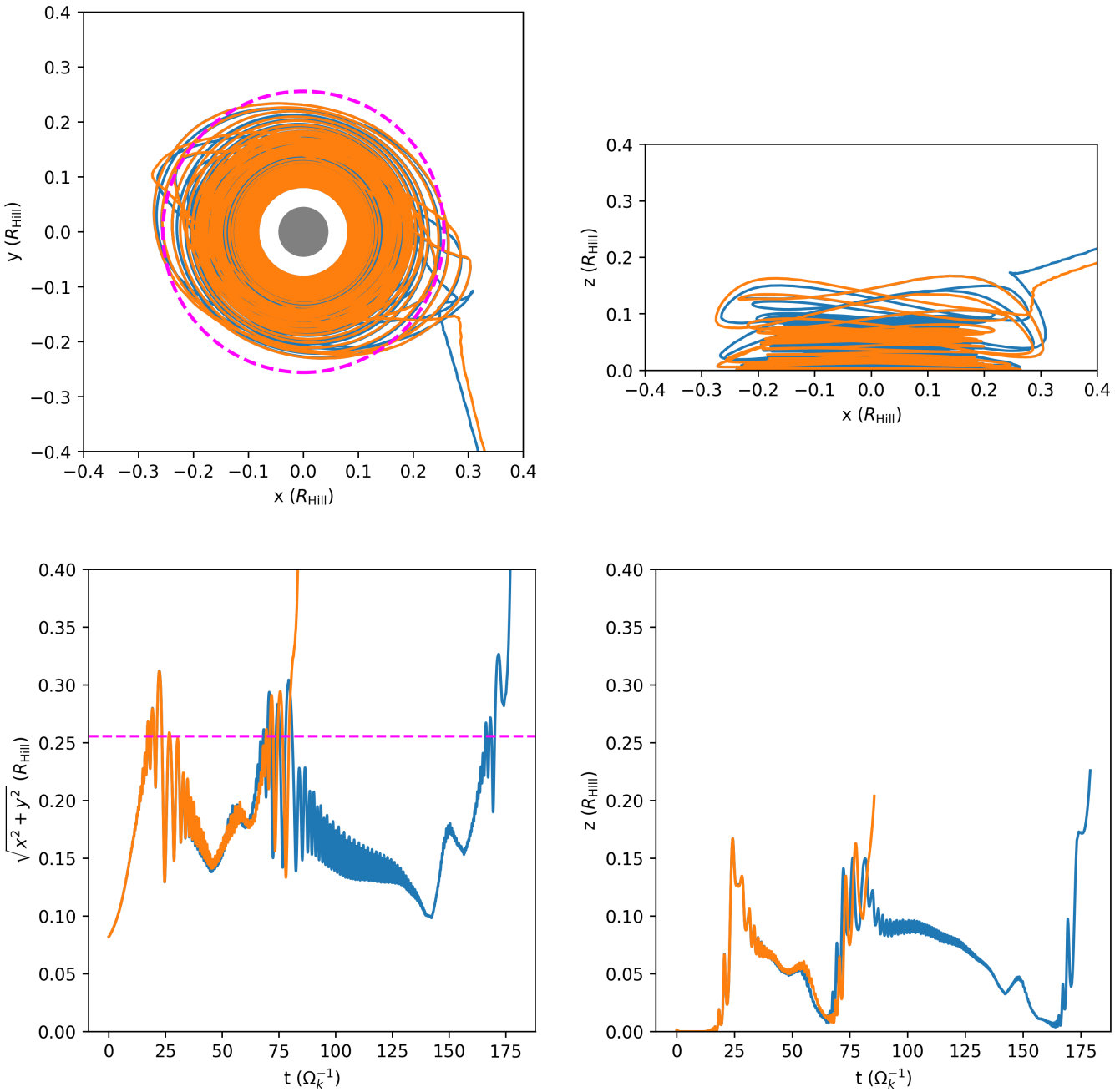

Fig. 4. Trajectories of two tracer particles integrated forward in time inside the Hill sphere. Both particles start in the midplane with the same distance to the protoplanetary core and only slightly different azimuthal angles. The starting location was chosen specifically to show the sensitivity of the path to the initial conditions. The dashed magenta lines are the atmospheric radius $R_{\rm atm}$ as defined in section 2.2. The planetary core has a radius of $R_{\rm core} = 0.044\,R_{\rm Hill}$ and is displayed as a gray circle. The white ring in the top left panel is also recycled, but is not part of the trajectory of the two example tracer particles. Top left: Midplane view. Top right: View of the xz-plane. Bottom left: Distance to the z-axis ($\sqrt{x^2+y^2}$). Bottom right: Distance to the midplane (z-coordinate). Both tracer particles start to spiral outward in the midplane. The tracer particle represented by the orange line escapes the Hill sphere much faster than the particle represented by the blue line, indicating a strong dependence on the initial conditions of the tracer particle.

displays the 1D-averaged energy budget of the M1 simulation. The thermal energy of the atmosphere is several orders of magnitude higher than the kinetic energy. The atmosphere is therefore pressure supported. Inside $R_{\rm atm}$, the kinetic energy density is significantly higher than outside. This energy is primarily in the azimuthal velocity component, that is, it is from the rotation of the gas around the protoplanetary core. The density and temperature profiles displayed in the right panel of figure 3 show a smooth transition from the protoplanetary atmosphere to the circumestellar disk. Only the velocity profile allows us to distinguish between the atmosphere and the disk. Hence our definition of $R_{\rm atm}$ based on dynamical arguments.

To give an overview of the general flow structure, we first display the midplane density distribution and the velocity field

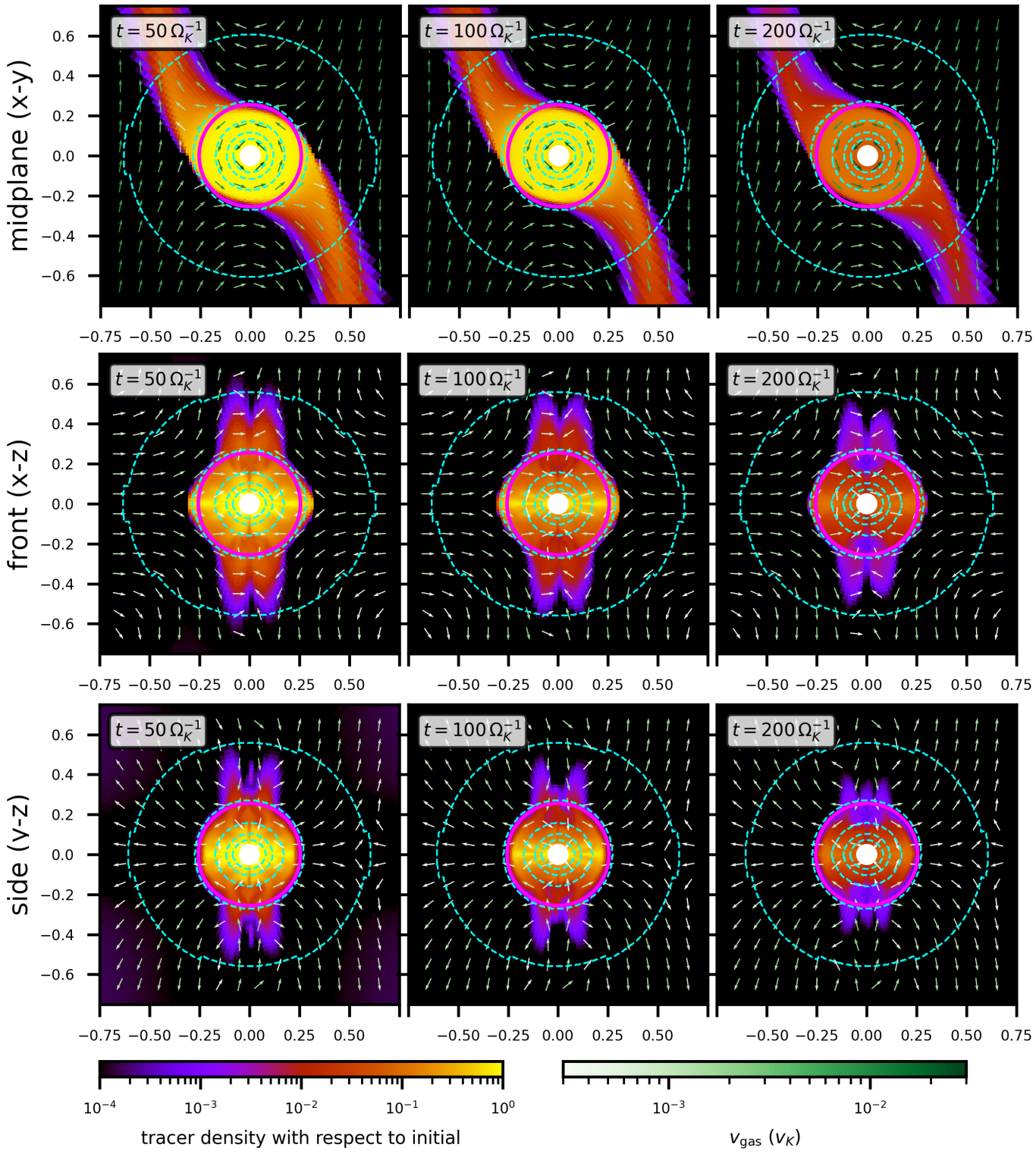

Fig. 5. Evolution of the tracer fluid inserted into the Hill sphere of the M1 simulation after thermodynamic equilibrium was reached. At $t = 0\,\Omega_K^{-1}$, the whole Hill sphere is filled with a uniform tracer fluid concentration of unity. The top panel shows the view of the midplane, the middle panel the view of the front, and the bottom panel the side view. The length unit used is $R_{\rm Hill}$. The dashed cyan lines are iso-density lines at $[2, 4, 8, 16, 32]\,\rho_0$. The magenta circle is the atmospheric radius $R_{\rm atm}$, defined such that inside $R_{\rm atm}$, the azimuthal velocity is the largest component everywhere in the midplane, i.e., the gas rotates around the protoplanetary core. The atmosphere is elongated in the x-z view because of the stellar tidal forces.

for the M1 simulation in figure 2. After the planetary gravity is switched on, gas accumulates around the planetary core and three distinctive flow regions develop from the initial shearing flow. Around the planetary core, a protoplanetary atmosphere forms in which the gas flow is dominated by the planetary gravity. In this region, the gas rotates around the planetary core in the azimuthal direction. Here, up to $0.9\,R_{\rm atm}$, the radial and meridional velocity components do not exceed 5 % of the total velocity, while at $1.1\,R_{\rm atm}$, for example, the meridional velocity already exceeds 15 % of the total velocity. Along the orbital tra-

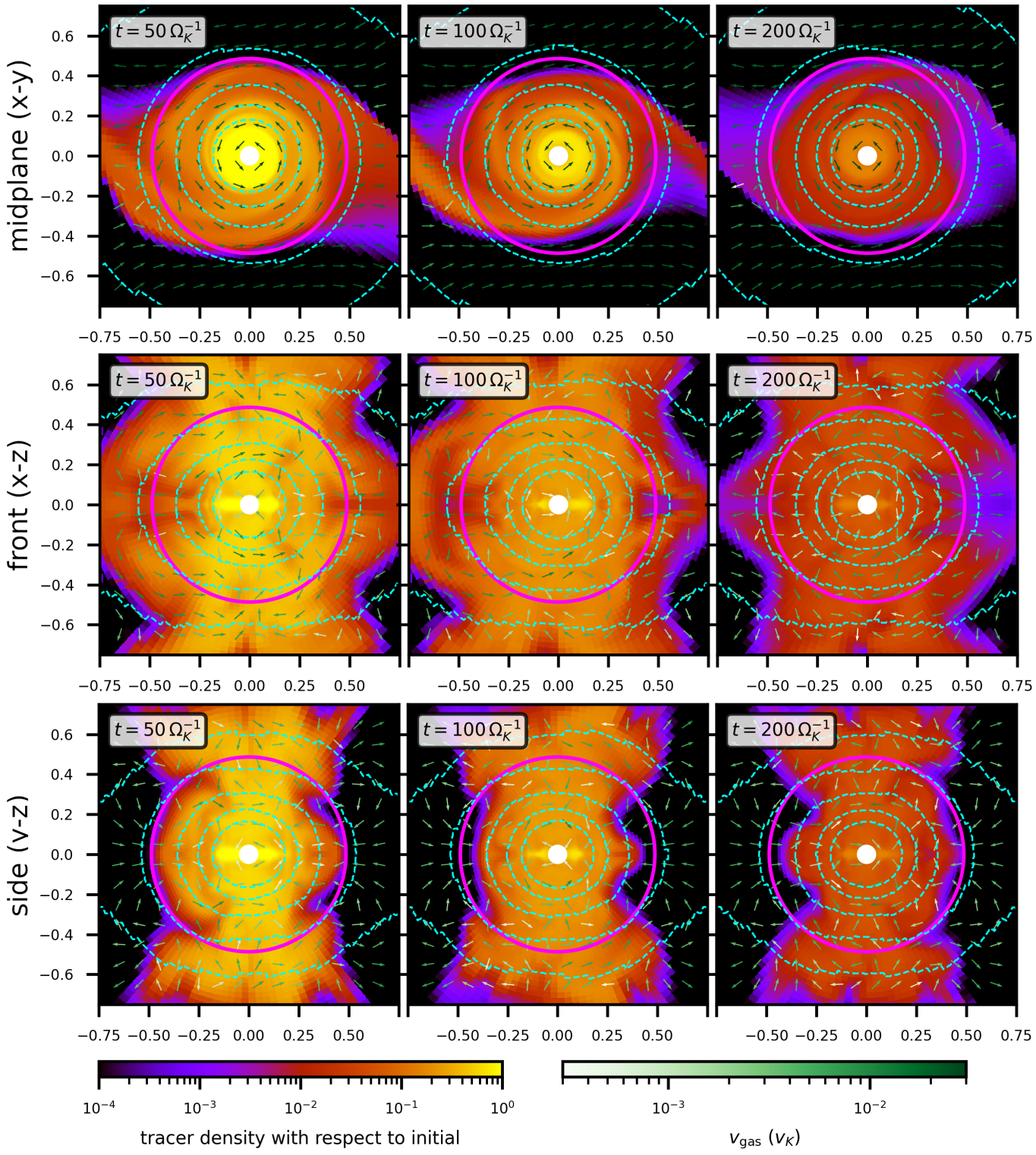

Fig. 6. Same as Figure 5, but for M10. Even though the simulation is in thermodynamic equilibrium, the velocity field changes between snapshots and the atmosphere is asymmetric.

jectory of the planet, two horseshoe orbits develop, one in front of the planet, and one behind. Farther away from the planet in the x-direction, the velocity field is dominated by stellar gravity, and the gas in the local frame follows the shearing flow of the disk, that is, the gas rotates around the central star. The rotational direction of the protoplanetary atmosphere is against the shearing flow, but is aligned with the horseshoe orbits. This is due to the conservation of angular momentum, hence the rotational vector of the planetary atmosphere is aligned with the rotational vector of the circumstellar disk. It becomes clear that the planetary proto-atmosphere and the circumstellar disk are strongly interlinked and have to be studied together. The protoplanetary atmosphere is not isolated from the circumstellar disk.

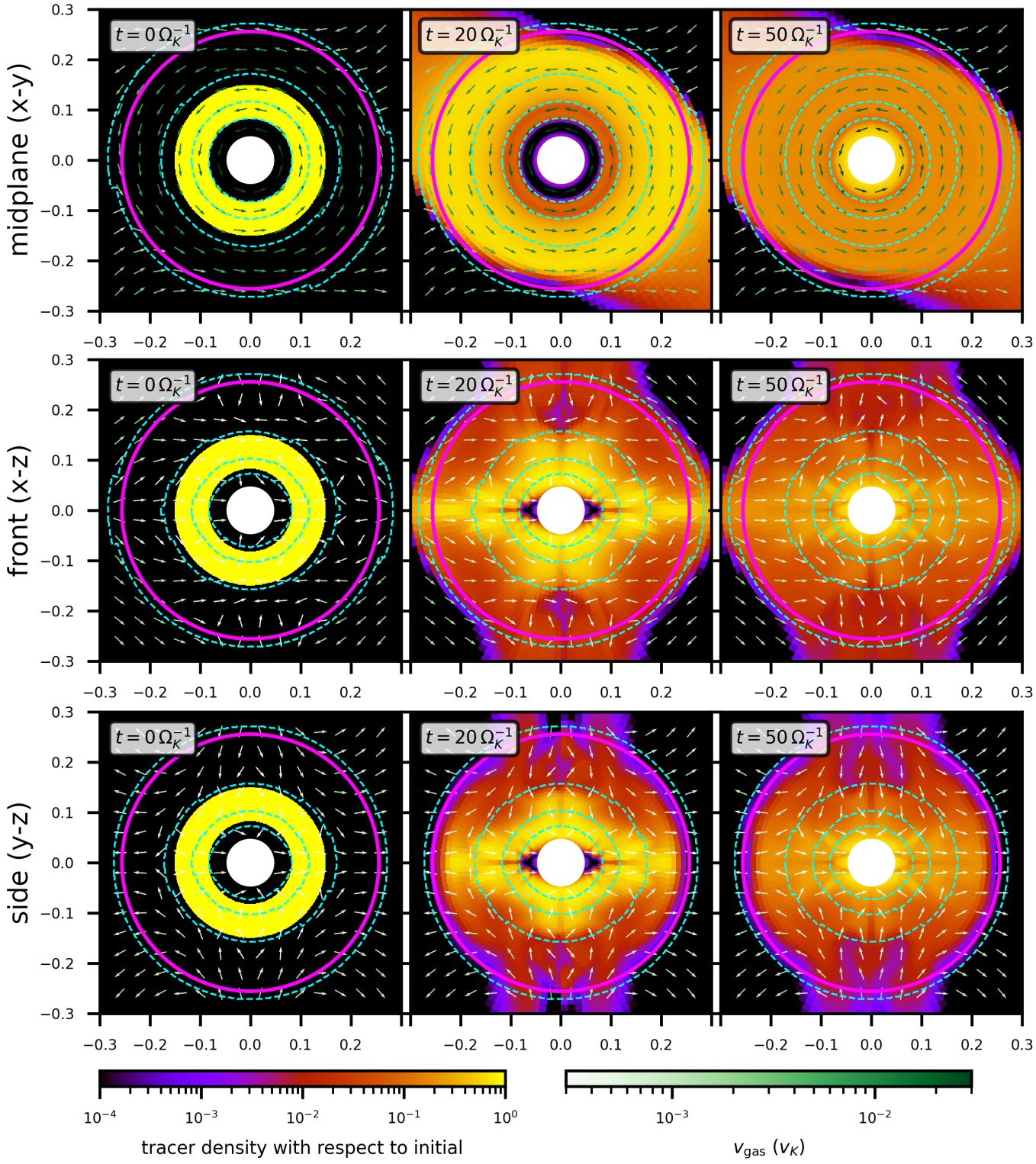

Fig. 7. Same as Figure 5, but only a small shell around the core was filled with tracer fluid. The gap between the tracer fluid filled shell and the protoplanetary core highlights how the inner parts of the atmosphere are recycled.

4.2. Thermodynamic equilibrium

In Moldenhauer et al. (2021), we showed that the M1 setup eventually reaches a steady state in which radiative cooling is fully compensated for by atmosphere-disk recycling, that is, an exchange of entropy between the atmosphere and the circumstellar disk by gas advection. Radiative cooling transports energy outward and recycling of low-entropy atmospheric gas with high-entropy circumstellar gas transports energy inward, while the net mass flux across shells effectively vanishes. The cooling timescale itself is not measured, but the temperature and density are observed to eventually become constant in time, indicating that radiative cooling is fully compensated for by atmospheric recycling. This shows that the cooling timescale is longer than the recycling timescale despite the very low opacity, high-

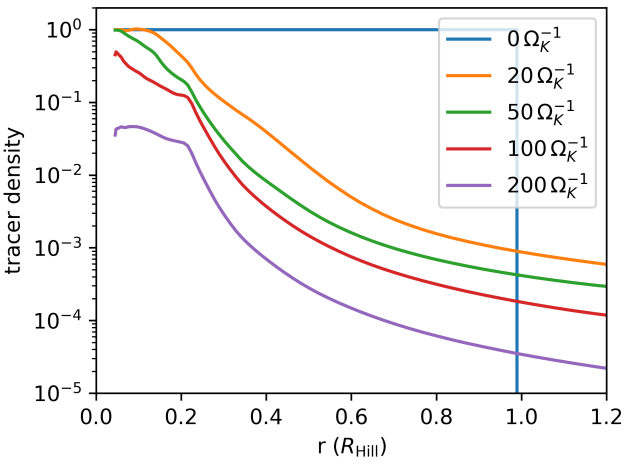

Fig. 8. Evolution of the 1D-averaged tracer fluid concentration in the Hill sphere of the M1 simulation. The M1 simulation reached thermodynamic equilibrium after $\approx 300\,\Omega_K^{-1}$ and the tracer fluid was inserted after $2000\,\Omega_K^{-1}$. After $200\,\Omega_K^{-1}$, the tracer fluid concentration decreased to less than 5 % even in the inner regions of the protoplanetary atmosphere. This figure shows that the recycling timescale is $\sim 100\,\Omega_K^{-1}$, explaining that thermodynamic equilibrium is reached after $\sim 100\,\Omega_K^{-1}$.

lighting the efficiency of the recycling process. The simulations in this paper explore a wide range of core masses and a scenario with and without headwind. All our simulations eventually reached thermodynamic equilibrium after $\approx 300\,\Omega_K^{-1}$, which is on the same order of magnitude as their respective recycling timescales. In thermodynamic equilibrium, the atmosphere does not continue to cool, despite a continuous loss of radiation energy. Only smaller random oscillations remain, which tend to be stronger for higher core masses. For all simulations, the spherically averaged temperature oscillates by less than 1 % and the spherically averaged density by less than 2 %. This thermodynamic equilibrium does not necessarily mean that the flow structure needs to be constant in time. For higher core masses, we observe that the atmosphere starts to become turbulent. Here, the velocity field changes in time, but the simulations stay in thermodynamic equilibrium.

Additionally, we were able to remove the oscillations caused by the initial collapse of the atmosphere that were reflected by the radial boundaries. To remove the oscillations, we ran the simulations until they reached equilibrium and then averaged over several hundred output files at an output frequency of $1\,\Omega_K^{-1}$. We then continued the simulation from this averaged state. The turbulent flow observed for higher core masses is independent of these oscillations. Removal of these oscillations did not change the equilibrium temperature or the recycling time of the atmosphere. However, for maximum accuracy, we performed all post-processing steps from this averaged state.

4.3. Characteristics of the gas flow

In order for atmospheric gas to recycle, there have to be regions in which the atmosphere accretes material and regions in which material leaves the atmosphere, that is, a continuous exchange of gas between the atmosphere and the circumstellar disk. Figure 4 displays the trajectories of two tracer particles that start in the midplane close to the planetary core at almost the exact same position. Both tracer particles start with the same distance to the core, they only differ slightly in their initial azimuthal coordinate. At first, both particles spiral outward while being stuck in the midplane, that is, $z \approx 0$. After they reach a distance to the center of the core $\sqrt{r^2 - z^2} \approx R_{\rm atm}$, they reach the zone where the gas from the protoplanetary atmosphere starts to mix with the circumstellar gas from the horseshoe orbits. Here, they drift away from the midplane and rapidly gain altitude before they slowly move back toward the midplane. During this vertical mixing process, the particles oscillate around a distance of $\sqrt{r^2 - z^2} \approx R_{\rm atm}$ from the center of the vertical axis. The process then repeats and the particles again move away from the midplane. The particle represented by the orange trajectory is then picked up by one of the horseshoe orbits and is removed from the Hill sphere, while the particle represented by the blue trajectory repeats the drift toward the midplane for a second time before it is finally ejected. This illustrates how sensitive the trajectories of the tracer particles are to the initial conditions. The boundary between the protoplanetary atmosphere and the horseshoe orbits features an irregular flow pattern causing continuous mixing between the atmospheric and circumstellar gas. For previous 2D simulations (Ormel et al. 2015a), a well-defined separatrix existed that separated the atmosphere from the circumstellar flow. In 3D the topology is different and this clear distinction is no longer possible.

4.4. Recycling of the entire atmosphere and turbulence

Figure 5 shows the tracer fluid concentration at different points in time for the M1 simulation. The tracer fluid was introduced with a concentration of unity inside the Hill sphere after the simulation reached thermodynamic equilibrium. The protoplanetary atmosphere is slightly elongated in the x-direction, as can be seen when the front view is compared to the side view. This is because of the stellar tidal forces that stretch the atmosphere along the radial direction. Except for directly above and below the planetary core, the region outside of $R_{\rm atm}$ is cleared from the tracer fluid more than 2 orders of magnitude faster than inside, indicating that this region is not part of the atmosphere. After only $50\,\Omega_K^{-1}$, the tracer fluid concentration in this region is lower than 10^{-4}, except for the horseshoe region, where the tracer fluid from the atmosphere is transported away. This observation agrees with the structure of the velocity field because only for $r < R_{\rm atm}$ does the gas rotate around the protoplanetary core. This motivates our definition of $R_{\rm atm}$ from section 2.2 as it marks the transition from short recycling to significantly longer recycling.

The high-mass case is depicted in figure 6, which shows the time evolution of the tracer fluid for the M10 simulation. Here, the protoplanetary atmosphere is asymmetric compared to the low-mass case. The asymmetries arise from turbulence, which can be observed by the changing velocity field especially in the front and side view. However, as the turbulence occurs on a subsonic timescale, it is only visible in the velocity field. Even the turbulent simulations eventually enter thermodynamic equilibrium where density and temperature stay approximately constant in time. When we compared the displayed tracer fluid densities to results where we artificially kept the velocity field constant after the tracer fluid was injected, we observed that for higher core masses, the resulting tracer fluid density was significantly different. This is because the random changes in the velocity field for the high-mass case have a significant impact on the recycling process. Turbulence affects the recycling process in two ways: At the boundary layer between the atmospheric flow around the planetary core and the horseshoe orbits, it in-

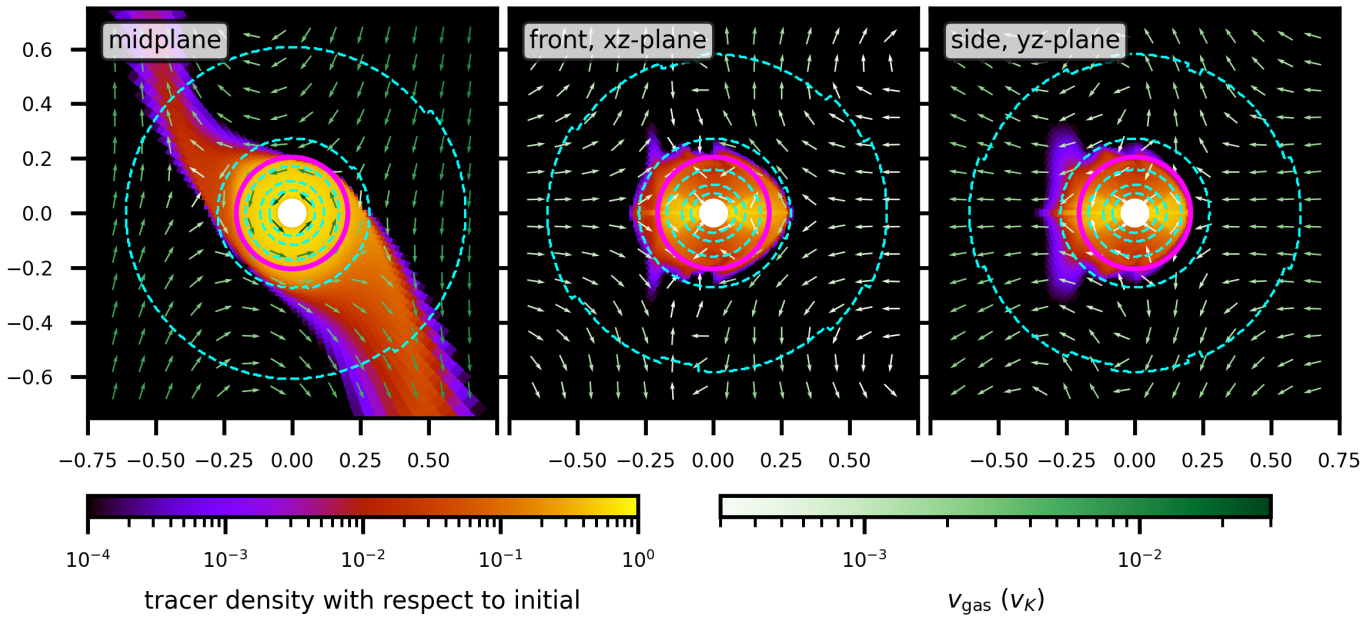

Fig. 9. Tracer fluid density at $t = 100\,\Omega_K^{-1}$ after the tracer fluid was injected into the Hill sphere of the M1-HW simulation after it reached thermodynamic equilibrium. The headwind shifts the horsehoe orbits toward the star, which results in asymmetric recycling streams. Additionally, the headwind recycles the gas directly above and below the protoplanetary atmosphere.

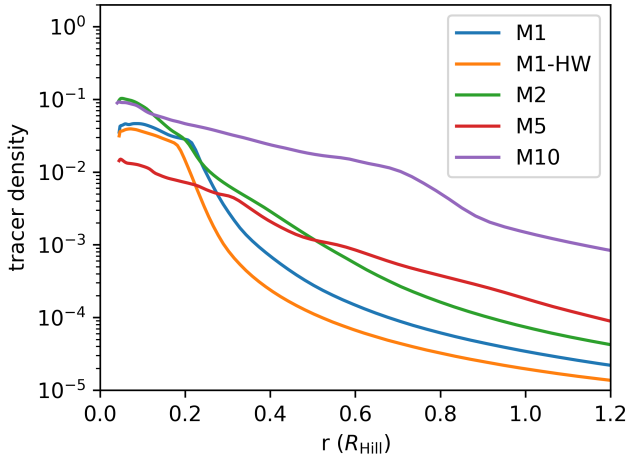

Fig. 10. 1D-averaged tracer fluid concentration for different core masses at $t = 200\,\Omega_K^{-1}$ after the fluid was introduced into thermodynamic equilibrium.

creases mixing. Additionally, turbulence increases the mixing inside the atmosphere, that is, it transports low-entropy gas toward the boundary layer and recycles high-entropy gas from the boundary layer to the inner parts of the atmosphere. The addition of viscosity to our inviscid simulations might soften or remove the observed turbulent flow and provide additional heating.

In Figure 7 we highlight how the gas is distributed inside the inner parts of the M1 simulation. First, we waited for the simulation to enter thermodynamic equilibrium, then we filled a small spherical shell around the planetary core with the tracer fluid. We intentionally left a small gap between the spherical shell filled with tracer fluid and the planetary core. This allowed us to show that even the innermost regions of the atmosphere are recycled efficiently. After the introduction of the tracer fluid, we let the simulation continue to evolve in its thermodynamic equilibrium. The tracer fluid was quickly distributed throughout the entire protoplanetary atmosphere on a timescale of $t_{\rm mix} \sim 10\,\Omega_K^{-1}$, including the region between the initial tracer fluid location and the core. The inner region that was initially left without tracer fluid was eventually filled with tracer fluid primarily through the vertical direction. The midplane region of the inner atmospheric parts took longest to be filled with tracer fluid as this is the region in which gas is being transported outwards. At the boundary between the horseshoe orbits and the atmosphere, some of the tracer fluid mixed with the gas of the horseshoe orbit and was transported away from the planet and back into the circumstellar disk. This process slowly decreased the tracer fluid concentration in the atmosphere, showing how the gas is being recycled on a timescale of $t_{\rm rec} \sim 100\,\Omega_K^{-1}$. In addition to the gas exchange through the horseshoe orbits, gas was accreted along the vertical axis, indicated by the lower tracer fluid concentration along the vertical axis compared to the midplane. In agreement with the tracer particle trajectories, the tracer fluid shows that the gas inside the protoplanetary atmosphere is constantly mixed and gas is exchanged with the circumstellar disk through the horseshoe orbits and through vertical infall.

In Figure 8 we show the evolution of the 1D-averaged tracer fluid concentration inside the Hill sphere for the M1 simulation. Initially, all cells that are fully within the Hill sphere were filled with a tracer fluid. When we then continued to evolve the simulation, the tracer fluid concentration started to decrease. While the concentration in the inner regions, $r < R_{\rm atm}$, decreased more slowly, all regions experience a depletion of the tracer fluid on a recycling timescale $t_{\rm rec} \sim 100\,\Omega_K^{-1}$. After $200\,\Omega_K^{-1}$, the tracer fluid concentration decreased to lower than 5 % everywhere within in the protoplanetary atmosphere. This shows that even the atmospheric region in which the gas rotates around the protoplanetary core is recycled relatively quickly. Additionally, this explains why it takes $\sim 100\,\Omega_K^{-1}$ for the simulation to reach thermodynamic equilibrium.

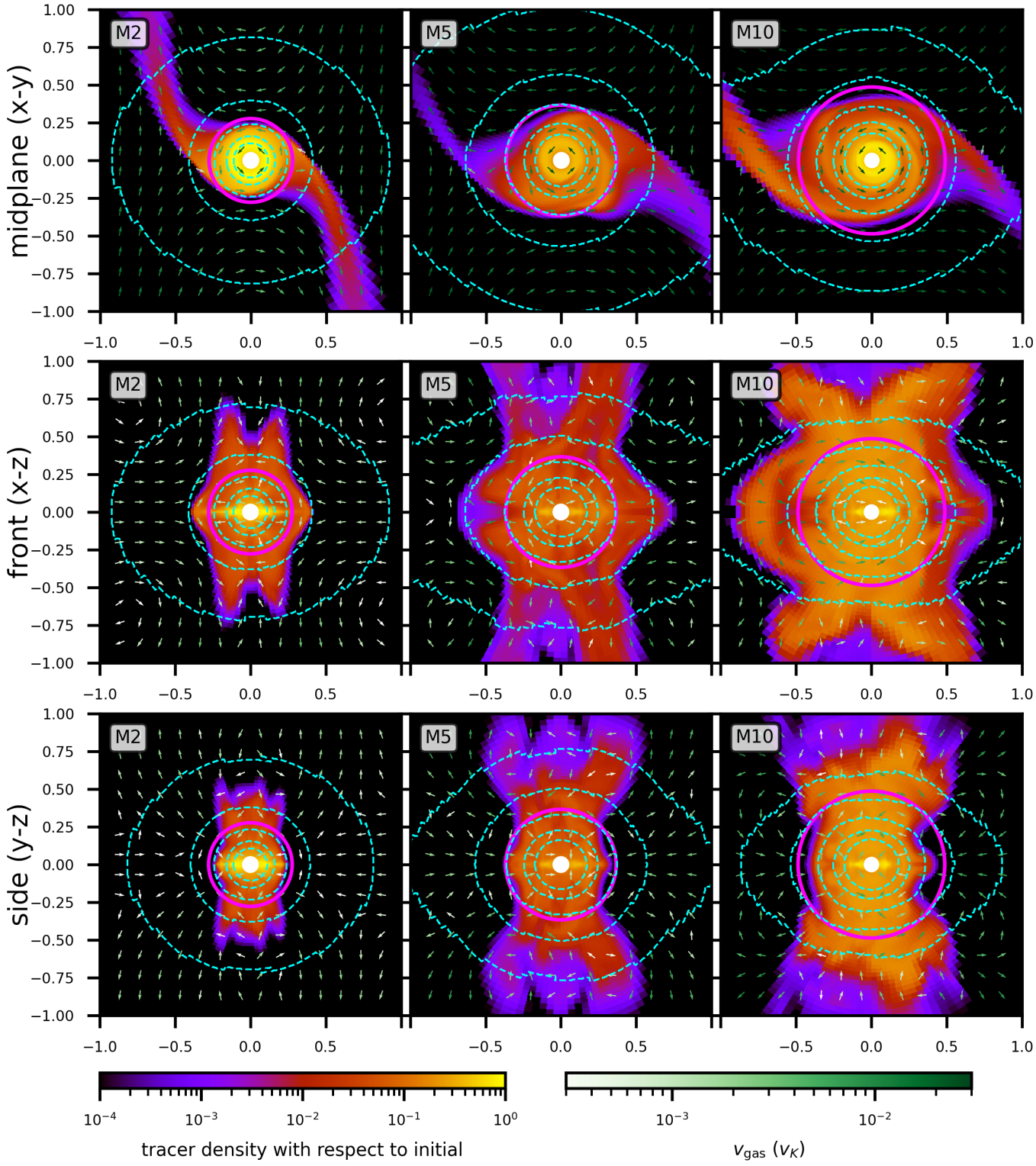

Fig. 11. Tracer fluid distribution for simulations with different core masses. After thermodynamic equilibrium is reached, the Hill sphere is initialized with a tracer density of unity and is evolved for an additional $100\,\Omega_K^{-1}$. The length unit for all panels is $R_{\rm Hill}$, which scales with the mass of the core. Because we assumed the same density for all cores, the cores have the same radius in units of $R_{\rm Hill}$. Top panel: Tracer fluid density in the midplane. Bottom panel: Tracer fluid density in the xy-plane seen from the front.

5. Parameter study

To understand the parameters that determine the efficacy of atmospheric recycling, we conducted a parameter study. First, we analyze the effect of the headwind that the protoplanet experiences in section 5.1. In section 5.2, we then analyze the influence of the planetary core mass on the structure of the atmosphere and on the resulting recycling timescale. Because the boundaries have improved and new postprocessing techniques are available, we revisit the claim of Cimerman et al. (2017) that opacity has little effect and determine its influence on the recycling timescale. Finally, section 5.4 investigates the influence of

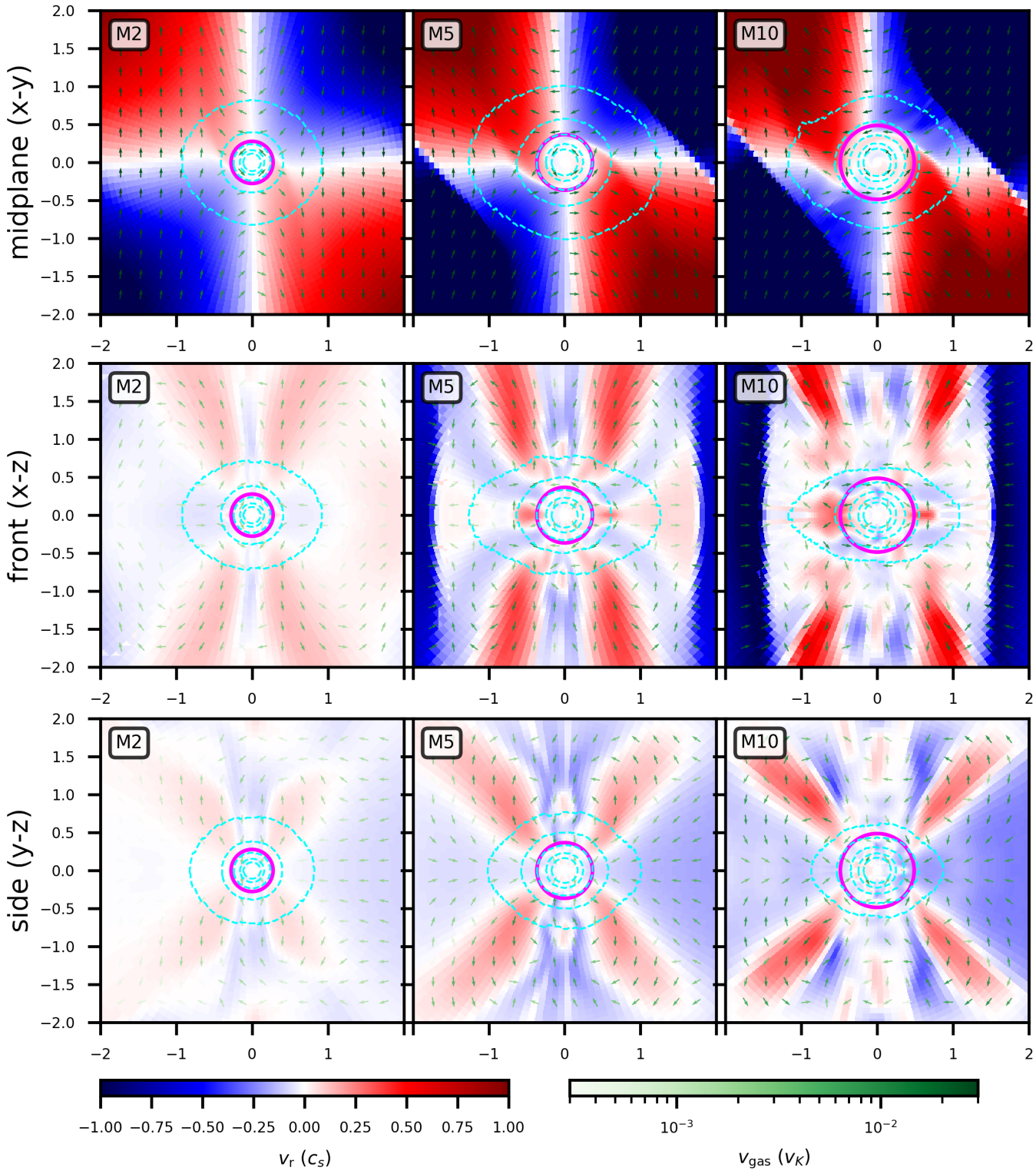

Fig. 12. Radial velocity component in units of the local sound speed. The top panel shows the view from the midplane, the middle panel shows the view from the front, and the bottom panel shows the side view. The length unit used is $R_{\rm Hill}$. The dashed cyan lines are iso-density lines at $[2, 4, 8, 16, 32]\,\rho_0$. The magenta circle is the atmospheric radius $R_{\rm atm}$ (see Fig. 5).

all studied parameters on the final atmospheric mass in thermodynamic equilibrium.

5.1. Recycling with headwind

Including the headwind introduces an asymmetry: The horseshoe orbits are no longer centered on the protoplanet, but are shifted toward the star. The gas that rotates around the star with the same frequency as the planet has a smaller separation from the star. This asymmetry allows the horseshoe orbits to penetrate

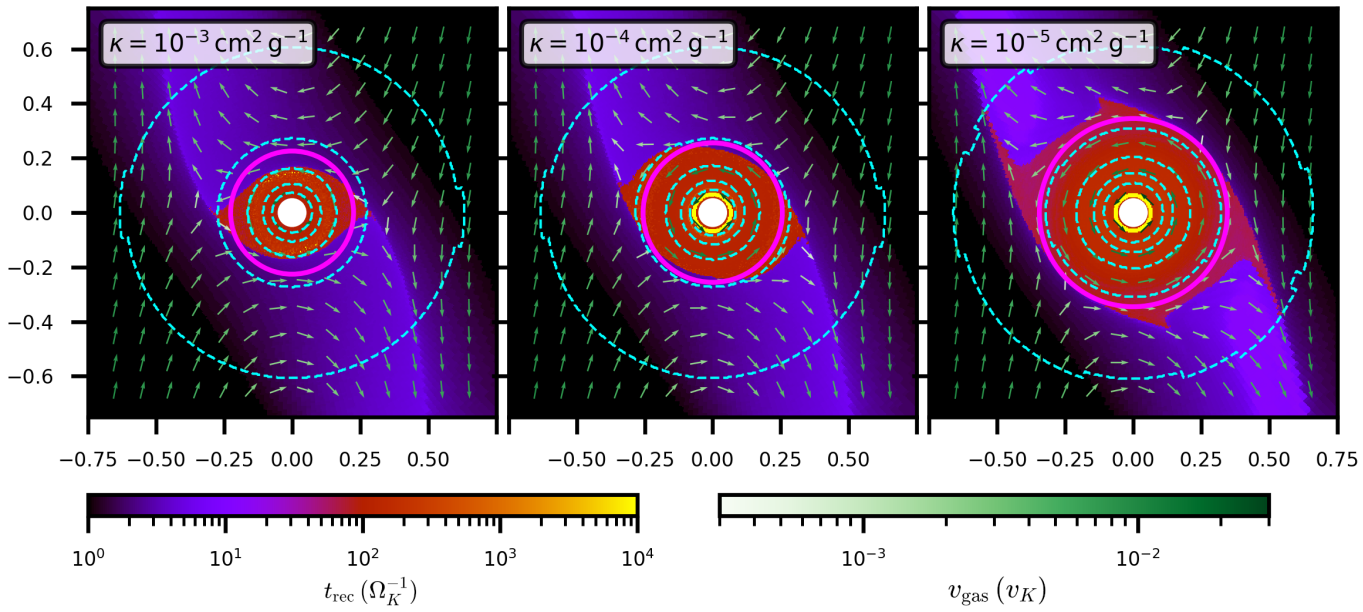

Fig. 13. Recycling timescale measured using tracer particles for simulations with different opacities. The center panel is the M1 simulation, which uses our default opacity. After thermodynamic equilibrium is reached, tracer particles are integrated along streamlines backward in time. The measured time until they then escape the Hill sphere is the plotted recycling time. It measures for how long the gas has been inside the Hill sphere.

deeper into the protoplanetary atmosphere, potentially increasing the recycling rate. Figure 9 shows the evolution of the tracer fluid for the M1-HW simulation. As expected, the recycling streams are no longer symmetric. Compared to the simulation without headwind, more tracer fluid leaves the protoplanetary atmosphere behind the planet, but in turn, less tracer fluid leaves the atmosphere in front of the planet. This is a result of the shift of the horseshoe orbits toward the star. Additionally, the headwind causes the regions of slow recycling along the vertical axis to disappear. Gas that was previously able to accumulate along the vertical axis is now swept away by the headwind. Instead, this region also moved toward the star, as is visible from the side view of the protoplanetary atmosphere. The density structure is not affected as it is dominated by the core gravity instead of the flow structure. These effects result in a generally slightly smaller protoplanetary atmosphere. However, even though we overestimated the headwind magnitude by roughly a factor of 5, the effect on the size of the atmosphere is relatively small. For higher core masses and therefore higher thermal masses, the effects of the headwind become even weaker.

5.2. Core mass comparison

In section 4.4 we have explained one key difference between lower core masses and higher core masses: for higher core masses, the velocity field changes in time even after thermodynamic equilibrium was reached. In this section, we explore the effects of the core mass on the recycling of the protoplanetary atmosphere. We waited until our simulations with core masses $M_c \in [2, 5, 10]$ reached thermodynamic equilibrium, where the density and temperature distribution of the atmosphere become constant in time. While thermodynamic equilibrium was reached after $\approx 300\,\Omega_K^{-1}$, we simulated for $1000\,\Omega_K^{-1}$ before injecting the tracer fluid in the Hill sphere.

Figure 11 displays the tracer fluid concentration at $t = 100\,\Omega_K^{-1}$ after it was injected for our simulations with core masses $M_c \in [2, 5, 10]\,M_{\mathrm{Earth}}$. The length scale used is R_{Hill}, which increases with the mass of the core. Because we assumed the same planetary core density for all core masses, the size of the core is identical and measured in R_{Hill} across all simulations: $R_{\mathrm{core}} = 0.044\,R_{\mathrm{Hill}}$. However, even with this variable scaling, the displayed atmosphere increases with core mass. This means that the size of the atmosphere increases faster than the radius of the core and the Hill sphere when the core mass is increased. The midplane view of figure 11 shows that as the core mass increases, more structure develops. The front and side views also show that the protoplanetary atmosphere becomes increasingly asymmetric for higher core masses. These asymmetries are not constant in time but change continuously as the simulation progresses and are caused by the onset of turbulence in the high-mass case. However, because the velocity field changes occur on a subsonic timescale, the temperature and density profile stay approximately constant in time. Although the atmosphere for higher core masses is turbulent, the protoplanetary atmosphere remains in thermodynamic equilibrium. Additionally, the larger atmosphere causes the tidal effects to be more pronounced, for higher core masses the atmosphere is significantly more stretched in the x-direction compared lower core masses. In the high-mass case, the density distribution appears less spherical and is squished in the vertical direction. However, this is mainly due to the larger size of the atmosphere, in which the vertical stratification of the circumstellar density profile has a stronger effect. The protoplanetary atmosphere itself still remains more spherical.

Figure 12 shows the radial velocity component for the different core masses as a 2D field in units of the local sound speed. At higher core masses, the radial in- and outflow becomes stronger because the gravitational acceleration by the planetary core is stronger. For higher core masses, $M_c > 2\,M_{\mathrm{Earth}}$ accretion shocks develop outside of the Hill sphere. However, as the atmosphere is significantly smaller than the Hill sphere, the whole recycling process occurs at subsonic velocities. Additionally, for higher core masses, the radial velocity also becomes increasingly asymmetric. This is because of the turbulent flow in and around the protoplanetary atmosphere at higher core masses.

For all core masses we analyzed, the azimuthal velocity component is sub-Keplerian at less than 50 % of the Keplerian velocity with respect to the planetary gravity. This shows that the atmosphere is mainly pressure supported, regardless of the core mass. Compared to the low-mass case, the high-mass case results in a flatter rotational velocity profile. This is caused by the more turbulent atmosphere at higher core masses. Previous studies also found a mainly pressure-supported atmosphere (Moldenhauer et al. 2021; Cimerman et al. 2017).

5.3. Opacity comparison

For our simulations we deliberately chose a very low opacity, $\kappa = 10^{-4}\,\mathrm{cm^2\ g^{-1}}$, in order to keep the cooling timescale short and therefore save on computation time. This raises the question whether this decreased opacity affects the recycling timescale. Additionally, we did not include self-gravity and the opacity was constant, therefore changing the opacity has the same effect on the flow structure as changing the ambient density of the disk. Here, we explore simulations with $\kappa = 10^{-3}\,\mathrm{cm^2\ g^{-1}}$ and $\kappa = 10^{-5}\,\mathrm{cm^2\ g^{-1}}$. While these opacities are still considerably lower than what would be realistically expected, they serve as a good comparison to verify the effect that opacity has on the recycling timescale. All our simulations start optically thick and only slightly increase their optical depth when thermodynamic equilibrium is reached. In Figure 13 we display the recycling time measured using tracer particles for the different opacities. Other parameters such as the boundary temperature or the disk velocity profile remain unchanged by this change in opacity. The size of the atmosphere increases when the opacity is decreased, which at first glance seems counterintuitive. In the regime of optically thick atmospheres, a lower opacity results in a higher radiative flux and in an increase in cooling efficiency; the atmosphere therefore contracts more. This results in a higher pressure gradient, which in turn allows for a larger pressure-supported atmosphere. However, as Figure 13 shows, the recycling timescale remains unchanged. The opacity only affects the local cooling timescale, while the recycling timescale is affected by the core mass and probably by the global dynamical timescale at the location of planet. The cooling timescale and the recycling timescale are therefore independent of each other. Because of our artificially low opacity and the result that the recycling timescale is independent of the cooling timescale, we can conclude that at realistic opacities recycling will also halt the contraction of the atmosphere at the explored parameter space.

The rotational velocity of the atmosphere significantly increases when the opacity is decreased. This is because of the contraction of the lower entropy atmosphere and the conservation of angular momentum. However, outside of the protoplanetary atmosphere toward the circumstellar shearing flow, the opacity has virtually no effect on the gas velocity. As expected, the opacity only changes the local behavior of the atmosphere.

5.4. Atmosphere size and mass

To determine the atmospheric mass, we used the atmospheric radius R_{atm} , which we defined based on dynamical arguments measured in thermodynamic equilibrium, as explained in Sect. 2.2. Additionally, for easy comparison with other work, we calculated the mass inside the Hill sphere and Bondi sphere. The minimum of the Bondi and Hill radius is often quoted as an upper limit for the size of the atmosphere as the gas outside either escapes because of the stellar gravity or the thermal pressure.

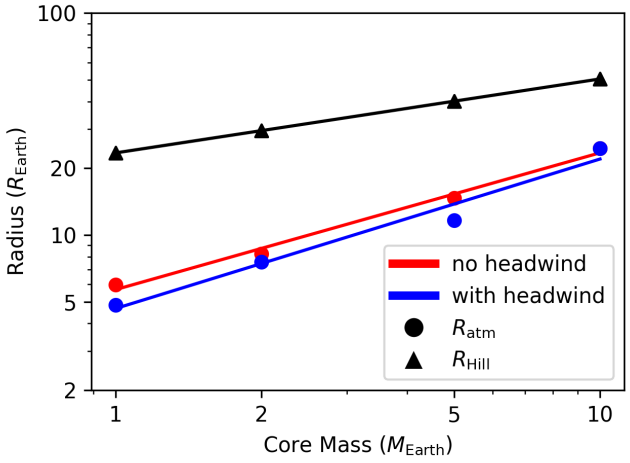

Fig. 14. Comparison of the atmospheric radius for different core masses and headwind parameters. The Hill radius is by definition independent of the headwind parameter. We fit a power law to the data points $R_{\mathrm{atm}}/R_{\mathrm{Earth}} = a \cdot (M_c/M_{\mathrm{Earth}})^n$ using the relative least-squares method. When the headwind is included, we obtain $a = 4.7 \pm 0.6, n = 0.67 \pm 0.08$. Without the headwind, the result of the fit is $a = 5.7 \pm 0.3, n = 0.62 \pm 0.04$.

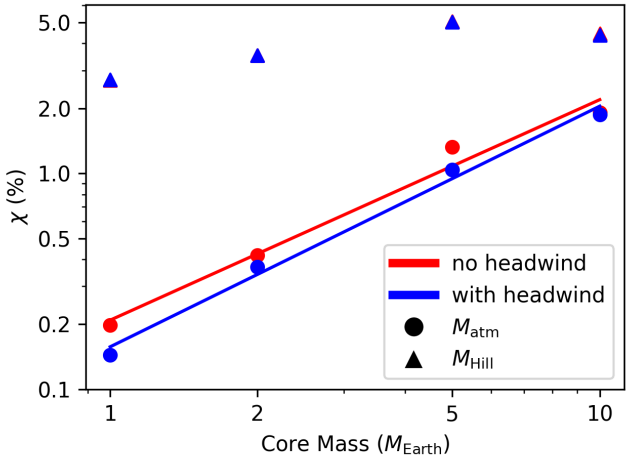

Fig. 15. Comparison of the atmosphere-to-core mass ratio, $\chi := M_{\mathrm{atm}}/M_{\mathrm{c}}$, for different core masses and headwind parameters. For the mass inside the Hill sphere, the data points overlap for the different headwind parameters. We fit a power law to the data points $\chi = a \cdot (M_c/M_{\mathrm{Earth}})^n\,\%$ using the relative least-squares method. When the headwind is included we obtain $a = 0.16 \pm 0.02, n = 1.1 \pm 0.1$. Without the headwind, the result of the fit is $a = 0.21 \pm 0.03, n = 1.0 \pm 0.1$.

However, because we did not observe a traditional gravitationally bound atmosphere, they have little physical meaning in our case besides serving as a length scale. When we talk about the protoplanetary atmosphere, we refer to the region inside R_{atm}.

Table 1 shows the radii and mass of these three spheres for the different simulations. All simulations result in atmospheric masses well below the core mass. Hence, the envelope does not become self-gravitating and is therefore well below the critical core mass for runaway gas accretion (Mizuno et al. 1978). The Bondi radius quickly increases with the core mass, and the Hill radius becomes the limiting parameter for the size of the atmosphere for planetary core masses $M_c \geqslant 2\,M_{\mathrm{Earth}}$. The size of the atmosphere measured with the described method, R_{atm}, also sig-

nificantly increases with core mass. Together with the higher gas densities at higher core masses, this results in an increased atmospheric mass, $M_{\rm atm}$, and in an increased atmospheric mass ratio, $\chi := M_{\rm atm}/M_{\rm c}$. The atmospheric mass and the atmospheric radius values from Table 1 are visualized graphically in Figs. 14 and 15, and a power-law fit to the atmospheric radius and mass is applied. The calculated exponents are within errors: they are the same for the headwind case and for the case without headwind. The size of the measured atmosphere approximately scales with $M_c^{2/3}$ and the mass ratio of the atmosphere scales linearly with the core mass ($\chi \sim M_c \Rightarrow M_{\rm atm} \sim M_c^2$). This means that the steeper density profile for higher core masses has little effect on the total atmospheric mass, that is, most of the atmospheric mass is contributed by the outer layers of the atmosphere. The higher atmospheric mass at higher core masses comes from the increase in atmospheric size instead of the increase in density.

If a headwind is included, the Bondi radius becomes slightly smaller for the simulations with $M_c \geqslant 5$, indicating a slightly hotter atmosphere because of the increase in recycling efficiency, hence, a stronger radiative cooling and contraction as well. We suspect that the same effect also occurs for lower core masses, but is too small to be measurable. The Hill radius is independent of the headwind parameter by definition. All simulations with a headwind show a smaller $R_{\rm atm}$ because the horseshoe orbits penetrate more deeply. This effect significantly decreases the mass that rotates around the planetary core, $M_{\rm atm}$, as the atmospheric size is the dominant factor for the atmospheric mass. At $M_c = 10\,M_{\rm Earth}$, the thermal mass is so high that this effect becomes less significant because the gravity of the planetary core starts to dominate the flow structure. The shift of the horseshoe orbits is less noticeable compared to the size of the atmosphere at higher planetary core masses.

For the simulations with different opacities M1-HO, M1, and M1-LO, the change in the gas density is relatively small, as can be seen from the mass inside the Hill sphere, $M_{\rm Hill}$. A decreased opacity, that is, a higher cooling efficiency, results in a slightly higher atmospheric mass because of the increased density. Considering that we varied the opacity by orders of magnitude here, the change in atmospheric mass is comparatively minor. However, if we take the change in the size of the atmosphere $R_{\rm atm}$ caused by the change in opacity into account, the mass of the atmosphere changes significantly.

6. Discussion

6.1. Atmosphere-disk recycling and thermodynamic equilibrium

In Moldenhauer et al. (2021), we showed that atmosphere-disk recycling is capable of fully compensating for radiative cooling. With our parameter study, we here confirmed that this holds true even for higher core masses and different opacities. At a separation of $a_p = 0.1$ au, the whole atmosphere is recycled. In addition, we found that for higher core masses, the recycling pattern changes. Instead of a full steady state with a velocity field that is constant in time, we find that for higher core masses, the atmosphere becomes turbulent. However, from a thermodynamic point of view, the simulations still reach equilibrium, where hydrodynamic recycling fully compensates for radiative cooling. Compared to Cimerman et al. (2017), the protoplanetary atmospheres in our simulations are less isolated. Although Cimerman et al. (2017) also observed a fully recycling atmosphere, they found a significantly sharper entropy gradient between the inner parts of the atmosphere and the disk. We suspect that this is because a bug in their boundary conditions forced them to use gravitational smoothing and because their atmosphere is still contracting. In this regard, our results are more similar to the 3D isothermal simulations of Béthune & Rafikov (2019), where the transition is smoother. Kurokawa & Tanigawa (2018) observed in their nonisothermal simulations that recycling was suppressed by a buoyancy barrier caused by the entropy gradient in the atmosphere. In our simulations, we did not observe a buoyancy barrier that inhibits recycling of the inner regions.

6.2. In-situ formation at 0.1 au

For our simulations we deliberately chose a very low opacity to keep the Kelvin-Helmholtz cooling timescale short, favoring the formation of larger and more massive atmospheres. According to our findings in section 5.3, a higher, more realistic opacity would result in a significantly smaller and less dense atmosphere. Thus, the atmospheric mass would be even lower.

At the chosen separation of $a_p = 0.1$ au, the recycling mechanism is so efficient that even for our highest core mass of $M_c = 10\,M_{\rm Earth}$, the atmospheric mass ratio only reaches $\chi = 2\,\%$. Extrapolating figure 15 suggest that for even higher core masses than the range we explored, the atmosphere-to-core mass ratio would still not grow high enough for runaway gas accretion to be possible. This is in agreement with Fung et al. (2019), who found in their 3D simulations that the atmospheric mass ratio stays below 10 % even for $M_c = 20\,M_{\rm Earth}$ and an isothermal equation of state. We suspect that the atmospheric mass ratio will increase for larger separations as the recycling timescale scales with the dynamical timescale, Ω_K^{-1}. A longer recycling timescale corresponds to a lower rate at which high-entropy circumstellar gas enters the atmosphere. Hence, the atmosphere cools more efficiently. As the separation and thus the dynamical timescale is increased, we suspect that there will be a point at which recycling becomes too inefficient to counteract radiative cooling and more massive atmospheres become possible. Our results show that protoplanetary cores, $M_c \leqslant 10 M_{\rm Earth}$ at 0.1 au, fail to accrete atmospheres with $M_{\rm atm} > \sim 2\,\%$ when atmospheric recycling is taken into account even when the luminosity through the accretion of solids is ignored and an artificially low gas opacity is assumed.

6.3. Rotational profile

Because of the conservation of angular momentum, the rotational support in 2D can be calculated analytically: Gas that is accreted from the circumstellar disk at the Hill sphere has an angular momentum of $R_{\rm Hill}^2 \Omega_K$. By setting this value equal to the angular momentum of the atmosphere $\sqrt{G M_p r}$, we obtain that the atmosphere is rotationally supported up to $R_{\rm rot} \sim R_{\rm Hill}/3$ (Quillen & Trilling 1998). Ormel et al. (2015a) observed in their 2D simulations that because of vortensity conservation, the azimuthal velocity of the atmosphere increases if the gravitational smoothing length is decreased, allowing more gas to flow into the envelope. For their smallest smoothing length, their atmosphere rotates almost at the circumplanetary Keplerian velocity. Vortensity is not a conserved quantity in 3D. Although we used no gravitational smoothing, all our atmosphere rotate at sub-Keplerian velocities. The reason is the inflow of gas from the third, vertical direction. The rotational profile of the 3D simulations in Ormel et al. (2015b) is significantly slower than in the 2D simulations. However, it is still dependent on the gravitational smoothing length used. For their shortest gravitational

smoothing length, their rotational profile at radii larger than the smoothing length is similar to ours.

7. Conclusions and summary

We conducted 3D hydrodynamic simulations with radiative transfer of a protoplanet embedded in a circumstellar disk using a local shearing box approach. Using tracer particles and tracer fluids as post-processing, we compared the flow pattern as well as the atmospheric mass for different planetary core masses, $M_c \in [1, 2, 5, 10]\, M_{\rm Earth}$. We introduced a new radius, $R_{\rm atm}$, motivated by an increase in recycling timescale. Inside $R_{\rm atm}$, the recycling time of the gas is two to three orders of magnitude higher than in the rest of the Hill sphere. Furthermore, we investigated the effect of the headwind and opacity.

Our key findings are summarized below: For all explored parameters, the whole protoplanetary atmosphere is recycled. There is no (inner) region where the gas is never exchanged with the circumstellar disk.

At core masses $M_c > 2\, M_{\rm Earth}$, the atmosphere starts to become increasingly turbulent which further enhances recycling. The size of the atmosphere, $R_{\rm atm}$ increases approximately proportional to $M_c^{2/3}$, that is, stronger than the Hill radius, respectively.

The ratio of the atmosphere to the core mass, $\chi := M_{\rm atm}/M_c$, scales approximately linearly with the protoplanetary core mass. Together with scaling of the atmospheric radius, $R_{\rm atm} \propto M_c^{2/3}$, this means that the increase in density has only a minor effect on the atmospheric mass, that is, most mass comes from the outer layers.

The headwind parameter has only a minor effect on the size and mass of the atmosphere. When the headwind is included, the atmosphere becomes asymmetric, slightly smaller, and therefore less massive.

While our results show that the opacity has a significant effect on the final size and mass of the protoplanetary atmosphere, we also found that the recycling timescale is not affected by the opacity. The recycling and Kelvin-Helmholtz cooling timescale are independent of each other. The cooling timescale is dominated by local effects such as the opacity. We suspect that the recycling timescale will become longer at larger separations because the dynamical timescale is longer. At the explored separation of $a_p = 0.1$ au even for our highest core mass of $10\, M_{\rm Earth}$, the simulation enters thermodynamic equilibrium well before an atmosphere that would support runaway gas accretion is accreted.

To conclude, atmosphere-disk recycling is an important effect capable of counterbalancing radiative cooling within a broad range of environmental conditions. At a separation of $a_p = 0.1$ au, it keeps the ratio of atmosphere to core mass low and efficiently prevents the atmosphere from transitioning into the runaway gas accretion phase.

Acknowledgements. We would like to remember our co-author, colleague and friend Willy Kley who sadly passed away shortly before the acceptance of this paper. Willy was always available for valuable scientific input and advise, and was very eager to maintain a friendly and harmonious atmosphere within his research group and with his colleagues. He will be missed. TWM and RK acknowledge funding through the German Research Foundation (DFG) under grant no. KU 2849/6 as well as support through travel grants under the SPP 1992: Exoplanet Diversity program. RK further acknowledges financial support via the Emmy Noether and Heisenberg Research Grants funded by DFG under grant no. KU 2849/3 and 2849/9. WK acknowledges funding by the DFG through grant KL 650/31. We acknowledge support by the High Performance and Cloud Computing Group at the Zentrum für Datenverarbeitung of the University of Tübingen, the state of Baden-Württemberg through bwHPC and the DFG through grant no. INST 37/935- 1 FUGG.

References

Ali-Dib, M., Cumming, A., & Lin, D. N. C. 2020, MNRAS, 494, 2440
Ataiee, S., Baruteau, C., Alibert, Y., & Benz, W. 2018, A&A, 615, A110
Batygin, K., Bodenheimer, P. H., & Laughlin, G. P. 2016, ApJ, 829, 114
Béthune, W. & Rafikov, R. 2019, MNRAS, 1811
Bitsch, B., Morbidelli, A., Johansen, A., et al. 2018, A&A, 612, A30
Bodenheimer, P. & Pollack, J. B. 1986, Icarus, 67, 391
Chachan, Y., Lee, E. J., & Knutson, H. A. 2021, ApJ, 919, 63
Chiang, E. & Laughlin, G. 2013, MNRAS, 431, 3444
Cimerman, N. P., Kuiper, R., & Ormel, C. W. 2017, mnras, 471, 4662
Ferguson, J. W., Alexander, D. R., Allard, F., et al. 2005, ApJ, 623, 585
Fung, J., Artymowicz, P., & Wu, Y. 2015, ApJ, 811, 101
Fung, J. & Lee, E. J. 2018, ApJ, 859, 126
Fung, J., Zhu, Z., & Chiang, E. 2019, ApJ, 887, 152
Ginzburg, S. & Chiang, E. 2019, MNRAS, 487, 681
Hori, Y. & Ikoma, M. 2010, ApJ, 714, 1343
Ida, S. & Lin, D. N. C. 2004, ApJ, 604, 388
Ikoma, M., Nakazawa, K., & Emori, H. 2000, ApJ, 537, 1013
Johansen, A. & Nordlund, Å. 2020, ApJ, 903, 102
Kuiper, R., Klahr, H., Dullemond, C., Kley, W., & Henning, T. 2010, A&A, 511, A81
Kuiper, R., Yorke, H. W., & Mignone, A. 2020, ApJS, 250, 13
Kurokawa, H. & Tanigawa, T. 2018, MNRAS, 479, 635
Kuwahara, A. & Kurokawa, H. 2020, A&A, 643, A21
Lambrechts, M., Johansen, A., & Morbidelli, A. 2014, A&A, 572, A35
Lee, E. J. & Chiang, E. 2015, ApJ, 811, 41
Lee, E. J., Chiang, E., & Ormel, C. W. 2014, The Astrophysical Journal, 797, 95
Machida, M. N., Kokubo, E., Inutsuka, S.-i., & Matsumoto, T. 2008, ApJ, 685, 1220
Mignone, A., Bodo, G., Massaglia, S., et al. 2007, The Astrophysical Journal Supplement Series, 170, 228
Mizuno, H. 1980, Progress of Theoretical Physics, 64, 544
Mizuno, H., Nakazawa, K., & Hayashi, C. 1978, Progress of Theoretical Physics, 60, 699
Moldenhauer, T. W., Kuiper, R., Kley, W., & Ormel, C. W. 2021, A&A, 646, L11
Mordasini, C. 2014, A&A, 572, A118
Mordasini, C., Alibert, Y., & Benz, W. 2009, A&A, 501, 1139
Nayakshin, S., Dipierro, G., & Szulágyi, J. 2019, MNRAS, 488, L12
Ormel, C. W. 2013, Monthly Notices of the Royal Astronomical Society, 428, 3526
Ormel, C. W. 2014, ApJ, 789, L18
Ormel, C. W., Kuiper, R., & Shi, J.-M. 2015a, mnras, 446, 1026
Ormel, C. W., Shi, J.-M., & Kuiper, R. 2015b, mnras, 447, 3512
Papaloizou, J. C. B. & Terquem, C. 1999, ApJ, 521, 823
Perri, F. & Cameron, A. G. W. 1974, Icarus, 22, 416
Pollack, J. B., Hubickyj, O., Bodenheimer, P., et al. 1996, Icarus, 124, 62
Quillen, A. C. & Trilling, D. E. 1998, ApJ, 508, 707
Rafikov, R. R. 2006, ApJ, 648, 666
Schlecker, M., Mordasini, C., Emsenhuber, A., et al. 2021, A&A, 656, A71
Szulágyi, J., Masset, F., Lega, E., et al. 2016, MNRAS, 460, 2853
Tanigawa, T., Machida, M., & Ohtsuki, K. 2012, in European Planetary Science Congress 2012, EPSC2012–610
Weiss, L. M., Marcy, G. W., Petigura, E. A., et al. 2018, AJ, 155, 48
Winn, J. N. & Fabrycky, D. C. 2015, ARA&A, 53, 409
Wu, Y. & Lithwick, Y. 2013, ApJ, 772, 74

Chapter 5

Results and outlook

This chapter shows and analyzes the results of the simulations listed in table 2.1. First, section 5.1 gives an overview of the flow structure evolution in the models from their initialization up until a thermodynamic equilibrium develops. In section 5.2 the equilibrium solution is then investigated using the M1 simulation as an example. Section 5.3 analyzes in-depth the atmospheric recycling process that causes the thermodynamic equilibrium to emerge, again using the M1 simulation as an example. Then, section 5.4 conducts a parameter study to analyze how the different parameters influence the recycling process and the evolution of the protoplanetary atmosphere. Section 5.5 compares the critical ambient density at different separations, optical depths, and core masses to observed systems to check whether runaway gas accretion could be possible. Finally, section 5.6 hints at what future studies could explore in the context of atmospheric recycling.

The contents of section 5.1 to section 5.4.3 have been published in the articles listed in chapter 4. For the results shown in section 5.4.4 and section 5.5 a manuscript is being prepared and will be submitted within the coming months.

Most plots in this chapter use the Hill radius as a length unit. The Hill radius is the radius of a sphere that has approximately the size of the region where the gravity of the protoplanetary core dominates over the stellar

gravity. It is given by

$$R_{\mathrm{Hill}} = a\sqrt[3]{\frac{M_c}{3M_*}}, \tag{5.1}$$

with the mass of the planetary core, M_c, the mass of the star, M_*, and the orbital separation, a.

Motivated by the recycling timescale jump of more than two orders of magnitude observed in section 5.3, a new "atmospheric" radius, R_{atm}, is introduced. However, instead of calculating this radius using the recycling timescale, it is defined using dynamical considerations:

$$R_{\mathrm{atm}} := \max\left\{ r \,\middle|\, v_\varphi|_{\theta=\pi/2} > \max(v_r, v_\theta) \right\}. \tag{5.2}$$

The atmospheric radius R_{atm} is the maximum radius where the azimuthal velocity component is the largest component of the velocity field in the mid-plane, i.e. where the gas rotates around the core instead of the star. The resulting sphere matches well with the high recycling time region, $t_{\mathrm{rec}} > 100\,\Omega_K^{-1}$, and serves as a good measurement for the extent of the atmosphere.

5.1 Flow structure

Initially, the whole computational domain has a uniform density and the velocity field is given by the circumstellar shearing flow across the planetary core. Figure 5.1 displays the density as well as the velocity field around the planetary core at $t = 0\,\Omega_K^{-1}$. At the orbital position of the planet, the velocity of the gas is zero. Closer to the star (negative x-direction), the velocity of the gas is faster than the orbital velocity of the protoplanet. Further away from the star (positive x-direction), the velocity of the gas is slower than the orbital velocity of the protoplanet. For simulations that include a headwind, the whole velocity field is shifted towards the star, i.e the sign change in the shearing flow no longer occurs at the orbital position of the planet. In this case, the protoplanetary core experiences a gas flow head-on, hence the name headwind.

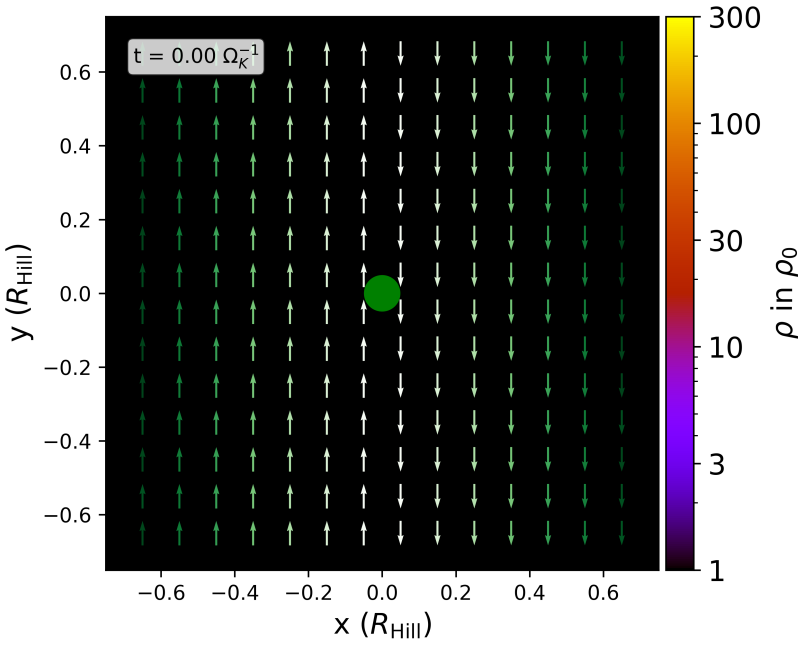

Figure 5.1: Density and flow structure of the M1 simulation at $t = 0\,\Omega_K^{-1}$. The green circle in the center is the planetary core. The color of the arrows is determined by the magnitude of the gas velocity, a darker green indicates a higher velocity. The computational domain is initialized with a uniform density ρ_0 and the shearing flow of the circumstellar disk across the planetary core.

When the simulation is started, the planetary core perturbs the circumstellar shearing flow by accreting gas through its gravitational field. Because of the accretion of gas, the density and temperature increase towards the core. Figure 5.2 shows the 1D averaged density and temperature profiles. Both quantities smoothly transition from the atmospheric flow region (inside R_{atm}) to the circumstellar disk, i.e it is not possible to define an atmosphere using the density or temperature profile.

During this accretion phase additional flow structure develops as shown in figure 5.3 which displays the M1 simulation at $t = 1000\,\Omega_K^{-1}$: An atmospheric region develops where the gas rotates around the protoplanetary core instead of the host star. Horseshoe orbits develop along the orbital direction of the planet. Because the simulations are performed locally at the location of

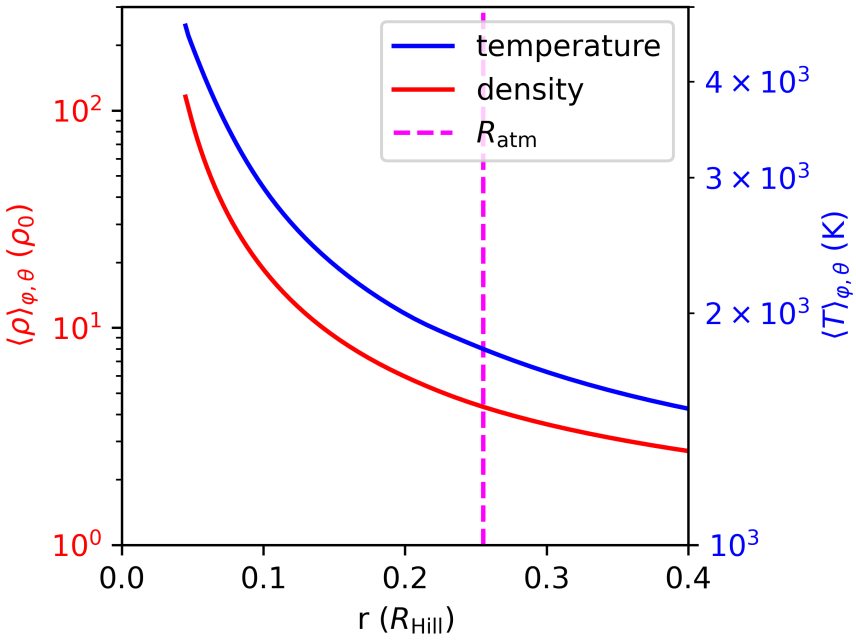

Figure 5.2: 1D averaged density and temperature profile of the M1 simulation at $t = 2000\,\Omega_K^{-1}$. The gravity of the protoplanetary core accretes gas which results in a density and temperature gradient. Both the density and the temperature smoothly transition from the atmosphere inside R_{atm} to the circumstellar disk, i.e. it is not possible to define the atmosphere using the density or temperature.

the planet, the computational domain does not include the entirety of the horseshoe orbits. However, this is not an issue because only the interaction of the horseshoe orbits with the atmosphere is relevant for this work. Further away from the orbit of the protoplanet, the flow transitions back into the circumstellar shearing flow as the gravity of the core becomes less important.

Figure 5.4 shows the 1D averaged energy budget of the gas at $t = 1000\,\Omega_K^{-1}$. The thermal energy (blue) of the gas is more than one order of magnitude higher than its kinetic energy (orange). Hence, the atmosphere is pressure supported and rotates at sub-Keplerian speeds ($\approx 0.5\,v_K$ with respect to the protoplanetary core). Inside the atmospheric radius, R_{atm}, the kinetic energy is significantly higher than outside. This energy is primarily

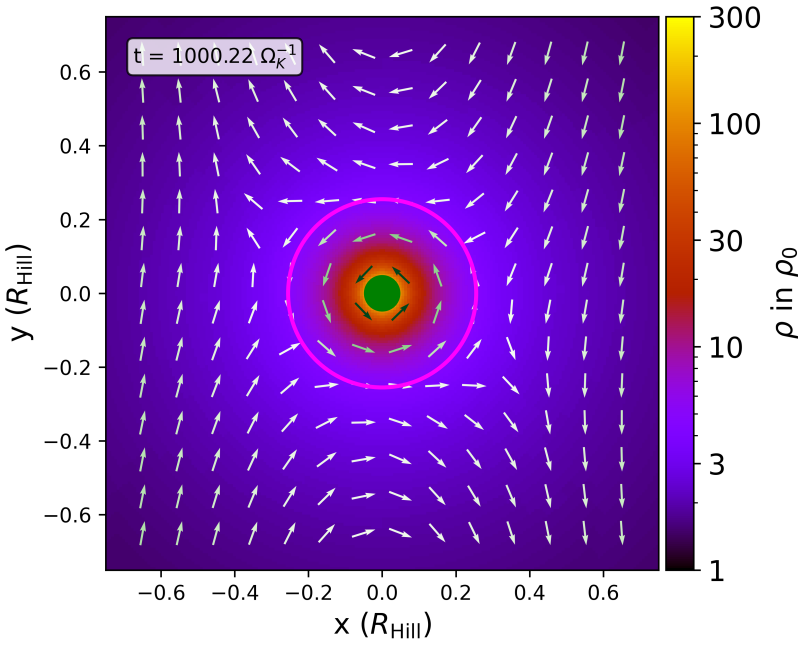

Figure 5.3: Density and flow structure of the M1 simulation at $t = 1000\,\Omega_K^{-1}$. The green circle in the center is the planetary core. The color of the arrows is determined by the magnitude of the gas velocity, a darker green indicates a higher velocity. The magenta circle is the atmospheric radius R_{atm}. Three flow zones emerge: The atmospheric flow around the core, the horseshoe orbits along the orbital direction of the protoplanetary core, and the circumstellar shearing flow further away from the planet's orbit.

in the azimuthal velocity component because the gas is orbiting the protoplanetary core inside R_{atm}. However, in the thermal energy profile, there is no separation between the protoplanetary atmosphere and the circumstellar disk visible. This confirms that the density and temperature profiles smoothly transition from the protoplanetary atmosphere to the circumstellar disk. It is evident that the atmosphere is not an isolated system but has to be studied together with its surrounding disk.

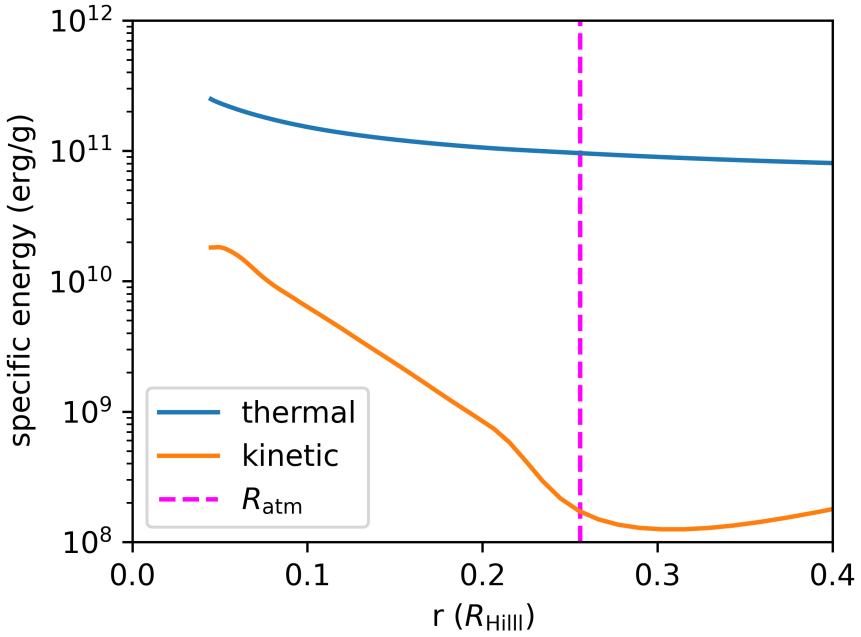

Figure 5.4: 1D averaged energy budget of the gas at $t = 1000\,\Omega_K^{-1}$ for the M1 simulation. The dashed red line is the atmospheric radius R_{atm}. The thermal energy of the atmosphere is more than one order of magnitude higher than the kinetic energy. Inside R_{atm} the kinetic energy increases because of the rotation around the core.

5.2 Thermodynamic equilibrium

When comparing a 3D simulation to an otherwise identical 1D simulation, one finds significant differences in their evolution. Figure 5.5 compares the mass evolution inside the Hill sphere for the M1 and the M1-1D setup, which only differ in their dimensionality. While the 3D simulation eventually stops accreting additional material, the 1D simulation continues to accrete gas. Because there is no external heating source added to the simulations, the 1D simulation will eventually approach the isothermal solution through radiative cooling where the atmosphere has the same temperature as the surrounding disk. In 3D, on the other hand, an additional mechanism is present: Atmospheric recycling. Atmospheric recycling replaces low entropy (cooled) atmospheric gas with high entropy circumstellar gas. Thereby providing the

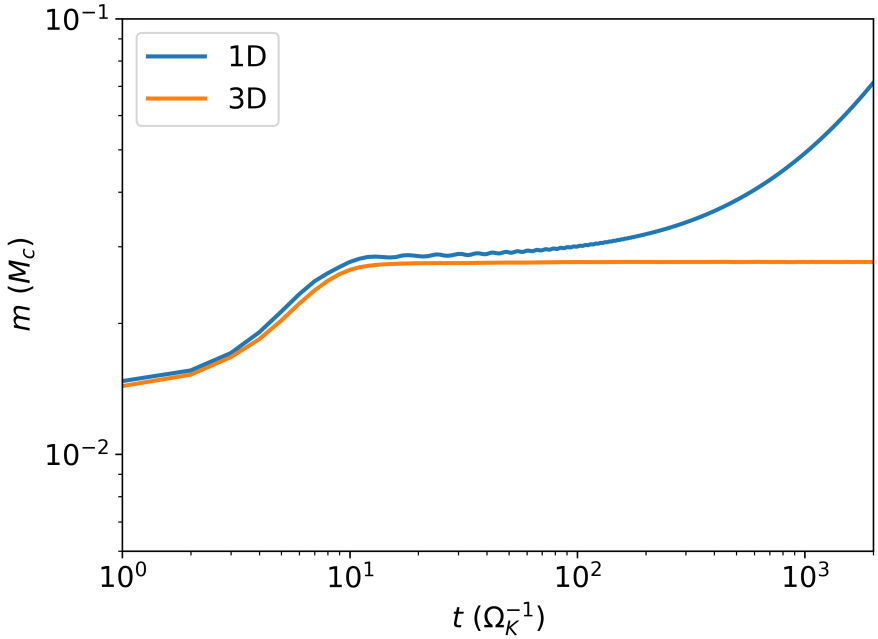

Figure 5.5: Mass evolution comparison of a 3D simulation to an otherwise identical 1D simulation. The 3D simulation eventually stops accreting gas while the 1D simulation does not. In 3D radiative cooling is fully compensated by atmospheric recycling which is geometrically not possible in a single dimension. A thermodynamic equilibrium develops in 3D.

atmosphere with energy and thus heating it without changing its mass. In 1D recycling is not possible for geometric reasons. Because there is only a single direction, gas cannot be replaced, i.e be accreted and removed at the same time. Interestingly, atmospheric recycling is also not possible in 2D. Here, after the initial accretion phase, a separatrix can be found that fully isolates the atmosphere from its surroundings (Ormel et al., 2015a). Atmospheric recycling is therefore a 3D exclusive effect.

In Figure 5.6 the cumulative mass (blue) and the mass fluxes (red and orange) are displayed. The in- and outflux through each shell per Ω_K^{-1} is approximately one order of magnitude lower than the cumulative mass. Considering that Ω_K^{-1} at 0.1 au is very short compared to the disk lifetime, this is a relatively high mass flux. However, when the net mass flux rate is compared

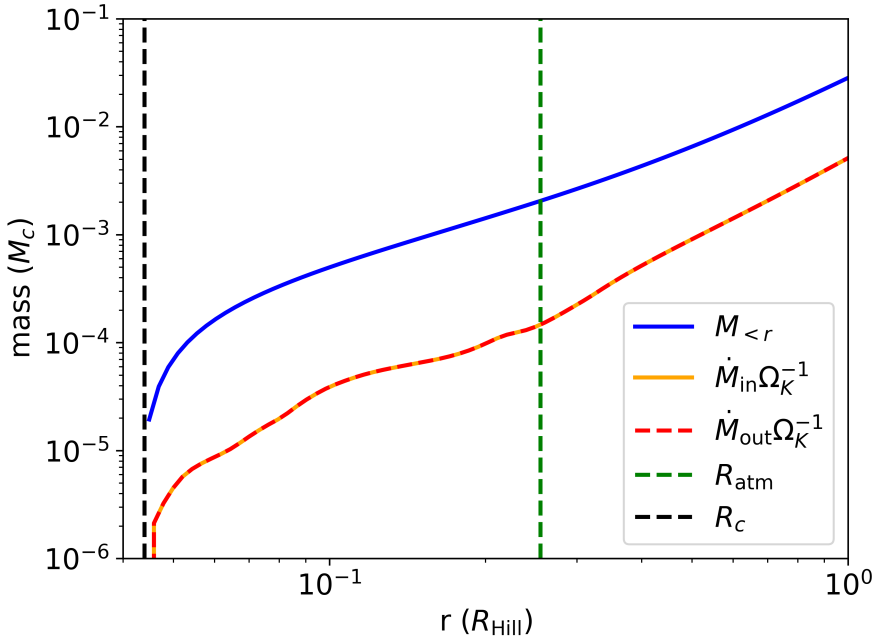

Figure 5.6: 1D averaged mass and mass flux for the M1 simulation. The blue curve is the cumulative mass $M_{<r}$ from the inner boundary R_c up to r. The orange and red curves are the mass in- and outflow across the shell per Ω_K^{-1}. Compared to cumulative mass, the net mass flow across a shell vanishes everywhere, i.e. the mass of the atmosphere is constant in time. The mass flow only vanishes at $r = R_c$. Hence, all layers of the atmosphere experience recycling.

to the cumulative mass, one finds that it effectively vanishes. Therefore, there is a high mass exchange between shells but no net mass gain of the atmosphere, i.e no further accretion. However, this high mass flux does not necessarily mean a high recycling rate. For example, if the gas orbits the core on an elliptical orbit, it would move across shells on very short timescales even without any recycling. To measure the recycling time correctly, it is therefore necessary to use a more sophisticated method utilizing for example tracers. This analysis is performed in the next section 5.3.

Figure 5.7 shows the evolution of the 1D averaged entropy of the M1 simulation. After $\sim 300\,\Omega_K^{-1}$ the entropy of the atmosphere stops decreasing. The atmosphere is then in a thermodynamic equilibrium where radiative

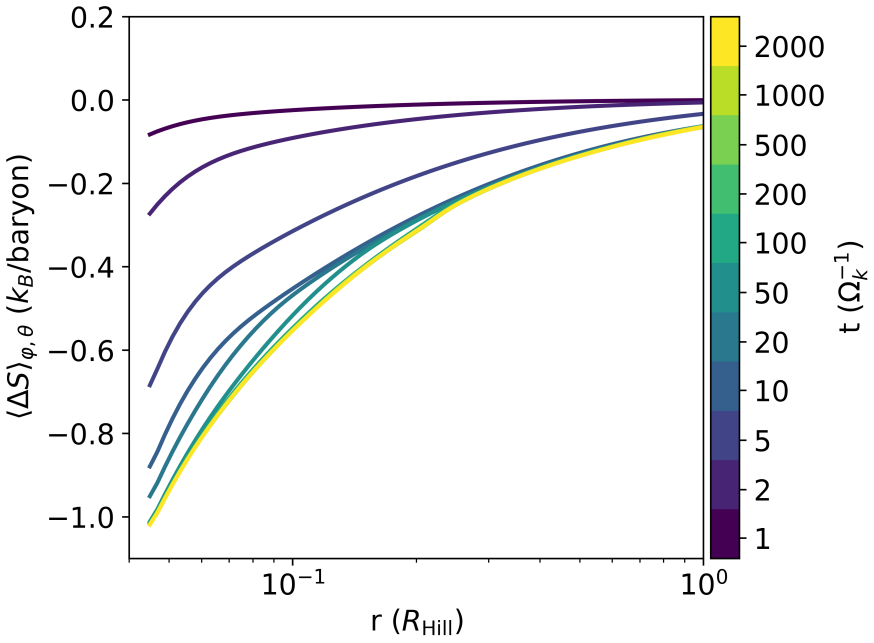

Figure 5.7: Evolution of the 1D averaged entropy for the M1 simulation. After $\sim 300\,\Omega_K^{-1}$ the entropy of the atmosphere stops decreasing. Radiative cooling is then fully counteracted by atmospheric recycling and the atmosphere enters a thermodynamic equilibrium.

cooling is fully compensated by atmospheric recycling. This already suggests that the recycling timescale is of the order $\sim 100\,\Omega_K^{-1}$. Similar to the thermal energy from figure 5.4, the entropy has no sharp gradient between the protoplanetary atmosphere and the circumstellar disk.

5.3 Atmospheric recycling

In the previous section, it was shown that in 3D the atmosphere eventually enters a thermodynamic equilibrium where radiative cooling is fully compensated by entropy advection. In this section, to analyze the recycling process, tracer particles and tracer fluids are utilized once the simulation reached a thermodynamic equilibrium. Because the particle integrator implemented in chapter 3 requires a velocity field that is constant in time, it cannot be used

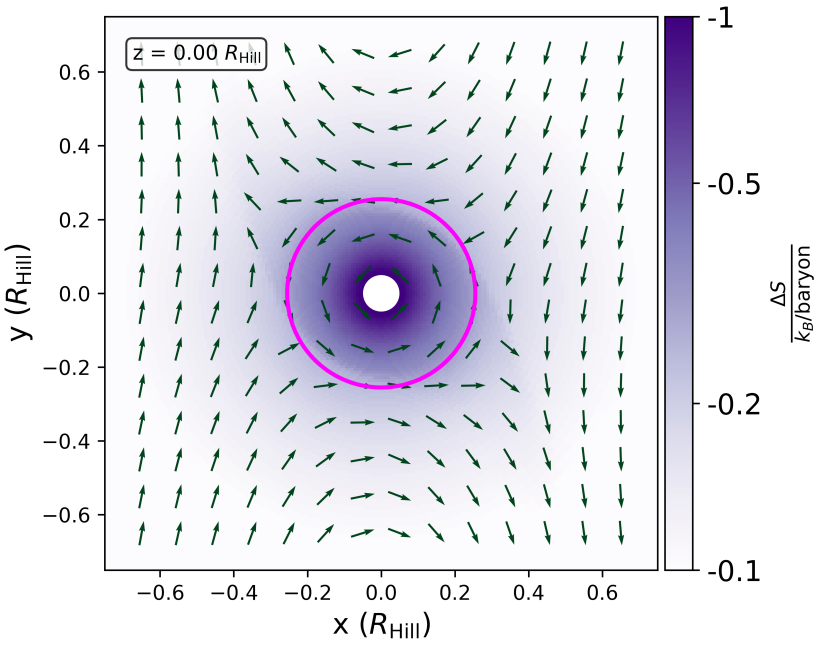

Figure 5.8: Entropy in the midplane of the M1 simulation after a thermodynamic equilibrium has developed. The entropy is measured as the difference to the boundary entropy. The magenta circle is the atmospheric radius R_{atm}. The atmosphere has lower entropy than the surrounding circumstellar disk because of radiative cooling. Low entropy atmospheric gas leaves the atmosphere through the horseshoe orbits and is replaced with high entropy circumstellar gas.

when the velocity field of the atmosphere continues to change significantly after a thermodynamic equilibrium is reached. In this case, tracer fluid is used that is evolved during the simulation as explained in section 2.4.2.

In figure 5.8 the entropy in the midplane is displayed. The atmosphere is cooling radiatively and has thus a lower entropy than the circumstellar disk. However, through the recycling flow, high entropy circumstellar gas replaces low entropy atmospheric gas. Figure 5.9 shows the recycling time of the M1 simulation measured using more than 500 million tracer particles. The tracer particles measure the time the gas has spent inside the Hill sphere, i.e. it measures on what timescale it is replaced with high entropy circumstellar gas outside of the Hill sphere (see section 2.4.1 for details). There

is a strong recycling time gradient at R_{atm} with a difference of more than two orders of magnitude. Inside R_{atm} the gas is recycled on timescales of $\sim 300\,\Omega_K^{-1}$ while the gas outside only spends as little time as $1\,\Omega_K^{-1}$ inside the Hill sphere. Therefore, unlike the density and temperature profiles that smoothly transition between the atmospheric and circumstellar regions, the recycling timescale allows for a clear distinction between the atmosphere and the disk. The midplane view shows how "old" gas is slowly removed through the horseshoe orbits and replaced with fresh circumstellar gas. Additionally, the front and side views show that gas from the circumstellar disk is also accreted through the vertical direction. This inflow appears to squish the atmosphere in the vertical direction. The atmosphere is significantly more elongated in the front view compared to the side view. This is because of the tidal forces exerted by the star.

Figure 5.10 also performs an analysis of the recycling timescale but with tracer fluid instead. After a thermodynamic equilibrium is reached, the whole Hill sphere is filled with tracer fluid. The simulation is then continued and the tracer fluid is advected with the same fluxes as the density, i.e. the tracer fluid tracks the flow of mass (see section 2.4.2). Most of the Hill sphere is cleared of the tracer fluid within only a few Ω_K^{-1}. After $100\,\Omega_K^{-1}$ (top left panel), the atmosphere and the parts of the horseshoe orbits that transport atmospheric gas away have a tracer fluid concentration that is more than three orders of magnitude higher than in the rest of the Hill sphere. After $200\,\Omega_K^{-1}$ (top right panel), the tracer fluid distribution is the same but the concentration is about one order of magnitude lower than at $t = 100\,\Omega_K^{-1}$. At $t = 200\,\Omega_K^{-1}$ the tracer fluid concentration within R_{atm} drops to approximately 1 % of the initial concentration. This confirms the previous analysis using the tracer particles that the atmosphere recycles primarily through the horseshoe orbits on timescales of $\sim 300\,\Omega_K^{-1}$.

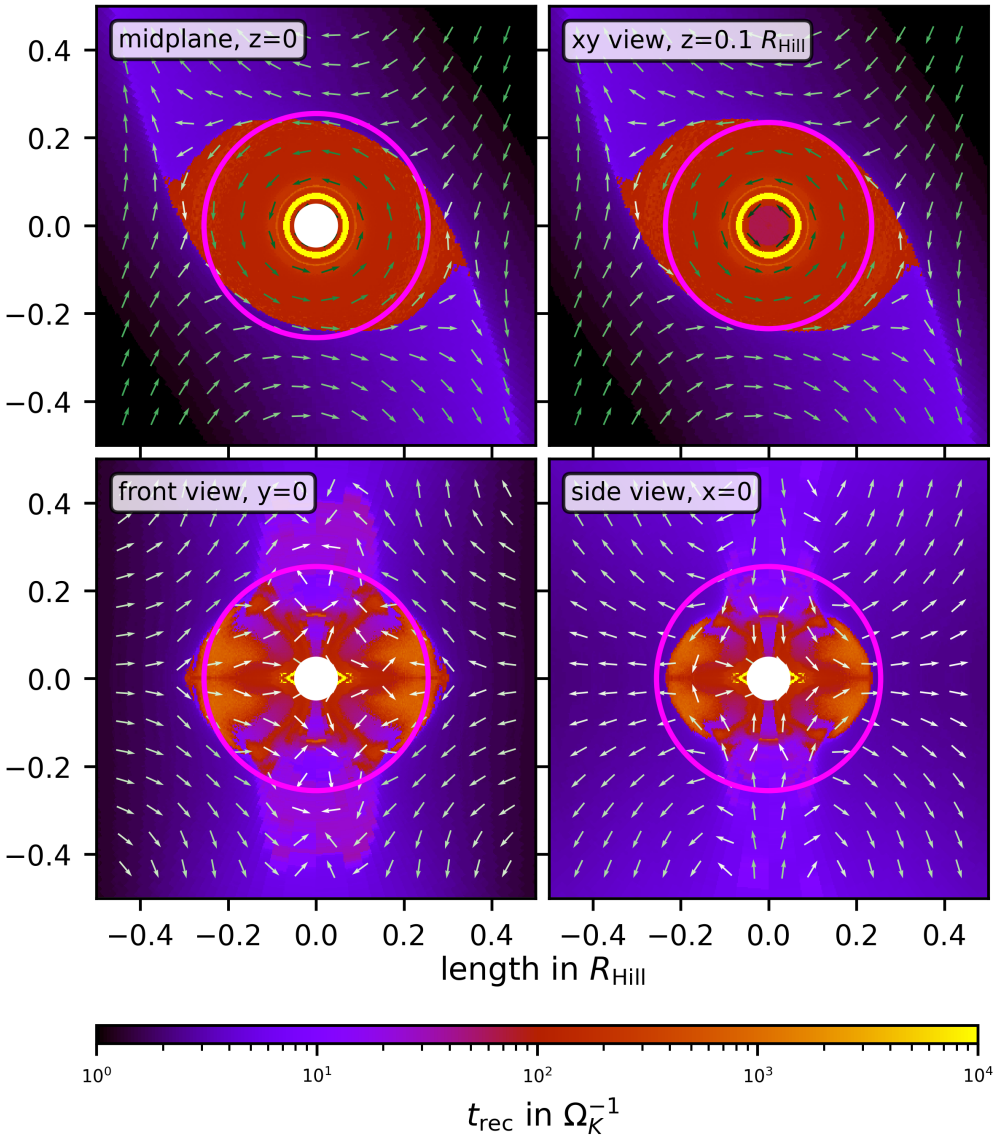

Figure 5.9: Recycling timescale of the M1 simulation measured using more than 500 million tracer particles. The magenta circle is the atmospheric radius, R_{atm}, as described in equation 5.2.

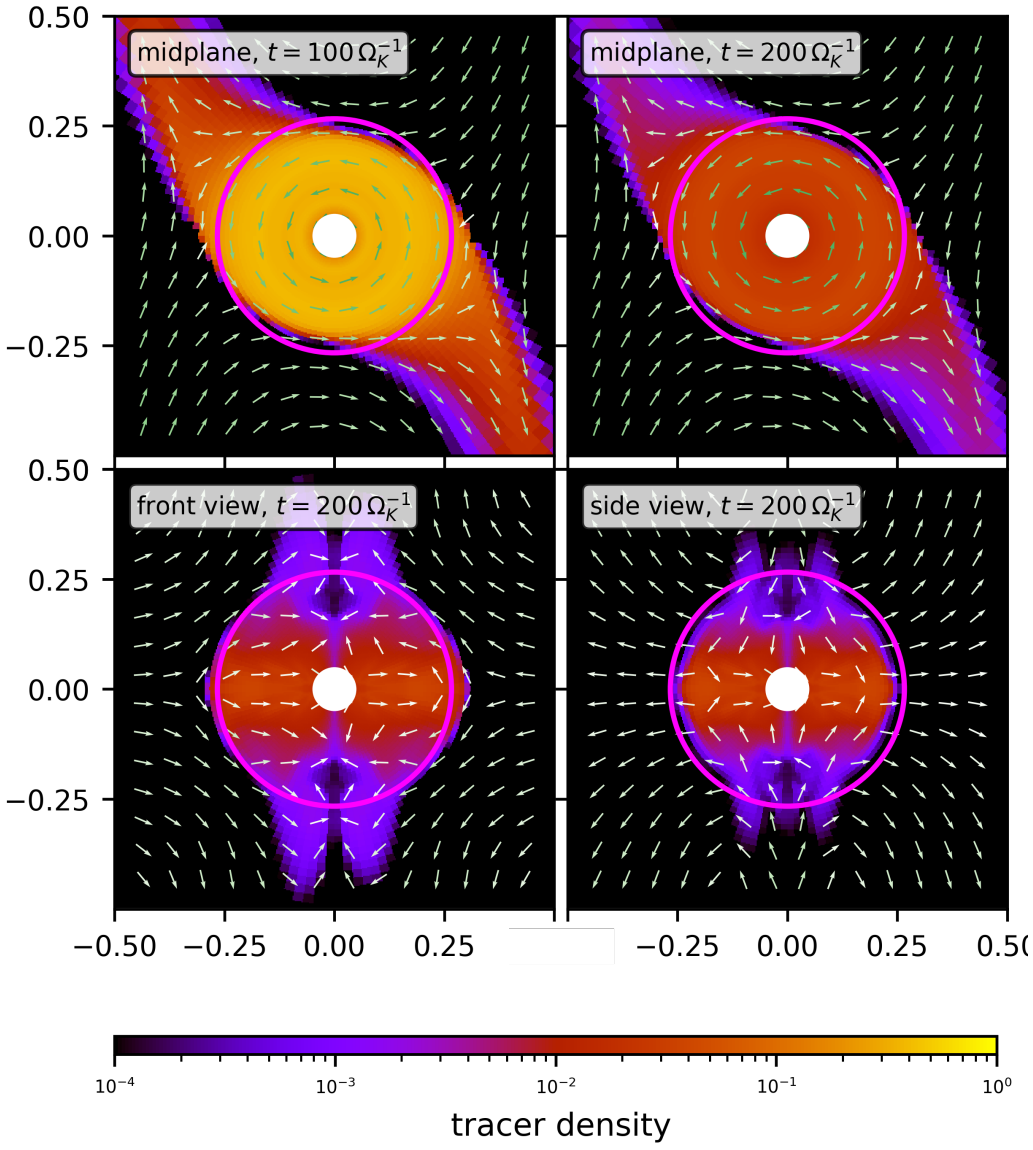

Figure 5.10: Recycling timescale of the M1 simulation measured using tracer fluid. At $t = 0\,\Omega_K^{-1}$ after a thermodynamic equilibrium was reached, the Hill sphere is filled with a tracer density of unity. The simulation is then continued. The magenta circle is the atmospheric radius, R_{atm}, as described in equation 5.2.

5.4 Parameter study

The previous two sections have shown how atmospheric recycling works and that is capable of fully counteracting radiative cooling to establish a thermodynamic equilibrium where the atmosphere is no longer accreting additional gas from the circumstellar disk.

The following sections analyze the influence of various parameters on the recycling timescale and the resulting atmosphere. Section 5.4.1 starts with the potential effects of the so-called headwind which introduces an asymmetry by shifting the horseshoe orbits away from the orbit of the planet towards the star. Then, section 5.4.2 compares different planetary core masses. In section 5.4.3 the effects of the optical depth, i.e. the gas opacity, are investigated. Finally, section 5.4.4 explores the effects of the orbital separation of the protoplanetary core from the host star.

5.4.1 Headwind comparison

Because of the pressure gradient in the circumstellar disk, the stellar gravity is partially compensated and the gas orbits the star at sub-Keplerian speeds. For solid objects like planetary cores, on the other hand, this force is negligible. Therefore, the protoplanet orbits the star faster than the surrounding gas and thus experiences a headwind. The headwind shifts the horseshoe orbits away from the orbit of the planetary core towards the star which introduces an asymmetry to the flow.

Figure 9 in Moldenhauer et al. (2022) displays the resulting tracer fluid concentration at $100\,\Omega_K^{-1}$ after it was injected into the Hill sphere. Compared to the M1 simulation from figure 5.10 the asymmetric flow pattern is clearly visible. Here, the leading horseshoe provides the atmosphere with more fresh circumstellar gas than it removes while the opposite is the case for the other horseshoe. Additionally, the headwind removes the slightly higher recycling time regions that surround the z-axis. However, the size of the atmosphere, R_{atm}, and the density, as well as temperature profiles, remain approximately unchanged. The 1D averaged tracer fluid density at $t = 200\,\Omega_K^{-1}$ displayed in figure 5.11 shows that the simulation that includes the headwind recycles at

a marginally faster rate. Considering that the used headwind Mach number, $\mathcal{M}_{\mathrm{hw}} = 0.1$, is exaggerated by a factor of three (see section 2.1), one can conclude that the headwind has a negligible effect on the recycling timescale and atmospheric mass.

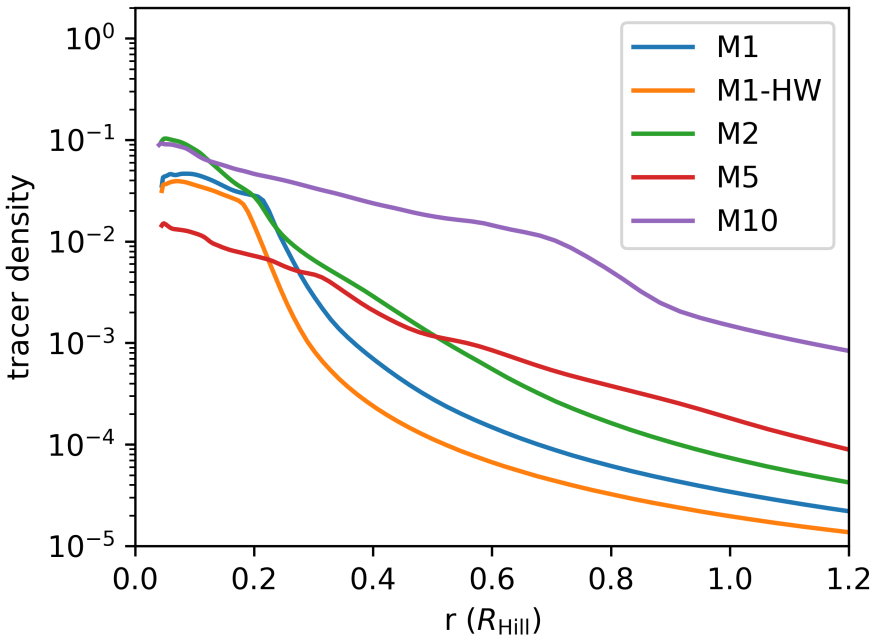

Figure 5.11: 1D averaged tracer fluid density at $t = 200\,\Omega_K^{-1}$ after the tracer fluid was introduced. All simulations are at $a_p = 0.1\,\mathrm{au}$. A lower tracer density indicates a higher recycling efficiency.

5.4.2 Core mass comparison

A more massive core has a stronger gravitational influence on the surrounding circumstellar gas flow. Hence, the Hill sphere becomes larger, the horseshoe orbits widen and the density and temperature gradients become steeper. These effects also affect the recycling of the protoplanetary atmosphere as can be observed in figure 5.11. When comparing the tracer concentration for the M1 (blue) simulation to the one for the M2 (green) simulation, one can see that doubling the core mass results in a longer recycling time. The

inner regions of the M2 simulation have a more than three times higher tracer fluid concentration compared to the M1 simulation at $t = 200\,\Omega_K^{-1}$ after the tracer fluid was introduced. The more massive core retains the gas better and therefore renders the recycling process less efficient.

However, the picture completely changes when comparing the M2 to the M5 (red) simulation. The M5 simulation has an almost 10 times lower tracer fluid concentration in its innermost regions compared to the M2 simulation. This anomaly is explained by the onset of turbulence within the atmosphere at higher core masses. While the M5 and M10 simulations also eventually reach a thermodynamic equilibrium as do the M1 and M2 simulations, they do not have a velocity field that is constant in time in this equilibrium. The velocity field continues to change on timescales much shorter than the recycling timescale. This turbulence enhances atmospheric recycling in two ways: Firstly, it increases mixing at the boundary layer between the atmosphere and the horseshoe orbits, and secondly, it enhances mixing within the atmosphere. When the core mass is further increased to $M_c = 10\,M_{\rm Earth}$ in the M10 simulation, the recycling time increases again.

To conclude, there are two effects that affect the recycling timescale when the core mass is changed: A higher mass core retains the gas better and the recycling timescale becomes longer. When the core mass surpasses a certain threshold (between 2 and $5\,M_{\rm Earth}$), turbulence within the protoplanetary atmosphere starts to occur and the recycling timescale becomes shorter.

5.4.3 Optical depth comparison

Optical depth plays an important role in determining the efficiency of radiative cooling. A lower optical depth results in a higher cooling rate. To study the effects of the optical depth on the atmosphere and to determine whether it affects atmospheric recycling, in this section, the standard simulation M1 is compared to M1-1 and M1+1 which feature a one order of magnitude lower and higher optical depth respectively.

Figure 5.12 compares the 1D averaged temperature profiles of these simulations after a thermodynamic equilibrium was reached. As expected, a lower

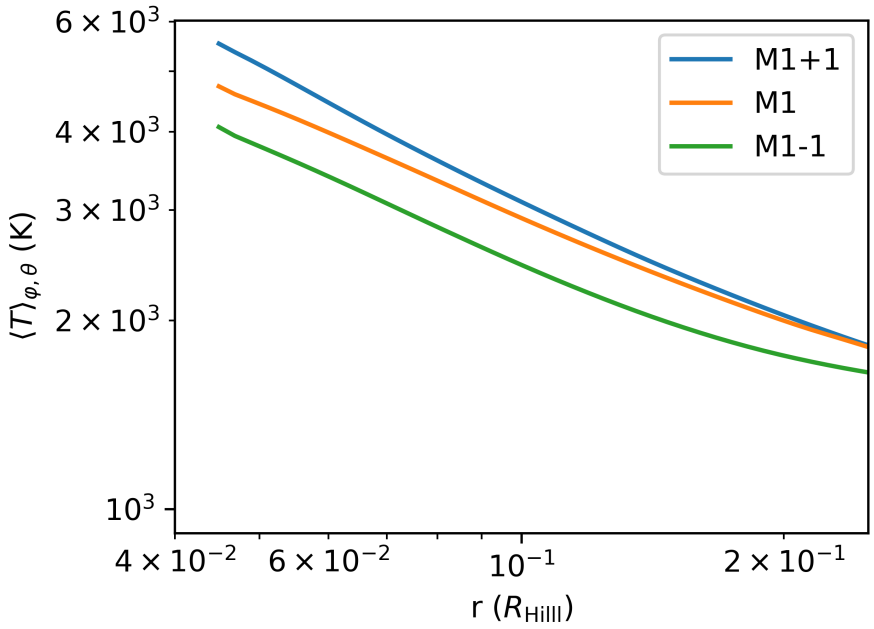

Figure 5.12: 1D averaged temperature profiles for different optical depths. M1 is the standard case. M1+1 and M1-1 have an optical depth that is one order of magnitude higher and lower respectively. Towards the circumstellar disk, the effect of the optical depth diminishes because of the short recycling time there.

optical depth results in a lower equilibrium temperature because of the more efficient cooling. The difference between the simulations is more pronounced in the inner layers. Towards the outer layers, i.e. towards the circumstellar flow, the differences in the temperature profiles diminish. Here, the recycling time is short enough that radiative cooling has little effect on the thermodynamics of the gas. The lower temperatures lead to a denser atmosphere for lower optical depths.

The different temperature and density profiles caused by the difference in cooling also affect the rotational velocity of the atmosphere, shown in figure 5.13. For a lower optical depth, the sign change in the azimuthal velocity occurs at a larger radius. This means that the velocity profile transitions from the atmospheric flow to the circumstellar flow further away from the core,

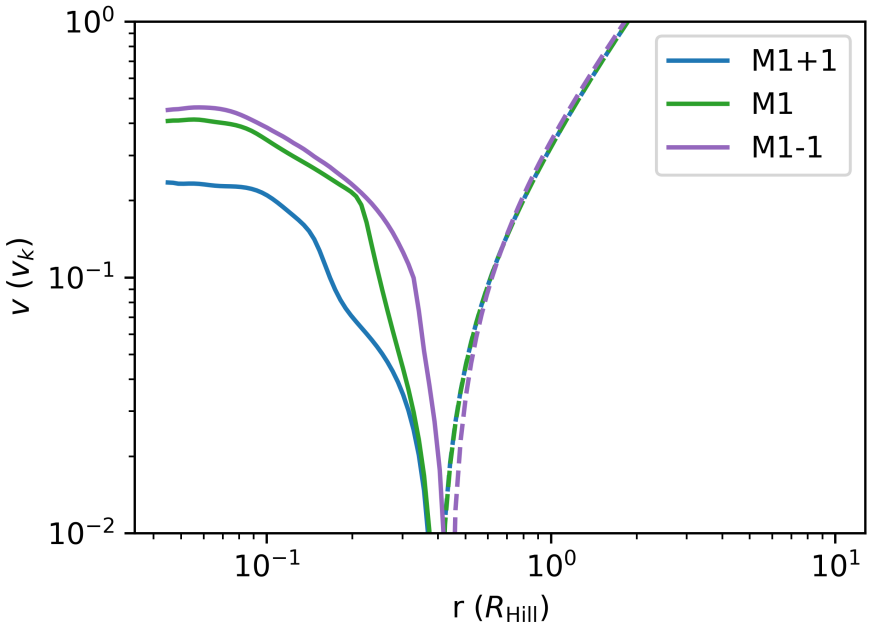

Figure 5.13: 1D averaged azimuthal velocity for different optical depths. M1 is the standard case. M1+1 and M1-1 have an optical depth that is one order of magnitude higher and lower, respectively. A lower optical depth results in a larger and faster rotating atmosphere.

i.e. the atmosphere becomes larger if the opacity is lowered. Additionally, a lower optical depth results in a faster rotating atmosphere. The higher rotational speed can be explained by the conservation of angular momentum as the lower temperature atmosphere contracts more. The larger atmosphere can be explained by an increase in gas pressure which can be seen in figure 5.14. Higher atmospheric pressure can sustain a larger atmosphere. It's important to note that a higher azimuthal velocity and a higher pressure are not mutually exclusive because of the increase in density for lower opacities. For all explored optical depths the atmosphere rotates at significantly sub-Keplerian speeds and is therefore always predominantly pressure supported.

In figure 13 of Moldenhauer et al. (2022), a recycling time analysis using tracer particles is displayed for different optical depths. Here, the change in size of the protoplanetary atmosphere depending on the optical depth can be

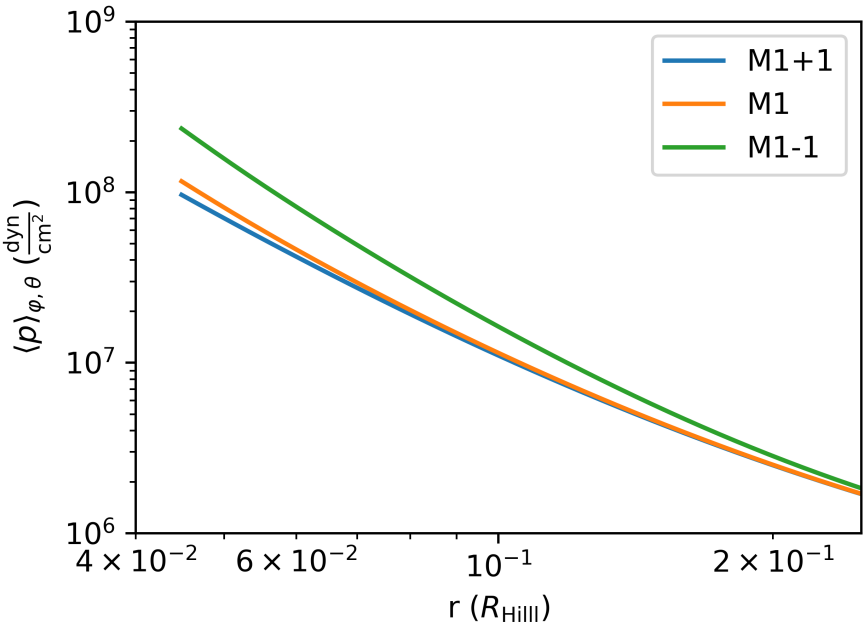

Figure 5.14: 1D averaged pressure profiles for different optical depths. M1 is the standard case. M1+1 and M1-1 have an optical depth that is one order of magnitude higher and lower, respectively. A lower optical depth leads to an increase in pressure which allows for a larger atmosphere to be supported.

seen. However, the recycling timescale is not affected by the optical depth. Additionally, for all simulations, the atmosphere recycles uniformly. There are no layers of different recycling timescales forming.

To conclude, the optical depth of the gas has significant effects on the atmosphere. A lower optical depth leads to a cooler, faster rotating, larger and denser atmosphere. The recycling timescale, on the other hand, is unaffected by the optical depth for the explored parameter space.

5.4.4 Orbital separation

The simulation time required to reach an equilibrium state depends on the dynamical timescale, $\Omega_K^{-1} = \sqrt{a^3/(GM_*)}$. While the dynamical timescale increases with the separation, a, the simulation time step stays constant as it is limited by the size of the inner boundary which is determined by the size

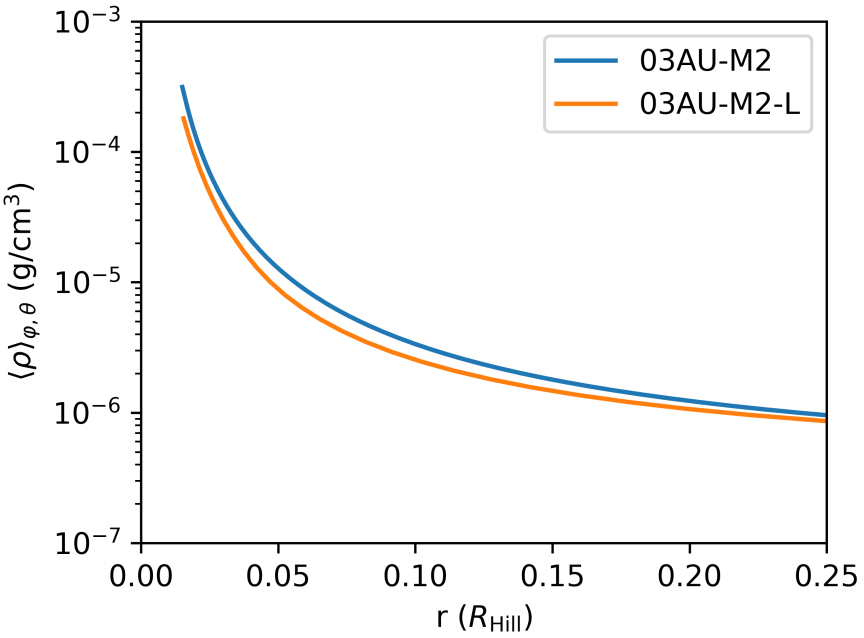

Figure 5.15: 1D averaged density profile for the 03AU-M2 (normal resolution) and 03AU-M2-L (lower resolution) simulations. Both simulations reach a thermodynamic equilibrium. However, the higher resolution results in a denser atmosphere.

of the protoplanetary core. Thus, for larger separations of the planetary core from the host star, the simulations become computationally more expensive. Considering that the simulations at $a = 0.1$ au already take multiple months in real-time to reach a thermodynamic equilibrium, an extensive parameter study at larger separations is only feasible when the resolution is reduced. Figure 5.15 compares the density profile of the 03AU-M2 (normal resolution) to the 03AU-M2-L (lower resolution) simulation. While both simulations reach a thermodynamic equilibrium, their density profiles do not match. A potential explanation for this behavior could be that the boundary between the atmosphere and the disk is more poorly defined in the lower-resolution models. This could lead to more gas being exchanged at that boundary, therefore more atmospheric recycling and thus a less dense atmosphere for the lower-resolution simulation. However, for a qualitative comparison of dif-

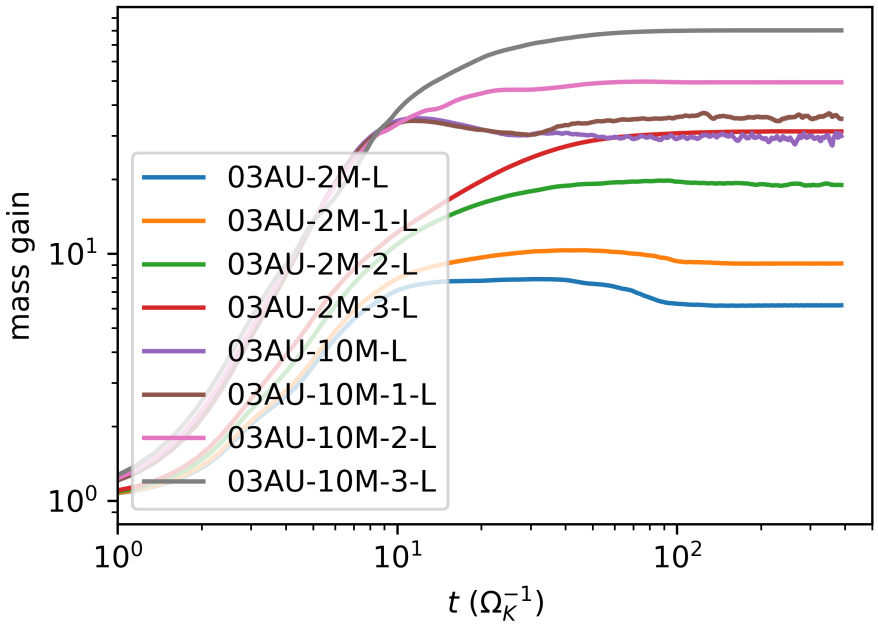

Figure 5.16: Relative mass gain inside the sphere $r < R_{\mathrm{Hill}}/4$ of the simulations with $a_p = 0.3\,\mathrm{au}$.

ferent parameters, the lower resolutions models nevertheless provide important insights. In the future, once computational capabilities have advanced further, these simulations should be repeated at a higher resolution.

Figure 5.16 displays the mass gain in the sphere $r < R_{\mathrm{Hill}}/4$ as a function of time for the simulations at 0.3 au. All simulations at $a_p = 0.3\,\mathrm{au}$ converge to a thermodynamic equilibrium where there is no more mass accreted by the protoplanetary core. As expected, a higher core mass or a lower optical depth and therefore more efficient cooling lead to a higher mass gain. Interestingly, the simulations at $a_p = 0.3\,\mathrm{au}$ take about one order of magnitude longer in units of Ω_K^{-1} to reach a thermodynamic equilibrium compared to the M1 simulation at $a_p = 0.1\,\mathrm{au}$ shown in figure 5.5. This is despite the fact that Ω_K^{-1} increases with a_p which suggests that the recycling timescale increases more strongly than the dynamical timescale with the orbital separation. The simulations with a core mass of $2\,M_{\mathrm{Earth}}$ have an atmospheric radius of $R_{\mathrm{atm}} \approx 0.4\,R_{\mathrm{Hill}}$ while for a core mass of $10\,M_{\mathrm{Earth}}$ the atmospheric radius increases

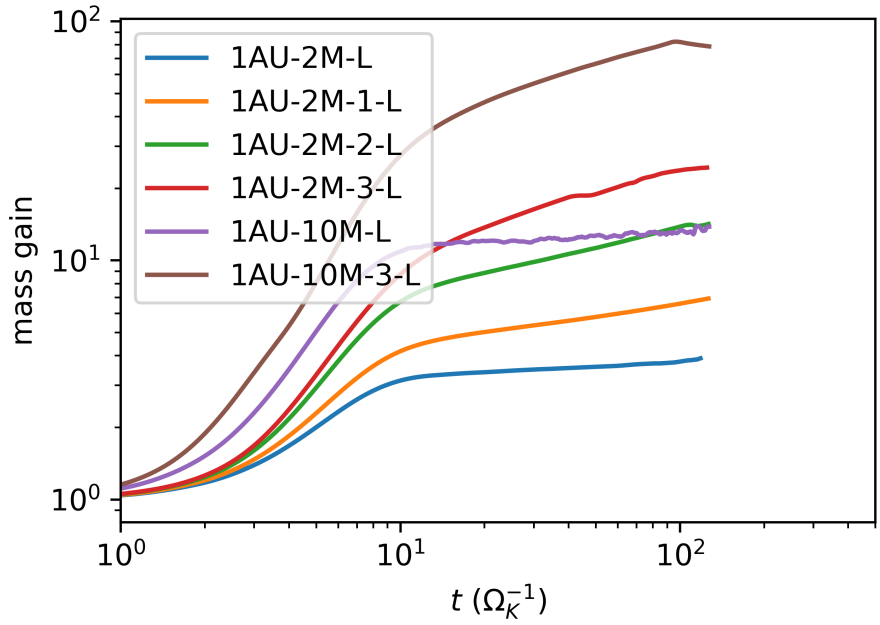

Figure 5.17: Relative mass gain inside the sphere $r < R_{\mathrm{Hill}}/4$ of the simulations with $a_p = 1\,\mathrm{au}$.

to $R_{\mathrm{atm}} \approx 0.4\,R_{\mathrm{Hill}}$.

The mass gain in the sphere $r < R_{\mathrm{Hill}}/4$ as a function of time for the simulations at 1 au is shown in figure 5.17. First, one can observe that the simulations did not yet reach a thermodynamic equilibrium. However, the preliminary results suggest that the previously observed trend continues and the simulations at 1 au take more time to reach an equilibrium even when measured in units of the longer dynamical timescale. The mass gain at 0.1 au is slightly lower compared to the mass gain at 0.3 au but is still growing as the atmosphere continues to accrete circumstellar gas. At an orbital separation of 1 au the simulations with a core mass of $2\,M_{\mathrm{Earth}}$ have an atmospheric radius of $R_{\mathrm{atm}} \approx 0.3\,R_{\mathrm{Hill}}$ while for a core mass of $10\,M_{\mathrm{Earth}}$ the atmospheric radius increases to $R_{\mathrm{atm}} \approx 0.7\,R_{\mathrm{Hill}}$. However, considering the cell size of approximately $0.05\,R_{\mathrm{Hill}}$ at the boundary between the atmosphere and the disk and the fact that the atmosphere is still growing, one cannot conclude with certainty that the atmospheric radius is smaller than at 0.3 au.

The orbital separation affects two relevant parameters: The dynamical timescale, Ω_K^{-1}, and the ambient temperature of the circumstellar disk, T_0. To analyze the effect of the ambient temperature, the 03AU-M2-L-T and 03AU-M10-L-T simulations use an ambient temperature of 1000 K which is roughly 50 % higher than the ambient temperature at 0.3 au calculated from the temperature profile from equation 2.7 which used by 03AU-M2-L and 03AU-M10-L. This increased ambient temperature leads to a 25 % lower mass gain for $M_c = 2\,M_{\mathrm{Earth}}$ and a 50 % lower mass gain for $M_c = 10\,M_{\mathrm{Earth}}$. Hence, the ambient temperature alone is a considerable factor for the atmospheric mass gain.

5.5 Runaway gas accretion

For an atmosphere to eventually undergo runaway gas accretion, the atmospheric mass has to be comparable to the core mass. In that case, self-gravity starts to become important and the accretion of gas from the protoplanetary disk is accelerated by the mass of the atmosphere itself. If there is enough gas available to be accreted by the protoplanet, the planet could then potentially become a gas giant. It is therefore insightful to analyze whether the performed simulations could accrete a massive enough envelope for this process to be possible.

The atmospheric mass is given by

$$M_{\mathrm{atm}} = \int\limits_{r<R_{\mathrm{atm}}} \rho(r)\,\mathrm{d}V, \tag{5.3}$$

where R_{atm} is the atmospheric radius as defined in equation 5.2. However, as explained in section 2.1, the results of the simulations only depend on the product $\rho_0\kappa$. The initial density, ρ_0 is therefore a free parameter if the opacity, κ, is changed accordingly. The initial density, ρ_0, directly affects the measured atmospheric mass, M_{atm}. Consequently, it is possible to rescale the simulations to an arbitrary atmospheric mass by changing ρ_0 and κ such that the product $\rho_0\kappa$ remains the same. By setting the atmospheric mass

to a value where runaway gas accretion starts to become a possible scenario and comparing the calculated required initial density and opacity to observed disk conditions, one can predict whether the evolution of a protoplanet in a given simulation could potentially lead to the formation of a gas giant.

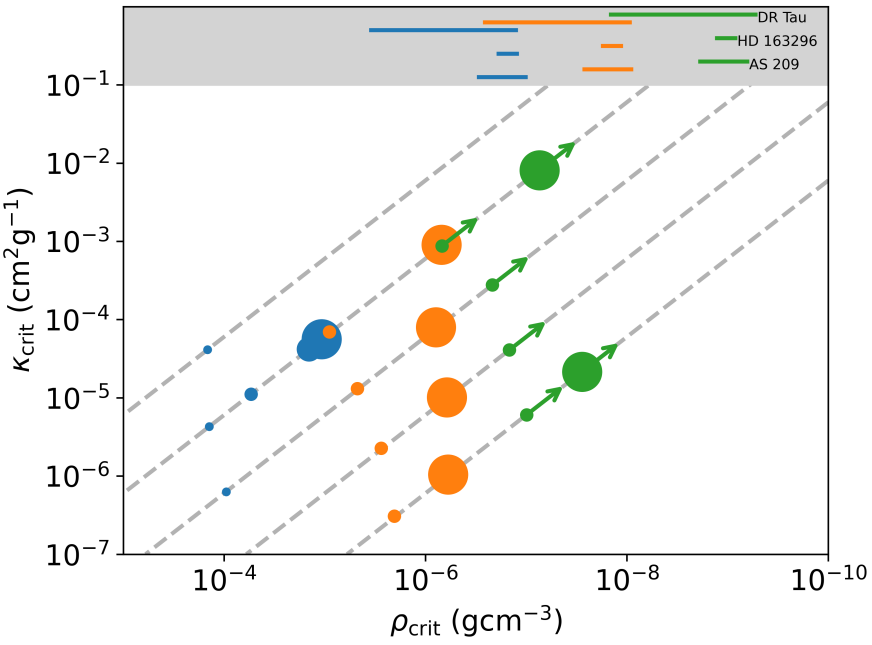

Figure 5.18: Critical gas opacity and disk ambient density for which the atmospheric mass reaches 10 % of the core mass. The dot sizes indicate the core mass (1,2,5 and 10 M_{Earth}). The color indicates the separation to the host star: blue for 0.1 au, orange for 0.3 au and green for 1 au. The dashed grey lines are $\kappa\rho$ isolines. The green arrows indicate that the simulations with a stellar separation of 1 au continue to accrete gas and therefore continue to move on their respective isoline. On the top of the figure, the disk densities with the error range of three observed systems are plotted at the investigated separations.

For this analysis, the critical atmospheric mass, $M_{\mathrm{atm,crit}}$, is set to 10 % of the core mass, M_c. The critical initial density ρ_{crit} and the critical opacity,

κ_{crit} are then given by

$$M_{\text{atm,crit}} \stackrel{!}{=} 0.1\, M_{\text{c}}, \tag{5.4}$$

$$\Rightarrow \rho_{\text{crit}} = \frac{0.1\, M_{\text{c}}}{M_{\text{atm}}} \rho_0, \tag{5.5}$$

$$\kappa_{\text{crit}} = \frac{\rho_0 \kappa}{\rho_{\text{crit}}}. \tag{5.6}$$

For a comparison with observed parameters, three systems are used: AS 209, DR Tau (Tazzari et al., 2016) and HD 163296 (Guidi et al., 2016). The gas surface densities which were calculated from the integrated dust emissions were compiled by Powell et al. (2019) and given in the form,

$$\Sigma_g(r) = \Sigma_0 \left(\frac{r}{r_c}\right)^{-\gamma} \exp\left(\left(\frac{r}{r_c}\right)^{2-\gamma}\right), \tag{5.7}$$

with the parameters listed in table 5.1. The volumetric gas density in the midplane is calculated from the surface density using

$$\rho_g(r) = \frac{\Sigma_g(r)}{\sqrt{2\pi} H}, \tag{5.8}$$

where H is the disk height from equation 2.8. The uncertainty that is given in table 5.1 only considers the error because of the disk age. However, including other sources of error, the total error can be several orders of magnitude (Birnstiel et al., 2012). Nevertheless, these disk densities allow for a comparison with the calculated critical densities from the simulations.

Name	Age in Myr	Disk Mass in $M_\odot$	Uncertainty in $M_\odot$	Σ_0 in gcm^{-2}	r_c in au	γ
AS 209	1.6	0.24	-0.165	44	98	0.91
HD 163296	5	0.21	-0.084	29	119	0.88
DR Tau	1	0.09	$-0.081/+0.18$	315	20	1.07

Table 5.1: Reference systems. The disk mass uncertainty is calculated from the disk age.

Figure 5.18 shows the critical density and opacity for different simulations

and displays the gas density in AS 209, DR Tau, and HD 163296 for comparison. The mass of the core is indicated by the dot size and the separation determines the color of the plotted dot. While a protoplanet accretes gas and its atmosphere grows in mass, their respective simulation moves on its $\rho_0\kappa$-isoline from left to right. The simulations with a separation of $a_p = 1\,\mathrm{au}$ (green) did not reach a thermodynamic equilibrium and continue to accrete gas as indicated by the green arrows.

A higher core mass results in a denser and larger atmosphere and thus a lower critical density and higher critical opacity, i.e. runaway gas accretion becomes more likely for the same disk conditions. The effect of the core mass is comparable in magnitude at different separations. However, for a higher value of $\rho_0\kappa$, i.e. a lower optical depth, the core mass has a stronger effect on the critical density.

For a larger separation, the protoplanet accretes a larger atmosphere with a stronger density gradient. Therefore, the critical density decreases when the orbital separation is increased. However, at the same time, the ambient circumstellar disk density also decreases for larger separations. The results imply that at none of the investigated separations runaway gas accretion is possible. However, because the simulations at 1 au did not yet reach a thermodynamic equilibrium and the lower resolution used for the simulation at 0.3 au and 1 au results in a flatter density profile, the results at these orbital separations are not conclusive. Nevertheless, it is evident that atmospheric recycling significantly decreases the possibility for runaway gas accretion to occur.

5.6 Summary and outlook

This thesis has shown that atmospheric recycling at small orbital separations is a significant effect. In a 1D simulation, a protoplanetary core accretes an orders of magnitude more massive atmosphere compared to an otherwise identical 3D simulation. Therefore, the work presented here has shown that when modeling the formation of close-in planets, it is crucial to take atmospheric recycling into account.

The in-depth analysis of the recycling process conducted within the scope of this thesis has demonstrated how the gas of the atmosphere is recycled with circumstellar gas and on what timescales. Using a quantitative calculation that takes observed disk densities into account it was shown that at close-in separations in-situ gas giant formation is unlikely. This result agrees with current observations that found super-Earths and mini-Neptunes in great abundance even when taking observational biases into account.

Future work on the formation of close-in planets should focus on a higher resolution for larger orbital separations and explore global effects. While the conducted simulation at $a_p = 0.1\,\mathrm{au}$ are converged, the lower resolution models at 0.3 au and 1 au are not. A limitation of the local simulations conducted in the scope of this thesis is that they ignore alterations of the circumstellar disk by the planet. However, this is a good approximation for lower mass protoplanetary cores like the ones explored here. Future studies should include the whole circumstellar disk in their simulation domain, especially when exploring higher core masses or when taking the eventual dispersal of the disk into account. Additionally, when the atmospheric mass reaches approximately 10 % of the core mass, the inclusion of self-gravity should be considered.

Acknowledgements

First, I want to thank my supervisors PD Dr. Rolf Kuiper and Prof. Dr. Willy Kley. Both have always supported me in my ideas, gave valuable advice, and were always eager to maintain a friendly and fun atmosphere. I couldn't have hoped for better supervisors. Sadly, Willy passed away shortly before the completion of this thesis and could therefore not witness the final step of my scientific education. I am also grateful to Prof. Dr. Klaus Werner who stepped in for Willy on short notice and Heike Fricke who was of great help with all bureaucratic matters.

I would also like to thank all my colleagues from the Computational Physics and the Emmy Noether Research Group on Massive Star Formation with whom I have had countless interesting scientific and non-scientific discussions. My special thanks go to my office mates Lucas Jordan and Thomas Rometsch for the great atmosphere in our office and our numerous discussions about economics and politics. I will miss my time at the institute.

Moreover, I would like to thank the rest of the team of the virtual conferencing software sci.an, Oliver Völkel and Jacob Isbell. I'm looking forward to the further development of our platform.

Additionally, I would like to thank the German government and taxpayers for providing me with the funding for my thesis through the DFG grant no. KU 2849/6. Furthermore, I was provided with all the computational resources that I could have wished for through the High-Performance Computing infrastructure of the state of Baden-Württemberg (bwHPC).

Finally, I would like to thank my parents who have always supported me unconditionally and enabled me in pursuing my goals.

Bibliography

Mohamad Ali-Dib, Andrew Cumming, and Douglas N. C. Lin. The imprint of the protoplanetary disc in the accretion of super-Earth envelopes. *MNRAS*, 494(2):2440–2448, April 2020. doi: 10.1093/mnras/staa914.

Yann Alibert, Olivier Mousis, Christoph Mordasini, and Willy Benz. New Jupiter and Saturn Formation Models Meet Observations. *ApJ*, 626(1): L57–L60, June 2005. doi: 10.1086/431325.

Sean M. Andrews, D. J. Wilner, A. M. Hughes, Chunhua Qi, and C. P. Dullemond. Protoplanetary Disk Structures in Ophiuchus. *ApJ*, 700(2): 1502–1523, August 2009. doi: 10.1088/0004-637X/700/2/1502.

Sean M. Andrews, D. J. Wilner, A. M. Hughes, Chunhua Qi, and C. P. Dullemond. Protoplanetary Disk Structures in Ophiuchus. II. Extension to Fainter Sources. *ApJ*, 723(2):1241–1254, November 2010. doi: 10.1088/0004-637X/723/2/1241.

Sean M. Andrews, Jane Huang, Laura M. Pérez, Andrea Isella, Cornelis P. Dullemond, Nicolás T. Kurtovic, Viviana V. Guzmán, John M. Carpenter, David J. Wilner, Shangjia Zhang, Zhaohuan Zhu, Tilman Birnstiel, Xue-Ning Bai, Myriam Benisty, A. Meredith Hughes, Karin I. Öberg, and Luca Ricci. The Disk Substructures at High Angular Resolution Project (DSHARP). I. Motivation, Sample, Calibration, and Overview. *ApJ*, 869 (2):L41, December 2018. doi: 10.3847/2041-8213/aaf741.

S. Ataiee, C. Baruteau, Y. Alibert, and W. Benz. How much does turbulence

change the pebble isolation mass for planet formation? *A&A*, 615:A110, July 2018. doi: 10.1051/0004-6361/201732026.

M. J. Baines, I. P. Williams, and A. S. Asebiomo. Resistance to the motion of a small sphere moving through a gas. *MNRAS*, 130:63, January 1965. doi: 10.1093/mnras/130.1.63.

Konstantin Batygin, Peter H. Bodenheimer, and Gregory P. Laughlin. In Situ Formation and Dynamical Evolution of Hot Jupiter Systems. *ApJ*, 829(2):114, October 2016. doi: 10.3847/0004-637X/829/2/114.

H. A. Bethe and C. L. Critchfield. The Formation of Deuterons by Proton Combination. *Physical Review*, 54(4):248–254, August 1938. doi: 10.1103/PhysRev.54.248.

William Béthune and Roman Rafikov. Envelopes of embedded super-Earths II. Three-dimensional isothermal simulations. *MNRAS*, page 1811, Jul 2019. doi: 10.1093/mnras/stz1870.

T. Birnstiel, H. Klahr, and B. Ercolano. A simple model for the evolution of the dust population in protoplanetary disks. *A&A*, 539:A148, March 2012. doi: 10.1051/0004-6361/201118136.

Bertram Bitsch, Alessandro Morbidelli, Anders Johansen, Elena Lega, Michiel Lambrechts, and Aurélien Crida. Pebble-isolation mass: Scaling law and implications for the formation of super-Earths and gas giants. *A&A*, 612:A30, April 2018. doi: 10.1051/0004-6361/201731931.

A. G. W. Cameron. Physics of the Primitive Solar Accretion Disk. *Moon and Planets*, 18(1):5–40, February 1978. doi: 10.1007/BF00896696.

Yayaati Chachan, Eve J. Lee, and Heather A. Knutson. Radial Gradients in Dust-to-gas Ratio Lead to Preferred Region for Giant Planet Formation. *ApJ*, 919(1):63, September 2021. doi: 10.3847/1538-4357/ac0bb6.

E. Chiang and G. Laughlin. The minimum-mass extrasolar nebula: in situ formation of close-in super-Earths. *MNRAS*, 431:3444–3455, June 2013. doi: 10.1093/mnras/stt424.

N. P. Cimerman, R. Kuiper, and C. W. Ormel. Hydrodynamics of embedded planets' first atmospheres - III. The role of radiation transport for super-Earth planets. *mnras*, 471:4662–4676, November 2017. doi: 10.1093/mnras/stx1924.

Andrew Cumming, R. Paul Butler, Geoffrey W. Marcy, Steven S. Vogt, Jason T. Wright, and Debra A. Fischer. The Keck Planet Search: Detectability and the Minimum Mass and Orbital Period Distribution of Extrasolar Planets. *PASP*, 120(867):531, May 2008. doi: 10.1086/588487.

A. S. Eddington. The internal constitution of the stars. *The Observatory*, 43:341–358, October 1920.

Alexandre Emsenhuber, Christoph Mordasini, Remo Burn, Yann Alibert, Willy Benz, and Erik Asphaug. The New Generation Planetary Population Synthesis (NGPPS). I. Bern global model of planet formation and evolution, model tests, and emerging planetary systems. *arXiv e-prints*, art. arXiv:2007.05561, July 2020.

E. Fehlberg. *Low-order Classical Runge-Kutta Formulas with Stepsize Control and Their Application to Some Heat Transfer Problems*. NASA technical report. National Aeronautics and Space Administration, 1969. URL `https://books.google.de/books?id=IMaJw5g4hGkC`.

Jason W. Ferguson, David R. Alexander, France Allard, Travis Barman, Julia G. Bodnarik, Peter H. Hauschildt, Amanda Heffner-Wong, and Akemi Tamanai. Low-Temperature Opacities. *ApJ*, 623(1):585–596, April 2005. doi: 10.1086/428642.

François Fressin, Guillermo Torres, David Charbonneau, Stephen T. Bryson, Jessie Christiansen, Courtney D. Dressing, Jon M. Jenkins, Lucianne M. Walkowicz, and Natalie M. Batalha. The False Positive Rate of Kepler and the Occurrence of Planets. *ApJ*, 766(2):81, April 2013. doi: 10.1088/0004-637X/766/2/81.

Jeffrey Fung and Eve J. Lee. Inner Super-Earths, Outer Gas Giants: How Pebble Isolation and Migration Feedback Keep Jupiters Cold. *ApJ*, 859 (2):126, June 2018. doi: 10.3847/1538-4357/aabaf7.

Sivan Ginzburg and Eugene Chiang. The end of runaway: how gap opening limits the final masses of gas giants. *MNRAS*, 487(1):681–690, July 2019. doi: 10.1093/mnras/stz1322.

Peter Goldreich and William R. Ward. The Formation of Planetesimals. *ApJ*, 183:1051–1062, August 1973. doi: 10.1086/152291.

A. A. Goodman, P. J. Benson, G. A. Fuller, and P. C. Myers. Dense Cores in Dark Clouds. VIII. Velocity Gradients. *ApJ*, 406:528, April 1993. doi: 10.1086/172465.

G. Guidi, M. Tazzari, L. Testi, I. de Gregorio-Monsalvo, C. J. Chandler, L. Pérez, A. Isella, A. Natta, S. Ortolani, Th. Henning, S. Corder, H. Linz, S. Andrews, D. Wilner, L. Ricci, J. Carpenter, A. Sargent, L. Mundy, S. Storm, N. Calvet, C. Dullemond, J. Greaves, J. Lazio, A. Deller, and W. Kwon. Dust properties across the CO snowline in the HD 163296 disk from ALMA and VLA observations. *A&A*, 588:A112, April 2016. doi: 10.1051/0004-6361/201527516.

Nader Haghighipour and Alan P. Boss. On Gas Drag-Induced Rapid Migration of Solids in a Nonuniform Solar Nebula. *ApJ*, 598(2):1301–1311, December 2003. doi: 10.1086/378950.

Jr. Haisch, Karl E., Elizabeth A. Lada, and Charles J. Lada. Disk Frequencies and Lifetimes in Young Clusters. *ApJ*, 553(2):L153–L156, June 2001. doi: 10.1086/320685.

Eunkyu Han, Sharon X. Wang, Jason T. Wright, Y. Katherina Feng, Ming Zhao, Onsi Fakhouri, Jacob I. Brown, and Colin Hancock. Exoplanet Orbit Database. II. Updates to Exoplanets.org. *PASP*, 126(943):827, September 2014. doi: 10.1086/678447.

Yasunori Hori and Masahiro Ikoma. Critical Core Masses for Gas Giant Formation with Grain-free Envelopes. *ApJ*, 714(2):1343–1346, May 2010. doi: 10.1088/0004-637X/714/2/1343.

Andrew W. Howard, Geoffrey W. Marcy, John Asher Johnson, Debra A. Fischer, Jason T. Wright, Howard Isaacson, Jeff A. Valenti, Jay Anderson, Doug N. C. Lin, and Shigeru Ida. The Occurrence and Mass Distribution of Close-in Super-Earths, Neptunes, and Jupiters. *Science*, 330(6004):653, October 2010. doi: 10.1126/science.1194854.

Jane Huang, Sean M. Andrews, Cornelis P. Dullemond, Andrea Isella, Laura M. Pérez, Viviana V. Guzmán, Karin I. Öberg, Zhaohuan Zhu, Shangjia Zhang, Xue-Ning Bai, Myriam Benisty, Tilman Birnstiel, John M. Carpenter, A. Meredith Hughes, Luca Ricci, Erik Weaver, and David J. Wilner. The Disk Substructures at High Angular Resolution Project (DSHARP). II. Characteristics of Annular Substructures. *ApJ*, 869(2):L42, December 2018. doi: 10.3847/2041-8213/aaf740.

R. Hueso and T. Guillot. Evolution of protoplanetary disks: constraints from DM Tauri and GM Aurigae. *A&A*, 442(2):703–725, November 2005. doi: 10.1051/0004-6361:20041905.

S. Ida and D. N. C. Lin. Toward a Deterministic Model of Planetary Formation. I. A Desert in the Mass and Semimajor Axis Distributions of Extrasolar Planets. *ApJ*, 604(1):388–413, March 2004. doi: 10.1086/381724.

Shigeru Ida, Tristan Guillot, and Alessandro Morbidelli. Accretion and Destruction of Planetesimals in Turbulent Disks. *ApJ*, 686(2):1292–1301, October 2008. doi: 10.1086/591903.

Masahiro Ikoma, Kiyoshi Nakazawa, and Hiroyuki Emori. Formation of Giant Planets: Dependences on Core Accretion Rate and Grain Opacity. *ApJ*, 537(2):1013–1025, July 2000. doi: 10.1086/309050.

Andrea Isella, John M. Carpenter, and Anneila I. Sargent. Structure and Evolution of Pre-main-sequence Circumstellar Disks. *ApJ*, 701(1):260–282, August 2009. doi: 10.1088/0004-637X/701/1/260.

Andrea Isella, Antonella Natta, David Wilner, John M. Carpenter, and Leonardo Testi. Millimeter Imaging of MWC 758: Probing the Disk Structure and Kinematics. *ApJ*, 725(2):1735–1741, December 2010. doi: 10.1088/0004-637X/725/2/1735.

Gerard P. Kuiper. On the origin of the solar system. *Proceedings of the National Academy of Sciences of the United States of America*, 37(1):1–14, 1951. ISSN 00278424. URL http://www.jstor.org/stable/88207.

R. Kuiper, H. Klahr, C. Dullemond, W. Kley, and T. Henning. Fast and accurate frequency-dependent radiation transport for hydrodynamics simulations in massive star formation. *A&A*, 511:A81, 2010. doi: 10.1051/0004-6361/200912355. URL https://doi.org/10.1051/0004-6361/200912355.

Rolf Kuiper, Harold W. Yorke, and Andrea Mignone. Makemake + Sedna: A Continuum Radiation Transport and Photoionization Framework for Astrophysical Newtonian Fluid Dynamics. *ApJS*, 250(1):13, September 2020. doi: 10.3847/1538-4365/ab9a36.

M. Lambrechts, A. Johansen, and A. Morbidelli. Separating gas-giant and ice-giant planets by halting pebble accretion. *A&A*, 572:A35, December 2014. doi: 10.1051/0004-6361/201423814.

Eve J. Lee and Eugene Chiang. To Cool is to Accrete: Analytic Scalings for Nebular Accretion of Planetary Atmospheres. *ApJ*, 811(1):41, September 2015. doi: 10.1088/0004-637X/811/1/41.

Eve J. Lee, Eugene Chiang, and Chris W. Ormel. Make super-earths, not jupiters: Accreting nebular gas onto solid cores at 0.1 au and beyond. *The Astrophysical Journal*, 797(2):95, 2014. URL http://stacks.iop.org/0004-637X/797/i=2/a=95.

C. D. Levermore and G. C. Pomraning. A flux-limited diffusion theory. *ApJ*, 248:321–334, August 1981. doi: 10.1086/159157.

Masahiro N. Machida, Eiichiro Kokubo, Shu-ichiro Inutsuka, and Tomoaki Matsumoto. Angular Momentum Accretion onto a Gas Giant Planet. *ApJ*, 685(2):1220–1236, October 2008. doi: 10.1086/590421.

M. Mayor, M. Marmier, C. Lovis, S. Udry, D. Ségransan, F. Pepe, W. Benz, J. L. Bertaux, F. Bouchy, X. Dumusque, G. Lo Curto, C. Mordasini, D. Queloz, and N. C. Santos. The HARPS search for southern extra-solar planets XXXIV. Occurrence, mass distribution and orbital properties of super-Earths and Neptune-mass planets. *arXiv e-prints*, art. arXiv:1109.2497, September 2011.

Michel Mayor and Didier Queloz. A Jupiter-mass companion to a solar-type star. *Nature*, 378(6555):355–359, November 1995. doi: 10.1038/378355a0.

A. Mignone, G. Bodo, S. Massaglia, T. Matsakos, O. Tesileanu, C. Zanni, and A. Ferrari. PLUTO: A Numerical Code for Computational Astrophysics. *The Astrophysical Journal Supplement Series*, 170:228–242, May 2007. doi: 10.1086/513316.

A. Mignone, C. Zanni, P. Tzeferacos, B. van Straalen, P. Colella, and G. Bodo. The PLUTO Code for Adaptive Mesh Computations in Astrophysical Fluid Dynamics. *ApJS*, 198(1):7, January 2012. doi: 10.1088/0067-0049/198/1/7.

H. Mizuno, K. Nakazawa, and C. Hayashi. Instability of a gaseous envelope surrounding a planetary core and formation of giant planets. *Progress of Theoretical Physics*, 60:699–710, September 1978. doi: 10.1143/PTP.60.699.

T. W. Moldenhauer, R. Kuiper, W. Kley, and C. W. Ormel. Steady state by recycling prevents premature collapse of protoplanetary atmospheres. *A&A*, 646:L11, February 2021. doi: 10.1051/0004-6361/202040220.

T. W. Moldenhauer, R. Kuiper, W. Kley, and C. W. Ormel. Recycling of the first atmospheres of embedded planets: Dependence on core mass and optical depth. *A&A*, accepted, February 2022.

C. Mordasini. Grain opacity and the bulk composition of extrasolar planets. II. An analytical model for grain opacity in protoplanetary atmospheres. *A&A*, 572:A118, December 2014. doi: 10.1051/0004-6361/201423702.

C. Mordasini, Y. Alibert, and W. Benz. Extrasolar planet population synthesis. I. Method, formation tracks, and mass-distance distribution. *A&A*, 501(3):1139–1160, July 2009. doi: 10.1051/0004-6361/200810301.

Simon Müller, Ravit Helled, and Lucio Mayer. On the Diversity in Mass and Orbital Radius of Giant Planets Formed via Disk Instability. *ApJ*, 854(2): 112, February 2018. doi: 10.3847/1538-4357/aaa840.

C. W. Ormel. An Atmospheric Structure Equation for Grain Growth. *ApJ*, 789(1):L18, July 2014. doi: 10.1088/2041-8205/789/1/L18.

C. W. Ormel, R. Kuiper, and J.-M. Shi. Hydrodynamics of embedded planets' first atmospheres - I. A centrifugal growth barrier for 2D flows. *mnras*, 446: 1026–1040, January 2015a. doi: 10.1093/mnras/stu2101.

C. W. Ormel, J.-M. Shi, and R. Kuiper. Hydrodynamics of embedded planets' first atmospheres - II. A rapid recycling of atmospheric gas. *mnras*, 447: 3512–3525, March 2015b. doi: 10.1093/mnras/stu2704.

A. Pannekoek. *A history of astronomy*. 1961.

F. Perri and A. G. W. Cameron. Hydrodynamic Instability of the Solar Nebula in the Presence of a Planetary Core. *Icarus*, 22(4):416–425, August 1974. doi: 10.1016/0019-1035(74)90074-8.

Erik A. Petigura, Andrew W. Howard, and Geoffrey W. Marcy. Prevalence of Earth-size planets orbiting Sun-like stars. *Proceedings of the National Academy of Science*, 110(48):19273–19278, November 2013. doi: 10.1073/pnas.1319909110.

James B. Pollack, Olenka Hubickyj, Peter Bodenheimer, Jack J. Lissauer, Morris Podolak, and Yuval Greenzweig. Formation of the Giant Planets by Concurrent Accretion of Solids and Gas. *Icarus*, 124(1):62–85, November 1996. doi: 10.1006/icar.1996.0190.

Diana Powell, Ruth Murray-Clay, Laura M. Pérez, Hilke E. Schlichting, and Mickey Rosenthal. New Constraints From Dust Lines on the Surface Densities of Protoplanetary Disks. *ApJ*, 878(2):116, June 2019. doi: 10.3847/1538-4357/ab20ce.

Roman R. Rafikov. Atmospheres of Protoplanetary Cores: Critical Mass for Nucleated Instability. *ApJ*, 648(1):666–682, September 2006. doi: 10.1086/505695.

P. L. Roe. Characteristic-based schemes for the euler equations. *Annual Review of Fluid Mechanics*, 18:337–365, January 1986. doi: 10.1146/annurev.fl.18.010186.002005.

V. S. Safronov. *Evolution of the protoplanetary cloud and formation of the earth and planets.* 1972.

J. Schneider. Defining and cataloging exoplanets: The exoplanet.eu database. In *EPSC-DPS Joint Meeting 2011*, volume 2011, page 3, October 2011.

N. I. Shakura and R. A. Sunyaev. Reprint of 1973A&A....24..337S. Black holes in binary systems. Observational appearance. *A&A*, 500:33–51, June 1973.

Donald Shepard. A two-dimensional interpolation function for irregularly-spaced data. In *Proceedings of the 1968 23rd ACM National Conference*, ACM '68, page 517–524, New York, NY, USA, 1968. Association for Computing Machinery. ISBN 9781450374866. doi: 10.1145/800186.810616. URL `https://doi.org/10.1145/800186.810616`.

Kimberley D. Supulver and D. N. C. Lin. Formation of Icy Planetesimals in a Turbulent Solar Nebula. *Icarus*, 146(2):525–540, August 2000. doi: 10.1006/icar.2000.6418.

J. Szulágyi, F. Masset, E. Lega, A. Crida, A. Morbidelli, and T. Guillot. Circumplanetary disc or circumplanetary envelope? *MNRAS*, 460(3):2853–2861, August 2016. doi: 10.1093/mnras/stw1160.

T. Tanigawa, M. Machida, and K. Ohtsuki. Formation of Circumplanetary Disks: High-Resolution Hydrodynamic Simulations. In *European Planetary Science Congress 2012*, pages EPSC2012–610, September 2012.

M. Tazzari, L. Testi, B. Ercolano, A. Natta, A. Isella, C. J. Chandler, L. M. Pérez, S. Andrews, D. J. Wilner, L. Ricci, T. Henning, H. Linz, W. Kwon, S. A. Corder, C. P. Dullemond, J. M. Carpenter, A. I. Sargent, L. Mundy, S. Storm, N. Calvet, J. A. Greaves, J. Lazio, and A. T. Deller. Multi-wavelength analysis for interferometric (sub-)mm observations of proto-planetary disks. Radial constraints on the dust properties and the disk structure. *A&A*, 588:A53, April 2016. doi: 10.1051/0004-6361/201527423.

S. Terebey, F. H. Shu, and P. Cassen. The collapse of the cores of slowly rotating isothermal clouds. *ApJ*, 286:529–551, November 1984. doi: 10.1086/162628.

E.F. Toro. *Riemann Solvers and Numerical Methods for Fluid Dynamics: A Practical Introduction*. Applied mechanics: Researchers and students. Springer, 1999. ISBN 9783540659662. URL `https://books.google.de/books?id=FbemQgAACAAJ`.

S. J. Weidenschilling. Aerodynamics of solid bodies in the solar nebula. *MNRAS*, 180:57–70, July 1977. doi: 10.1093/mnras/180.2.57.

Lauren M. Weiss, Geoffrey W. Marcy, Erik A. Petigura, Benjamin J. Fulton, Andrew W. Howard, Joshua N. Winn, Howard T. Isaacson, Timothy D. Morton, Lea A. Hirsch, Evan J. Sinukoff, Andrew Cumming, Leslie Hebb, and Phillip A. Cargile. The California-Kepler Survey. V. Peas in a Pod: Planets in a Kepler Multi-planet System Are Similar in Size and Regularly Spaced. *AJ*, 155(1):48, January 2018. doi: 10.3847/1538-3881/aa9ff6.

Joshua N. Winn and Daniel C. Fabrycky. The Occurrence and Architecture of Exoplanetary Systems. *ARA&A*, 53:409–447, August 2015. doi: 10.1146/annurev-astro-082214-122246.

A. Wolszczan and D. A. Frail. A planetary system around the millisecond pulsar PSR1257 + 12. *Nature*, 355(6356):145–147, January 1992. doi: 10.1038/355145a0.

J. T. Wright, O. Fakhouri, G. W. Marcy, E. Han, Y. Feng, John Asher Johnson, A. W. Howard, D. A. Fischer, J. A. Valenti, J. Anderson, and N. Piskunov. The Exoplanet Orbit Database. *PASP*, 123(902):412, April 2011. doi: 10.1086/659427.

Yanqin Wu and Yoram Lithwick. Density and Eccentricity of Kepler Planets. *ApJ*, 772(1):74, July 2013. doi: 10.1088/0004-637X/772/1/74.

Harold W. Yorke, Peter Bodenheimer, and Gregory Laughlin. The Formation of Protostellar Disks. I. 1 M sub sun. *ApJ*, 411:274, July 1993. doi: 10.1086/172827.